Uniwersytet Warszawski
Wydział Fizyki
Instytut Fizyki Doświadczalnej
Zakład Cząstek i Oddziaływań Fundamentalnych

Study of charged hadron production with tof-dE/dx identification method in central Ar+Sc collisions in NA61/SHINE experiment at CERN

ROZPRAWA DOKTORSKA

mgr Piotr Podlaski

Promotor:
prof. dr hab. Wojciech Dominik

Promotor pomocniczy:
dr inż. Magdalena Kuich

Warszawa, 2021

Acknowledgements

First and foremost I would like to express my gratitude to my supervisors, Prof. dr hab. Wojciech Dominik and dr inż. Magdalena Kuich for their continuous support, invaluable advice, and patience during my PhD study.

I would also like to thank Prof. Marek Gaździcki, Prof. Peter Seyboth, Maciej Lewicki, Michał Naskręt, Brant Rumberger and other members of the NA61/SHINE Collaboration for joint work and fruitful discussions which greatly contributed to completion of this thesis.

Finally, I would like to express my gratitude to my family and friends. Without their constant support and understanding it would not be possible for me to finish this work.

Abstract

Study of charged hadron production with tof-dE/dx identification method in central Ar+Sc collisions in NA61/SHINE experiment at CERN

This thesis presents results on inclusive spectra of protons, anti-protons, π^+, π^-, K^+ and K^- in 10% of the most central ^{40}Ar+^{45}Sc collisions. Data on Ar+Sc collisions were collected by the NA61/SHINE experiment at the CERN SPS. Results are presented for six beam momenta: 13*A*, 19*A*, 30*A*, 40*A*, 75*A*, and 150*A* GeV/*c*. This is the first measurement of hadron production in Ar+Sc collisions in the SPS energy range.

Identification of charged particles was performed via the $tof-\mathrm{d}E/\mathrm{d}x$ method. The method is based on the simultaneous measurement of particle energy loss in the Time Projection Chambers and time-of-flight through the detector.

Two-dimensional particle spectra are presented as a function of rapidity and transverse momentum. The results include corrections for various effects related to detector and reconstruction procedure efficiencies and particles originating from weak decays. Special attention was paid to the production of K mesons, lightest strange particles produced in heavy ion collisions. Transverse momentum spectra of charged kaons in mid-rapidity were parametrized with a Boltzmann-like exponential function. The parametrization yielded values for the inverse slope parameter T and enabled the calculation of kaon yields in mid-rapidity. Strangeness production in mid-rapidity was studied in the scope of the onset of deconfinement in intermediate-mass nuclei at the CERN SPS energy range.

Hadron production in Ar+Sc interactions is part of the main program of NA61/SHINE related to the study of the onset of deconfinement and the search for the critical point in strongly-interacting matter. The results presented in this thesis were compared with hadron production measurements in *p*+*p*, Be+Be, and Pb+Pb collisions recorded by the NA61/SHINE and NA49 experiments. Moreover, a comparison with predictions of three microscopic theoretical models was provided.

Streszczenie

Badanie produkcji naładowanych hadronów z wykorzystaniem metody identyfikacji tof-dE/dx w centralnych zderzeniach Ar+Sc w eksperymencie NA61/SHINE w CERN

Niniejsza rozprawa przedstawia inkluzywne widma produkcji naładowanych hadronów: porotonów, anty-protonów, π^+, π^-, K^+ oraz K^- w 10% najbardziej centralnych zderzeń ^{40}Ar+^{45}Sc. Dane doświadczalne dotyczące oddziaływań Ar+Sc zebrane zostały przez spektrometr NA61/SHINE działający przy akceleratorze SPS w CERN. Wyniki są przedstawione dla sześciu pędów wiązki: 13A, 19A, 30A, 40A, 75A, 150A GeV/c. Jest to pierwszy pomiar produkcji hadronów w oddziaływaniach Ar+Sc w zakresie energetycznym akceleratora SPS.

Identyfikacja cząstek naładowanych została przeprowadzona z wykorzystaniem metody $tof - \mathrm{d}E/\mathrm{d}x$. Metoda oparta jest na jednoczesnym pomiarze strat energii w komorach projekcji czasowej oraz czasu ich przelotu przez detektor.

Dwuwymiarowe widma produkcji cząstek zostały wynznaczone w funkcji pospieszności i pędu poprzecznego. Obliczono i zastosowano poprawki na efekty związane a wydajnością detektora oraz procedury rekonstrukcji, a także na wkład od cząstek pochodzących ze słabych rozpadów. Widma pędu pop-rzecznego naładowanych kaonów w obszarze średnich pospieszności zostały sparametryzowane z wykorzystaniem Boltzmannowskiego rozkładu wykładnieczego. Parametryzacja widm umożliwiła wyznaczenie krotności naładowanych kaonów w tym przedziale pospieszności, a także pozwoliła na okreslenie wartości odwrotności parametru nachylenia widm T. Wyniki te zostały wykorzystane do badań progu na uwolnienie kwarków w oddziaływaniach jąder o średnich masach przy energiach CERN SPS.

Produkcja hadronów w oddziaływaniach Ar+Sc jest częścią głownego programu doświadczalnego eksperymentu NA61/SHINE polegającego na badaniu progu na uwolnienie kwarków oraz poszukiwaniu punktu krytycznego materii oddziałującej silnie. Wyniki prezentowane w tej rozprawie zostały porównane z pomiarami produkcji hadronów w oddziaływaniach p+p, Be+Be oraz Pb+Pb uzyskanymi przez eksperymenty NA49 oraz NA61/SHINE przy akceleratorze SPS w CERN. Ponadto, wyniki zostały porównane z przewidywaniami trzech mikroskopowych modeli teoretycznych.

Contents

Chapter 1

Introduction

1.1 Standard Model of elementary particles

The Standard Model (SM, [1]) is a theory describing properties of elementary particles and interactions between them. It includes three of the four main forces in Nature: electromagnetic, strong, and weak. Gravity, described by General Relativity, remains a separate theory not included in the SM. The discovery of the last particle predicted by the SM, the Higgs boson, was announced in 2012 by two experiments at the Large Hadron Collider (LHC) at the European Organization for Nuclear Research (CERN): A Toroidal LHC ApparatuS (ATLAS) and the Compact Muon Solenoid (CMS) [2, 3].

The Standard Model organizes elementary sub-atomic particles into groups, including quarks and leptons (constituents of matter) and bosons (force carriers). Properties of particles predicted by the Standard Model are summarized in Fig. 1.1. The quarks appear in six flavors, sub-divided into three generations: up - u, down - d (first generation), charm - c, strange - s (second generation), top - t, and bottom - b (third generation). Similarly, there

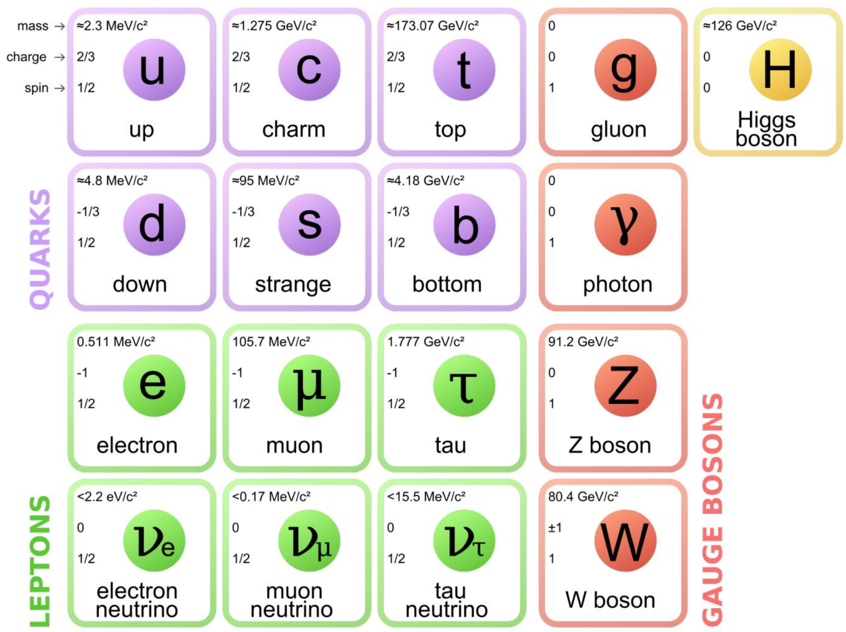

Figure 1.1: Standard Model of elementary particles. Summary of the properties of particles predicted by the model is provided. Picture taken from Ref. [4]

are six leptons in three generations: electron - e, electron neutrino - ν_e (first generation), muon - μ, muon neutrino ν_μ (second generation), tau - τ, and tau neutrino - ν_τ (third generation). The 12 particles listed above are accompanied by their respective antiparticles. Quarks do not exist as free particles and form bound states, called hadrons, constituting two (mesons), three (baryons), four (tetraquarks [5]) or five (pentaquarks [6, 7]) quarks. The lightest quarks, u and d, form protons and neutrons, which together with electrons constitute stable matter in the Universe. Leptons, on the other hand, can exist as free particles.

The gauge bosons mediate elementary interactions between the particles. The SM predicts existence of gluons g carrying the strong force. The weak force is mediated by W^+, W^-, and Z^0 bosons. The electromagnetic force has a single carrier called the photon γ. Quarks interact strongly, weakly, and electromagnetically, while leptons undergo weak and electromagnetic (if the lepton has a non-zero electric charge) interactions. The theory also allows self-interaction of gluons and weak gauge bosons, as well as coupling of photons to $W^\pm$ bosons. Strong and electromagnetic force carriers are massless. The $W^\pm$ and Z^0 bosons have masses of 80.4 GeV/c^2 and 91.2 GeV/c^2, respectively. The electromagnetic force has an infinite range, while the weak and the strong ones are short-ranged (of the order of $\approx 10^{-18}$m and 10^{-15}m, respectively). At sufficiently large energies, above around 250 GeV, the electromagnetic and weak interactions can be described in the common framework of the electro-weak theory [8–10].

The last (in the order of discovery) particle predicted by the SM is the Higgs boson. It is responsible for the masses of the other elementary particles via the so-called Brout-Englert-Higgs mechanism [11, 12]. The mass of the Higgs boson is equal to approximately 125 GeV/c^2.

1.2 Quantum Chromodynamics

Quantum Chromodynamics (QCD) is a part of the Standard Model describing the strong force between quarks and gluons. The *chromodynamics* refers to existence of *color charge*, the analogue of electric charge in Quantum Electrodynamics (QED). Each quark is charged with one of three *colors* (conventionally called *red*, *green* and *blue*), and corresponding anti-quarks can have one of the three *anti-colors* (*anti-red*, *anti-green* and *anti-blue*). The strong interaction involves the exchange of gluons, carrying color and anti-color simultaneously, which leads to an effective change of the quark color state. Gluons exist in an octet of colored states and a colorless singlet. The colorless singlet gluon state was excluded experimentally, as it would cause an un-observed infinite range of strong interactions. From a mathematical perspective, QCD is a quantum field theory with a non-abelian local gauge symmetry based on SU(3) group. The Lagrangian of the theory has a form:

$$\mathcal{L} = -\frac{1}{4} F^a_{\mu\nu} F^{\mu\nu}_a + \sum_{f=1}^{N_f} \overline{\psi}_f (i\not{D} - m_f)\psi_f, \tag{1.1}$$

where $F^a_{\mu\nu}$ is the gluon field strength tensor:

$$F^a_{\mu\nu} = \partial_\mu A^a_\nu - \partial_\nu A^a_\mu - g_s f_{abc} A^b_\mu A^c_\nu, \tag{1.2}$$

$\not{D}$ is the gauge-covariant derivative:

$$\not{D} = \gamma^\mu D_\mu = \gamma^\mu \partial_\mu + i g_s \gamma^\mu A^a_\mu t^a, \tag{1.3}$$

A^a_μ are the gluon fields ($a = 1,...,8$ is the color index), g_s is the strong coupling constant, m_f denote quark masses and γ^μ are Dirac matrices. t^a and f_{abc} denote the SU(3) generators and structure constants, respectively. ψ_f denote the quark fields ($f = u,d,c,s,t,b$ is the flavour index). In fact, the quark fields correspond to the SU(3) triplets of the color states $\psi_f = (\psi^r_f, \psi^g_f, \psi^b_f)^T$, with the upper indices denoting *red*, *green* and *blue* color states.

The QCD coupling constant, in fact, is not a constant, as it changes value depending on the four-momentum transfer Q^2. The running QCD coupling $\alpha_s(Q^2) = g_s/4\pi$ dependence on Q is shown in the left panel of Fig. 1.2. The coupling constant $\alpha_s(Q^2)$ decreases logarithmically with increasing energy scale. Numerical, non-perturbative QCD calculations enable prediction of the interaction potential between two quarks as a function of the distance between them. The $q-q$ potential is presented in the right panel of Fig. 1.2.

The energy-scale dependence of the QCD coupling, together with the shape of the quark-quark potential (Fig. 1.2), lead to two intriguing properties of the theory at the extreme ends of energy scale spectrum: confinement and asymptotic freedom.

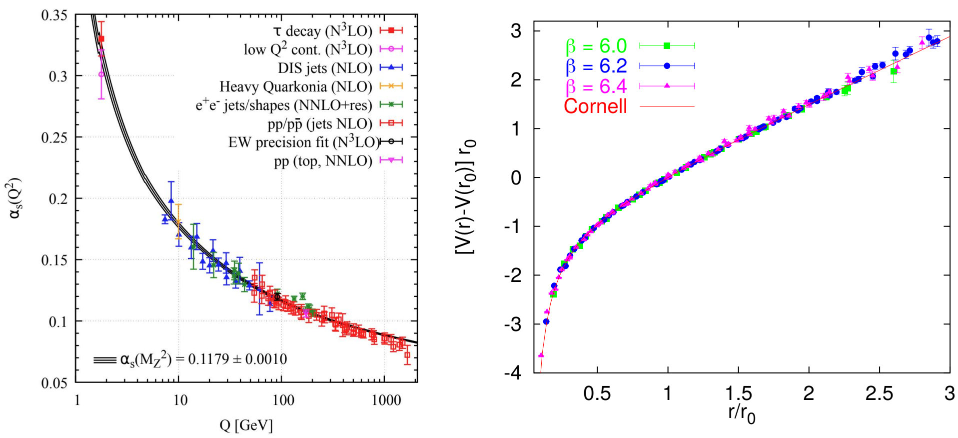

Figure 1.2: *Left*: Summary of measurements of the strong interaction running constant α_s as a function of momentum transfer Q. Figure taken from Ref. [13]. *Right*: The interaction potential between two quarks as a function of distance r. Plot shows results of lattice QCD calculations ($r_0 = 0.5$ fm and $V(r_0) = 0$). Figure taken from Ref. [14].

Confinement

QCD confinement states that carriers of the color charge (quarks and gluons) cannot exist as free particles [15,16]. The interaction potential between two quarks is linear at large distances. If the quarks are separated, the potential energy grows with their distance until it reaches the threshold for quark-antiquark pair production. Then, the production of an additional $q\bar{q}$ pair is more energetically favorable than further increase of the distance between the two original quarks. Schematically, the strong interaction between a pair of quarks due to self-interaction of gluons can be imagined as a string, which under sufficient tension breaks, creating an additional $q\bar{q}$ pair. This process is illustrated in Fig. 1.3.

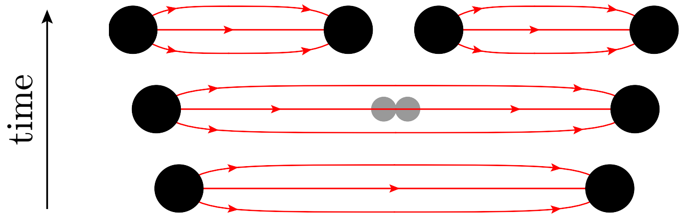

Figure 1.3: An illustration of string breaking by $q\bar{q}$ pair creation. Figure taken from Ref. [13].

Asymptotic freedom

Asymptotic freedom [17, 18] is the QCD property that causes the strong force to be weaker at higher energy scales and shorter distances. In the regime of large Q^2 values, the strong coupling constant becomes small. Thus, in the presence of weaker interactions (in the sense of strength, not to be confused with weak interactions), quarks behave almost like free particles. Small values of the coupling constant at large momentum transfers allow a perturbative approach to the QCD.

1.3 Phases of strongly-interacting matter

1.3.1 Hadron gas

Ordinary matter is composed of quarks and gluons confined in hadrons (protons and neutrons), constituting atomic nuclei and electrons, which together form chemical elements. An ensemble of strongly-interacting particles can be considered a matter in the form of the Hadron Gas (HG). The HG in equilibrium can be composed of many kinds of hadrons, in addition to protons and neutrons, at a wide range of densities and temperatures.

1.3.2 Quark-gluon plasma

One may ask what will happen if the density of matter reaches levels above the mean density of atomic nuclei. In such a case, the distances between nucleons become smaller. Effectively, hadrons will *overlap*. The small distance between quarks signifies the regime of asymptotic freedom. Quarks and gluons are no longer bound to hadrons, but freely propagate in the volume occupied by the system. Quark-Gluon Plasma (QGP, [19–21]), a new state of strongly-interacting matter, is formed. QGP can be formed by compression and/or heating of the hadronic matter, or in general, Hadron Gas. The described QGP formation process is schematically illustrated in Fig. 1.4.

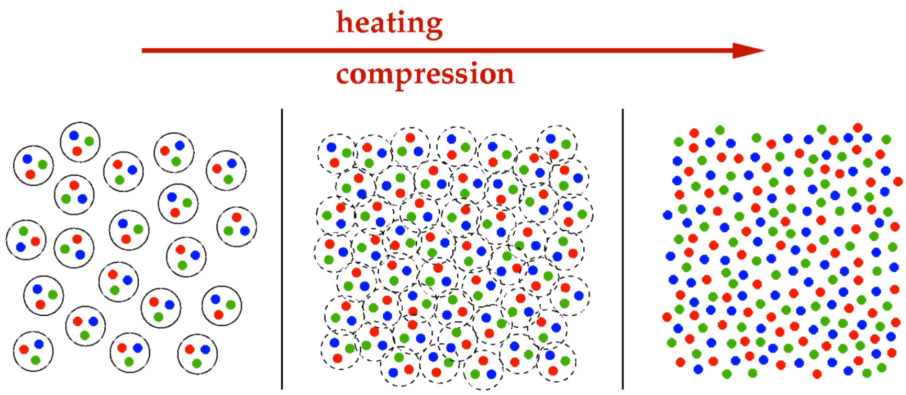

Figure 1.4: A schematic showing creation of the QGP by heating and/or compression of the hadronic matter. Figure taken from Ref. [22].

Today, QGP is expected to occur in Nature in the centers of massive astrophysical objects such as neutron stars. The gravitational interaction is sufficiently strong to create this exotic state of matter. The existence of QGP was confirmed experimentally in ultra-relativistic heavy-ion collisions recorded by the experiments at CERN [23] and Brookhaven National Laboratory (BNL) [24]. In high-energy heavy-ion collisions the QGP formation process takes a violent course, with a characteristic time-scale of the order of 1 fm/c=10^{-23} s.

1.3.3 Phase diagram

QCD calculations enable construction of the phase diagram of strongly-interacting matter as a function of temperature T and baryon chemical potential μ_B. The baryon chemical potential quantifies the energy change of the system caused by the addition or removal of one baryon. A schematic of the diagram is presented in Fig. 1.5. Strongly-interacting matter exists in the HG phase for low temperatures and relatively low baryon chemical potentials. In the opposite case, at high T and/or high μ_B, QGP is formed. Theoretical calculations suggest that the phase transition between HG and QGP is a smooth crossover for low μ_B. The cross-over takes place at the pseudo-critical temperature of $T_C \approx$150 MeV [25]. At higher baryon chemical potential values, a first-order phase transition is expected [26]. The point where the character of the phase transition changes from a smooth crossover to a first order is called the critical point (CP). The existence of the CP has not yet been confirmed. Non-perturbative lattice QCD calculations, based on the realistic quark masses, suggest that the CP is located in the region of $\mu_B - T$ phase diagram available for exploration by experiments operating at the CERN Super Proton Synchrotron (SPS) [27].

1.4 Relativistic collisions

Studies of the phase diagram of strongly-interacting matter require an experimental tool allowing change of system *temperature* and *density*. High-energy collisions of nucleons and atomic nuclei offer such a possibility and have been widely employed in studies of strongly-interacting systems for

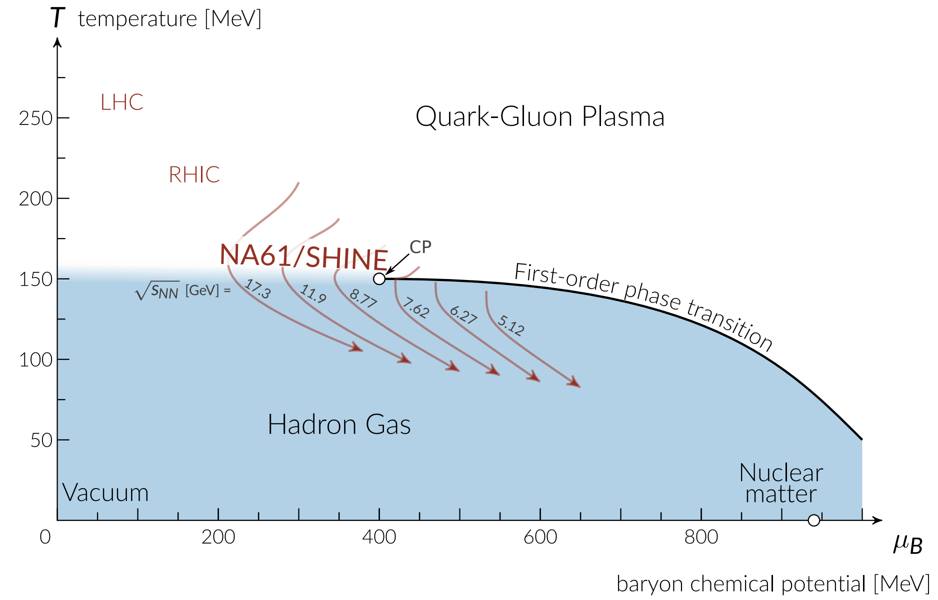

Figure 1.5: A schematic phase diagram of strongly-interacting matter as a function of temperature T and baryon chemical potential μ_B. Red lines show possible evolution of systems created in heavy-ion collisions at the CERN SPS. Figure taken from Ref. [28].

decades. Presently, experimental facilities accelerate hadrons, ions or electrons to nearly the speed of light, resulting in the total energy of particles up to thousands of times higher than their rest masses. The particles are formed into a *beam* - an organized stream of particles with a finite transverse size propagating in a well-defined direction. There are two main types of the high-energy experiments: *collider* experiments, in which particles forming two counter-propagating high-energy beams are forced to collide and *fixed-target* experiments, in which a high-energy beam hits a stationary target. In the high-energy regime, the interactions between the colliding objects are dominated by strong processes. In the fixed-target case, the beam particles are often referred to as the *projectiles*.

1.4.1 Wounded Nucleon Model

A simple geometrical description of the collision act between the two atomic nuclei is provided by the Wounded Nucleon Model (WNM) [29]. A schematic of a nuclear collision is presented in Fig. 1.6. The collision is depicted in the center-of-mass frame of reference. Before the collision, two atomic nuclei approach each other. Trajectories of their geometrical centers are separated by the *impact parameter* b. The nuclei in the center-of-mass frame of reference are (depending on the collision energy) disk-shaped due to Lorentz contraction. Nucleons constituting colliding nuclei can either interact with each other (*participants* of the collision) or pass the collision without any interactions (*spectators*). The interactions can be either elastic or inelastic. The nucleons which underwent inelastic interactions are referred to as *wounded nucleons*. The numbers of spectators N_{spec}, participants N_{part} and wounded nucleons N_{W} can be determined from the geometric parameters such as atomic mass and impact parameter combined with the nucleon-nucleon

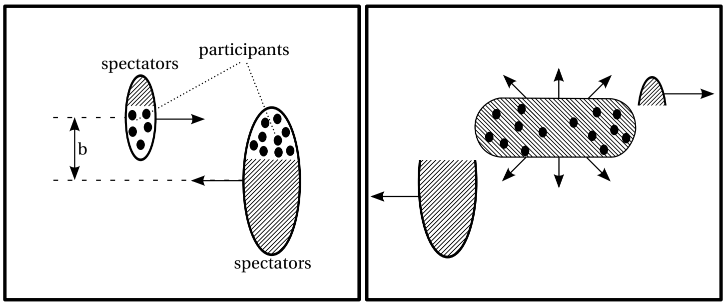

Figure 1.6: A schematic of an inelastic nucleus-nucleus collision. Figure taken from Ref. [30].

interaction cross-sections. Collisions with small values of b are called *central* collisions, while ones with large b are called *peripheral* collisions. In the case of central collisions, numbers of participant and wounded nucleons are approximately equal $N_{\text{part}} \simeq N_{\text{W}}$. The nuclear collision is considered inelastic if at least one pair of nucleons belonging to different nuclei interacted in an inelastic way. A small fraction of inelastic nuclear collisions can be classified as central, while the majority are peripheral [1]. In the case of fixed-target experiments, the number of spectators associated with the projectile particle, often called the number of projectile spectators, is particularly important. It can be estimated with the measurements of the hadron calorimeters and is often used for the estimation of collision centrality.

In the framework of the WNM, the particle production in the nuclear ($A+A$) collisions is a superposition of contributions coming from individual nucleon-nucleon collisions. Within this approach, reference p+p measurements allow determination of the particle multiplicity produced in $A+A$ collisions employing a simple linear scaling, as presented below.

$$n_{A+A} = \frac{1}{2} \cdot \langle W \rangle \cdot n_{p+p}, \tag{1.4}$$

where n_{A+A} and n_{p+p} are the mean multiplicities of particles produced in $A+A$ and p+p collisions, respectively. $\langle W \rangle$ represents the mean number of wounded nucleons in $A+A$ collisions, and the 1/2 factor comes from the fact that in inelastic p+p interactions, two nucleons are wounded. Deviations from the predictions of the WNM are attributed to collective effects present in ion-ion collisions (e.g., QGP formation or collective flow). Although collective effects in heavy-ion collisions were observed experimentally, the WNM still serves as a useful reference for particle production measurements in $A+A$ collisions.

1.4.2 Evolution of the system

A more detailed overview of the ion-ion collision at (ultra-)relativistic energies is schematically presented in Fig. 1.7, according to the currently-adopted model of the process. A non-equilibrium initial state is created just after the collision. Depending on the initial energy density in the colliding system, two scenarios are possible. For low energy densities, a hot

[1] In simplified geometrical picture $\mathrm{d}\sigma/\mathrm{d}b = 2\pi b$ for b smaller than the sum of radii of the colliding nuclei.

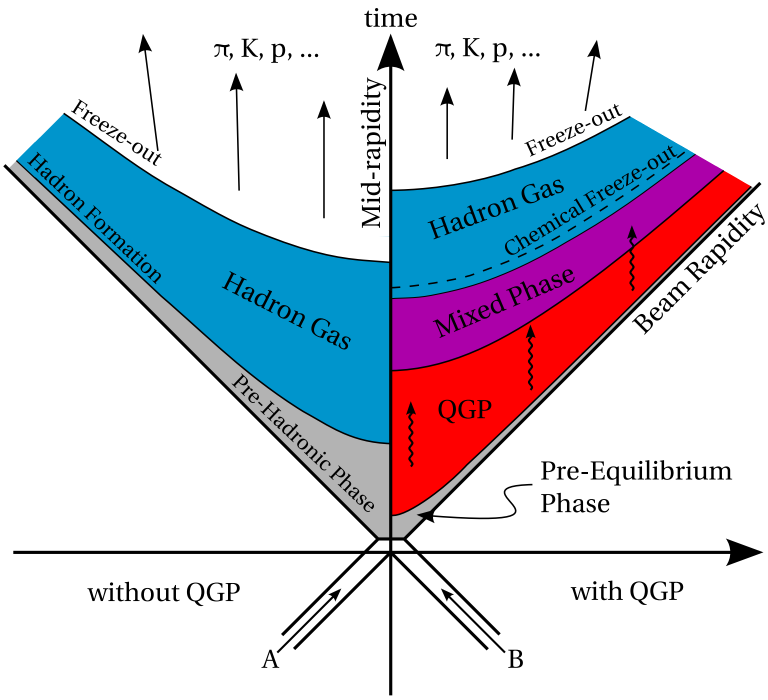

Figure 1.7: A schematic diagram of the evolution of (ultra-)relativistic collision between two atomic nuclei: A and B. Two scenarios are depicted: with (*right*) and without (*left*) formation of the QGP. Picture taken from Ref. [30].

and dense HG is formed (left part of Fig. 1.7). At higher energy densities QGP can be created (right part of Fig. 1.7). Strong interactions between its constituents dominate evolution of the expanding QGP. As the system expands, its temperature drops and hadrons start to emerge. This is known as hadronization, and represents a mixed phase of QGP and HG. The moment when the inelastic interactions between particles stop and hadron composition settles is called *chemical freeze-out*. As HG, present in the final evolution phase of both discussed scenarios, cools its particles undergo elastic interactions mainly through electromagnetic processes. The moment where elastic interactions between produced hadrons stop and their momenta become fixed is called *kinetic freeze-out*. After kinetic freeze-out, particles propagate away from the interaction point and can be detected in the experiments.

1.5 Onset of deconfinement

The instant associated with deconfined states of strongly-interacting matter being created is called the *onset of deconfinement*. Existence of the onset of deconfinement was predicted by the Statistical Model of the Early Stage (SMES) [31] to be located in the lower energy range of the CERN SPS accelerator. SMES predictions motivated an energy scan of hadron production in Pb+Pb interactions by the NA49 experiment at the CERN SPS (forty-ninth experiment at the CERN North Area). The NA49 measurements confirmed the existence of the onset of deconfinement by observing non-monotonous energy dependence of the strangeness to entropy ratio [32].

1.5.1 Statistical Model of the Early Stage

The SMES describes the early stages of a relativistic colliding nuclear system, without attempts to describe its subsequent (hydro-)dynamical evolution and expansion. The SMES is based on the assumption that creation of new particles (degrees of freedom) during the early stages of A+A collisions is a fully statistical process. All microscopic states allowed by the conservation laws can be formed with equal probabilities, and the final macroscopic state maximizes the total entropy. The properties of the state produced at the very beginning of the $A+A$ collision are entirely defined by the volume in which the production takes place and the available energy. It should be noted that only a fraction of the total available energy can be transferred into the creation of new degrees of freedom. The rest is carried by the net baryons escaping the collision region, as baryon number is conserved in strong interactions. The SMES assumes the existence of two pure phases of strongly-interacting matter: confined (HG) and deconfined (QGP). Consequently, the presence of the mixed phase, being a mixture of the mentioned phases, is also possible in the system, depending on which configuration maximizes the total entropy. The deconfined state is assumed to be composed of gluons, u, d, s quarks and their corresponding anti-quarks. The contribution coming from the remaining three quark flavors is neglected due to their large masses. Gluons and all non-strange (anti-)quarks are assumed to be massless, while strange (anti-)quark mass is assumed to be 175 MeV/c^2. The "bag model" equation of state [33] is used to describe the equilibrium deconfined state. In the confined state, non-strange particles, which dominate the entropy production, are assumed to be massless bosons, while strangeness carries are massive with a mass of 500 MeV/c^2, equal to the kaon mass - the most abundant strangeness carrier. The ideal gas equation of state is assumed in this phase. The system created at the very beginning of the collision then expands, hadronizes, and freezes-out, as described in Sec. 1.4.2. The entropy and the total number of s and $\bar{s}$ quarks are postulated to be (approximately) identical in the final stage as in the early stage. The number of internal degrees of freedom is significantly higher in the QGP phase than in the case of HG. Thus quantitative and qualitative differences in particle production properties are expected depending on which phase was present in the early stage of the collision.

1.5.2 Signatures of the phase transition

The SMES predicts a number of signatures of the onset of deconfinement in collisions of large $A+A$ systems (Pb+Pb, Au+Au) that can be observed in high-energy physics experiments. The most important ones are presented in Fig. 1.8 and will be discussed below. SMES predictions in Fig. 1.8 are compared with the corresponding experimental data.

Enhancement of entropy production

The entropy produced in the early stage of a collision is often considered to be proportional to the mean multiplicity of produced pions. In the SMES

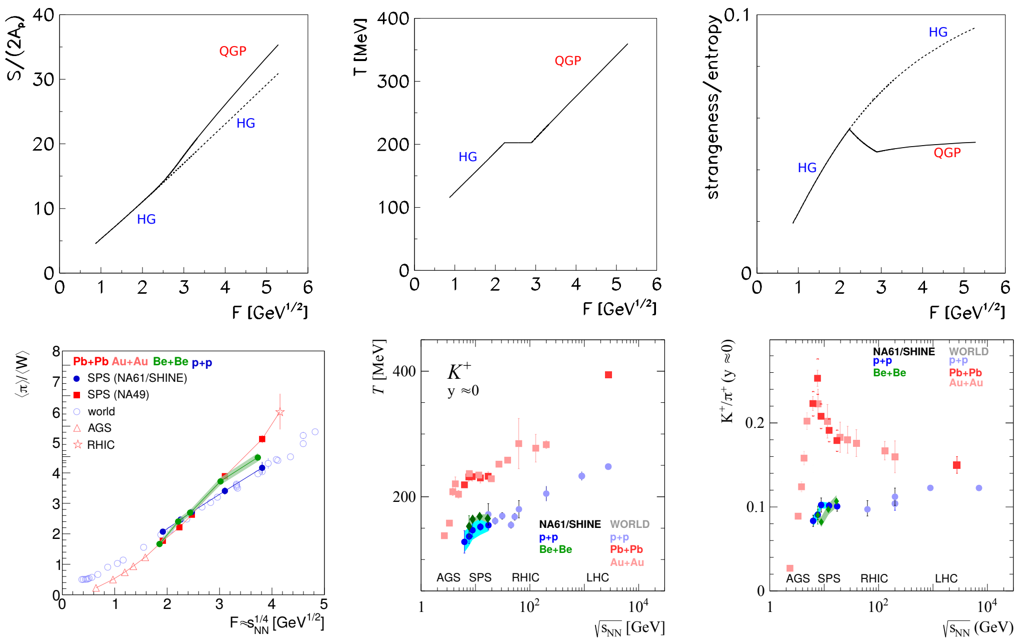

Figure 1.8: *Top row*: Signatures of the phase transition predicted by the SMES, *bottom row*: corresponding experimental results. *Left*: enhancement of entropy production, *middle*: a plateau in temperature, *right*: non-monotonic behaviour of strangeness to entropy production ratio. The signatures are displayed approximately as the collision energy dependence ($F \approx \sqrt[4]{s_{\mathrm{NN}}}$ in the SPS energy range) Figures taken from Refs. [31, 34, 35].

framework, experimentally measurable pion production per number of collision participants (see Sec. 1.4.1) is given by:

$$\frac{\langle \pi \rangle}{N_{\text{part}}} \propto g^{1/4} F, \quad F = \frac{\left(\sqrt{s_{NN}} - 2m_N\right)^{3/4}}{\left(\sqrt{s_{NN}}\right)^{1/4}} \approx \sqrt[4]{s_{NN}}, \tag{1.5}$$

where g is the number of the internal degrees of freedom for a particular phase, F stands for the Fermi-Landau collision energy, and $\sqrt{s_{NN}}$ is the collision energy in the center of mass frame of reference per nucleon pair (see Appendix A). As the number of degrees of freedom in the QGP phase is bigger than for HG, a quantitative difference in entropy production near the phase transition is expected. This change, referred to as *the kink*, was indeed observed in Pb+Pb collisions in the CERN SPS energy range (see left panel of Fig. 1.8).

Temperature of the system

According to SMES, temperature of a system formed in the early stage of a collision increases approximately linearly with the collision energy outside the phase transition region. For collision energies corresponding to the mixed QGP-HG phase formation, the temperature remains constant and equal to the transition temperature. As the temperature cannot be measured directly, the experimentally measured transverse mass (see Appendix A) spectra of charged kaons are described with the following exponential function:

$$\frac{\mathrm{d}n}{m_T \mathrm{d}m_T} = C \cdot \exp\left(-\frac{m_T}{T}\right) \tag{1.6}$$

The inverse slope parameter T corresponds to the kinetic freeze-out temperature T_{fo} of the system, modified for collective transverse flow during the evolution:

$$T \simeq T_{fo} + \frac{1}{2} m_0 \beta_T^2, \tag{1.7}$$

where m_0 and β_T are the mass of the particle and its transverse velocity in the expanding source, respectively. Nevertheless, a similar structure in the energy dependence of the inverse slope parameter for the data on Pb+Pb interactions is visible as in the SMES predictions for the temperature (see middle panel of Fig. 1.8). This structure is referred to as *the step*.

Strangeness production

The most prominent observable of the onset of deconfinement predicted by SMES is the strangeness to entropy production ratio. When crossing the phase transition, masses of the strange particles assumed by the SMES change significantly. Hence, a substantial qualitative difference in the energy dependence of strangeness production in the QGP and HG phases is expected. Indeed, SMES predicts that the strangeness to entropy ratio increases steeply with collision energy for the confined phase. At the onset of deconfinement, the ratio starts to drop and saturates at a constant value at large collision energies with only a pure QGP phase present. The non-monotonic dependence of the strangeness to entropy ratio is called *the horn* and was observed in Pb+Pb and Au+Au collisions (see right panel of Fig. 1.8).

1.6 Predictions for small and intermediate systems

The SMES predictions shown in Fig. 1.8 were calculated for large $A + A$ systems like Pb+Pb or Au+Au. However, the experimental data presented in the same figure also include results on small systems (p+p [36] and Be+Be [34]). The structures visible for large systems (kink, step, horn) are strongly suppressed in the case of p+p and Be+Be. One may ask the question: Is the observed behavior reflected in model predictions? The recently published update of the SMES [31] is able to provide predictions also for smaller systems. The strangeness to entropy ratio as a function of the collision energy for various system sizes, starting at $N_W \approx 2$ (p+p), is presented in Fig. 1.9. According to the SMES, the strangeness to entropy ratio should be strongly enhanced with respect to reference p+p data even for small systems ($N_W \approx 6-10$). Such prediction is in contradiction with the experimental data on Be+Be collisions ($N_W \approx 10$).

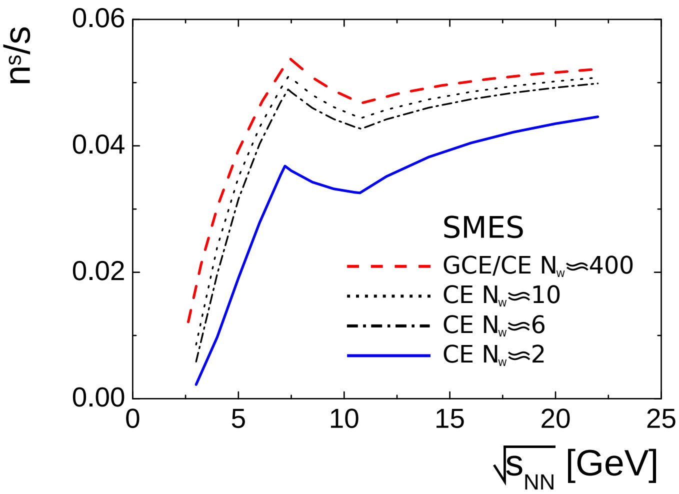

Figure 1.9: SMES predictions of energy dependence of the strangeness to entropy ratio for different colliding system sizes. Figures taken from Ref. [37].

1.7 NA61/SHINE experimental program

Exploration of the phase diagram of strongly-interacting matter in the SPS energy range is one of the main research goals of the NA61/SHINE experiment (sixty-first experiment at the CERN North Area, SPS Heavy Ion and Neutrino Experiment) - the successor of the NA49 experiment, which discovered the onset of deconfinement in Pb+Pb collisions. The experimental program of the NA61/SHINE also includes:

1. precise reference hadron production measurements in p+C reactions for long-baseline neutrino experiments (T2K, NOνA) to constrain neutrino fluxes [38, 39],
2. cross-section and hadron production measurements in π+C interactions to constrain cosmic-ray shower simulations used to determine properties of the primary cosmic-ray particles [40, 41],
3. measurements of nuclear fragmentation cross-section of intermediate-mass nuclei for a better understanding of the cosmic ray propagation in galaxies [42].

The NA61/SHINE experiment performed a unique two-dimensional scan of phase space in system size and collision energy by varying the beam momentum and size of the colliding system. The summary of collected data is presented in the left panel of Fig. 1.10. The data on hadron production were collected for p+p, Be+Be, Ar+Sc, Xe+La, and Pb+Pb reactions at six beam momenta from 13A GeV/c to 150A GeV/c (158 GeV/c for protons)[2]. Choices of particular target and projectile nuclei were based on technical capabilities of the CERN acceleration chain, as well as the chemical and physical properties of the target materials.

Performed measurements translate to coverage of a large volume in the $\mu_B - T$ phase diagram, presented schematically on the right panel of Fig. 1.10. The values of chemical freeze-out temperatures for NA61/SHINE data were estimated based on the hadron gas model simulations [43]. An ample

[2] 13A GeV/c stands for the momentum of 13 GeV/c per nucleon of the beam particle.

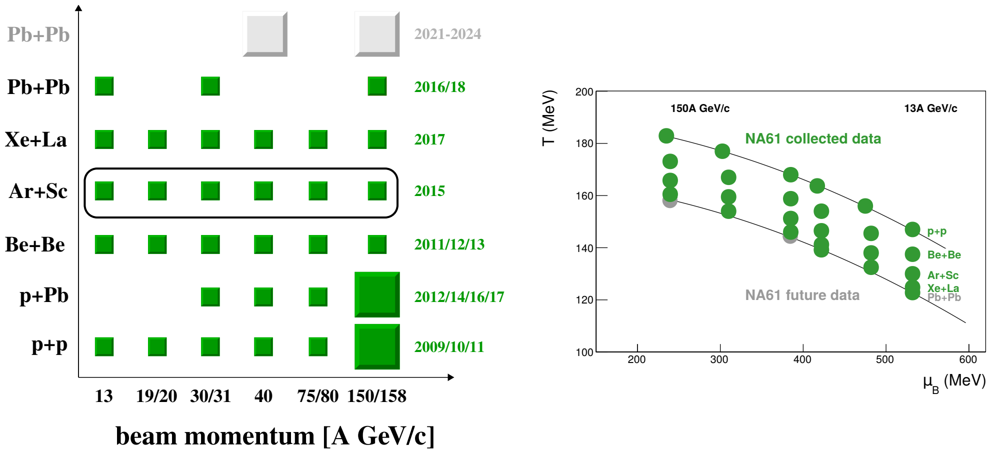

Figure 1.10: *Left*: A summary of data collected by NA61/SHINE experiment during the two-dimensional scan in system size and beam momentum. Green squares denote collected data. Square size reflects accumulated statistics. Gray squares refer to planned measurements after the hardware upgrade. *Right*: Region of the $\mu_B - T$ phase diagram of strongly-interacting matter corresponding to NA61/SHINE measurements. Chemical freeze-out temperatures were estimated based on the hadron gas model [43]. Figures taken from Ref. [44].

collection of experimental data on p+p and $A+A$ collisions accumulated by the NA61/SHINE experiment in the 2007-2018 period allows for precise studies of the transition between the phases of strongly-interacting matter.

Recent results on p+p interactions at SPS (NA61/SHINE) [45] and LHC (CMS, ALICE) [46, 47] show indications of collective phenomena and signs of deconfinement even in collisions of the smallest systems. The study of particle production in the vicinity of the onset of deconfinement is actively explored both experimentally and theoretically, as the existing models fail to describe the results of the experimental measurements.

1.8 Physics content of this dissertation

Studies of Ar+Sc collisions provided in this thesis give an insight on a substantial change of hadron production properties between small (p+p, Be+Be) and large (Pb+Pb, Au+Au) colliding systems. This thesis reports results on the production of the most abundant charged hadrons: protons, anti-protons, π^+, π^-, K^+ and K^- in central Ar+Sc collisions collected by the NA61/SHINE at six beam momenta: 13A, 19A, 30A, 40A, 75A, and 150A GeV/c. Particle production is presented as two-dimensional spectra in rapidity and transverse momentum. Properties of charged K meson production in mid-rapidity are further studied in the scope of the onset of deconfinement.

Structure of the thesis

This thesis consists of seven chapters and three appendices and is organized as follows:

Chapter 1 summarizes the theoretical description of strongly-interacting matter, emphasizing particle production properties in the vicinity of the onset of deconfinement. Chapter 2 contains a detailed description of the facility and experimental setup used for the data collection. The methodology of data reconstruction and Monte Carlo simulations is summarized in Chapter 3. The Ar+Sc dataset is characterized in Chapter 4. A thorough description of the analysis procedure is contained in Chapter 5. Results of the analysis, together with a comparison with world data and theoretical models, are presented in Chapter 6. The thesis is concluded with a summary in Chapter 7.

Supplementary information in appendices include definition of coordinate system and kinematic variables (Appendix A), a brief description of the NA61/SHINE detector upgrade (Appendix B), and numerical results in a tabulated form (Appendix C).

Author's contribution

The NA61/SHINE experiment is a large international project. The experiment's hardware and software were built by a collective effort of many collaborators. I have been a member of the NA61/SHINE since 2015.

I actively participated in the data taking campaigns throughout the years, controlling the experimental conditions and the data acquisition process. Moreover, I was responsible for the operation of the Time Projection Chambers and the Trigger system of the NA61/SHINE detector. Apart from controlling and operating the existing equipment, I was involved in the construction of the new gas system for the Forward Time Projection Chambers and new readout infrastructure for the Forward Time of Flight detector. In 2018 I was appointed deputy coordinator of the NA61/SHINE major hardware upgrade, originally planned for 2019-2021. My work on the upgrade also includes designing and constructing the new Trigger system for the NA61/SHINE experiment.

In parallel to tasks connected with hardware and data taking campaigns, I was involved in data analysis. For the analysis presented in this thesis, I was using calibrated and reconstructed data sets. I studied the event and track selection procedures, tuning the particular cut values to the Ar+Sc data set. I developed and applied the analysis procedure, introducing a low momentum variant of the particle identification method, essential for the data on the two lowest beam momenta. I calculated and applied correction factors based on Monte Carlo simulations. My results are corrected for effects connected with detector efficiency, reconstruction effects, and weakly-decaying particles. I am the author of all calculations and results presented in chapters 5 and 6, if not mentioned differently in the text. The final results were compared with other results of NA61/SHINE, as well as with the results of other experiments and predictions of theoretical models.

Chapter 2

NA61/SHINE detector

This chapter describes the NA61/SHINE facility at CERN. Detailed information about the NA61/SHINE detector setup can be found in Refs. [48, 49].

NA61/SHINE is a fixed-target experiment located in the North Area of CERN, on the H2 beamline of the SPS accelerator. It is a multi-purpose experimental facility allowing measurements of hadron production in hadron-proton, hadron-nucleus, and nucleus-nucleus interactions. The layout of the NA61/SHINE large-acceptance hadron spectrometer is presented in Fig. 2.1.

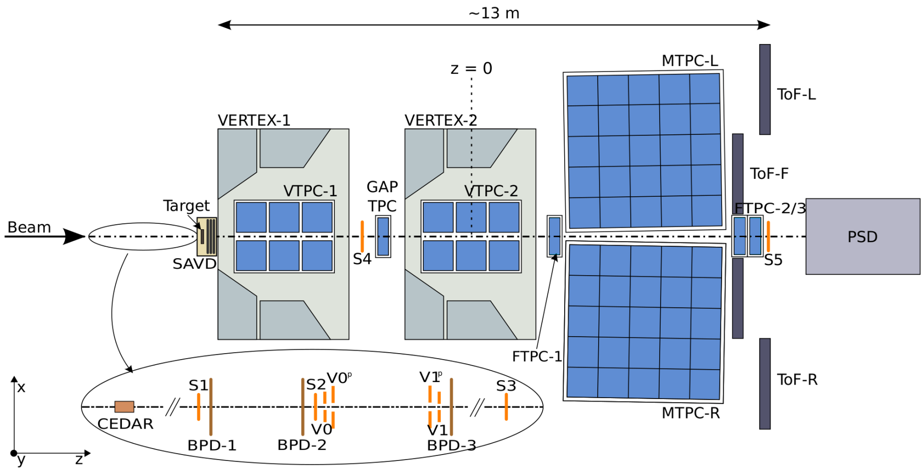

Figure 2.1: Schematic layout of the NA61/SHINE experiment (not to scale). Figure updated from Ref. [48]. A description of the NA61/SHINE coordinate system can be found in Appendix A.

The main components of the detection system are four large-volume Time Projection Chambers (TPCs): VTPC-1, VTPC-2, MTPC-L and MTPC-R. TPCs serve as the primary tracking devices of the NA61/SHINE spectrometer. Two of them, the VTPCs, are placed inside the superconducting magnets VERTEX-1 and VERTEX-2. Additionally, a small-volume TPC, GAP-TPC, is located in the gap between the VTPCs directly in the beamline. The GAP-TPC was added to improve acceptance for particles produced at small angles with respect to the beamline. Three Time of Flight detectors, ToF-L, ToF-R, ToF-F, are placed downstream of the MTPCs. The purpose of the ToF detectors is to improve particle identification capabilities. The NA61/SHINE spectrometer is also equipped with a hadron calorimeter called the Projectile Spectator Detector (PSD). More recent additions to the detector setup are the Small Acceptance Vertex Detector (SAVD) and a set of three small volume TPCs (FTPC-1, FTPC-2, FTPC-3), allowing reconstruction of charm hadrons (SAVD) and improving the forward acceptance (FTPCs). The superconducting magnets, large-volume TPCs, and TOF-L/R detectors were inherited from the NA49 experiment [49] - the predecessor of the NA61/SHINE. This thesis adopts the NA61/SHINE coordinate system described in Appendix A.

2.1 Targets

The targets used by NA61/SHINE for particle production studies are positioned upstream of the VTPC-1 at $z \approx$-580 cm. Typically, the target is mounted in a special target holder device, providing a helium atmosphere around the target and a pneumatic movement system to remove or insert the target in the beam. The helium atmosphere in the vicinity of the target helps to minimize interactions of beam particles with air surrounding the target (so-called off-target interactions). The pneumatic movement system allows easy collection of data with and without the target, thus allowing precise estimation of the contribution of off-target interactions to the final result. After the recent addition of the SAVD to the NA61/SHINE detection system, the target holder was integrated with this detector. It continues to provide a helium atmosphere around the target and a movement system based on piezoelectric motors.

The majority of experiments in the NA61/SHINE use targets made of solid materials. High purity and (preferably) isotopically pure targets are used. NA61/SHINE has collected data using targets made of Be, C, Al, Sc, La and Pb, with thickness between 1 mm and 2 cm, and transverse dimensions of around 2.5×2.5 cm^2. The target samples are checked for possible contamination using a Wavelength Dispersive X-Ray Fluorescence (WDXRF). WDXRF measurement results are used to estimate the biases to cross-section calculations caused by impurities in the target.

The flexibility of the NA61/SHINE detector allows for the use of targets with large longitudinal dimensions, that do not fit the standard NA61/SHINE target holder. The 20 cm long liquid Hydrogen Target (LHT) was utilized for the purpose of p+p measurements. More details on the LHT can be found in Refs. [36, 50]. In the past, NA61/SHINE conducted measurements with a replica of the carbon T2K target, a 90 cm long graphite rod [51, 52], and replica target of the NuMI target, a 120 cm long target composed of graphite fins.

2.2 Beamline and beams

2.2.1 Acceleration chain

NA61/SHINE uses primary and secondary beams delivered by the CERN accelerator complex. The Experiment can utilize various types of beams, from hadrons to heavy ions, in broad momentum range - from 13A GeV/c to 158A GeV/c for ions and 13 GeV/c to 400 GeV/c for hadrons. The upper

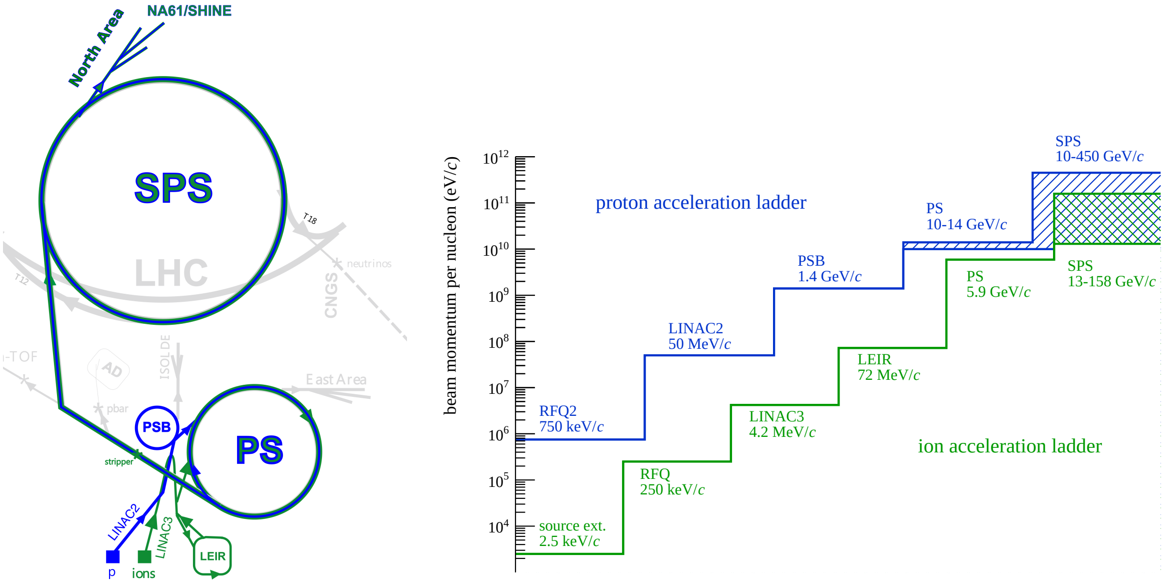

Figure 2.2: *Left:* A schematic of the CERN accelerator chain relevant to NA61/SHINE (top view, not to scale). *Right:* A quantitative visualization of consecutive steps of beam acceleration for protons (blue) and ions (green). Figures taken form Ref. [44].

limit on the beam momentum is imposed by the maximal magnetic field achievable in the H2 beamline magnets, whereas the lower limit is dictated by the beam stability and quality, as the H2 beamline was designed for the maximal SPS energy. The CERN acceleration chain, with components relevant to NA61/SHINE highlighted, is presented in the left panel of Fig. 2.2. From the sources, the beams of protons and ions undergo several acceleration steps to be brought to the target energy in the SPS and finally be extracted to the North Area and NA61/SHINE. The first steps of creation and acceleration of the beam are different for hadrons and ions.

Proton acceleration chain

The proton acceleration chain is presented on the left panel of Fig. 2.2 in blue color. The proton beam is generated from hydrogen gas by a duoplasmatron ion source. The beam is then focused, bunched, and accelerated to 750keV/c in the Radio-Frequency Quadrupole RFQ2. The next step in the acceleration process is LINAC2, a three-tank Alvarez drift tube linear accelerator. The beam is accelerated by the LINAC2 to 50 MeV/c and is then distributed in the four rings of the Proton Synchrotron Booster (PSB), in which the momentum of the beam reaches 1.4 GeV/c. The PSB is followed by the Proton Synchrotron (PS) accelerator, further increasing the beam momentum up to 14 GeV/c for injection into the SPS. In the SPS, the proton beam is accelerated up to 400 GeV/c and is transferred to the North Area using a method called *slow extraction*. The slow extraction mechanism permits the extraction of a constant flux of particles from the SPS over the course of several seconds. This process results in an approximately constant beam intensity delivered to the Experiment during the extraction, referred to as a *spill*. Throughout the acceleration, the beam is delivered in discrete packets called *bunches*. During the extraction process, the bunch structure is removed in a so-called de-bunching procedure, providing a random distribution of the beam particles in time. Consecutive steps of the proton acceleration process and corresponding momentum values are shown on the right panel of Fig. 2.2 with blue color.

Ion acceleration chain

Creation and acceleration of a variety of ion beams (e.g., Ar, Xe, Pb) is also possible in the CERN acceleration complex. The first stages of the ion acceleration chain are different from the proton chain. The acceleration chain for ions is shown on the left panel of Fig. 2.2 and marked with green color. The lead beam starts with the evaporation of isotopically pure ^{208}Pb sample, while gas sources are used for beams originating from nuclei of gases (similarly to protons). The atoms are ionized in an electron cyclotron resonance (ECR) source with electrons accelerated by repetitive microwave pulses. The ions are electrostatically extracted with the energy of $2.5A$ keV/c into the separator, which selects the particular charge state depending on the beam type. After the separator, the momentum of the beam is raised to $250A$ keV/c by the RFQ. Then, the LINAC3 linear accelerator brings the beam momentum up to $4.2A$ MeV/c. The beam is then injected into the Low Energy Ion Ring (LEIR), in which it reaches the momentum of $72A$ MeV/c and is passed to the PS. In the PS, the ion beam is accelerated to $5.9A$ GeV/c and is then extracted to the SPS. At the exit of the PS, on its way to the SPS, the beam traverses a final stripping stage to produce a fully ionized ion beam, i.e. the atoms are stripped of all electrons. The final acceleration of the ion beam is conducted by the SPS, where the beam reaches the momentum of up to $158A$ GeV/c and is *slowly* extracted to the North Area, utilizing the de-bunching procedure, as in the case of the proton beam. It is possible to select the nominal momentum to which the beam is accelerated by the SPS to be lower than the maximal achievable momentum. Consecutive steps of the acceleration of the ion beam, with respective momenta values, are shown on the right panel of Fig. 2.2 in green.

H2 beamline

The extracted SPS beam is transported to the primary target station, where secondary beams can be produced. The H2 beamline, schematically presented in Fig 2.3, emerges from the T2 primary target and can transport primary and secondary momentum-selected particles to the NA61/SHINE experimental area. When operating with primary ion beams, the primary target is removed from the beamline. Beam momentum and charge (positive or negative) are selected by two large spectrometers consisting of dipole magnets and collimators placed along the H2 beamline. Spectrometers allow for the selection of beam rigidity (momentum to charge ratio). A set of magnetic optics in the form of mainly dipole (bending) and quadrupole (focusing) magnets, together with beam detectors and collimators, is also provided through the length of the beamline. Collimators are used to limit

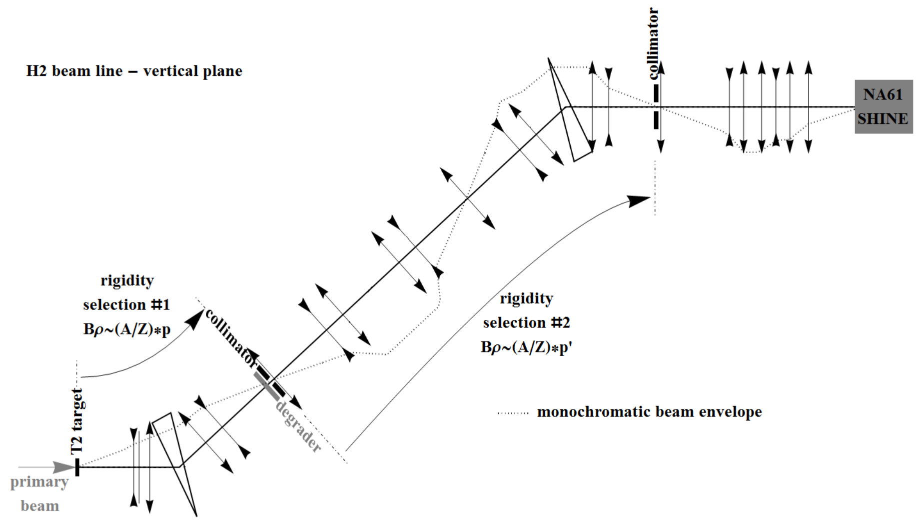

Figure 2.3: A schematic view of the vertical plane of the H2 beamline. The dimensions are not to scale (e.g. the beamline is approximately 600 m long and the height difference between the target station and NA61/SHINE is about 12 m.). Figure taken from Ref. [48]

the transverse size of the beam and to bring its intensity down to the desired level. For the NA61/SHINE experiment, secondary hadron beams of p, K, π, in the momentum range from 13 GeV to 158 GeV produced on the T2 target were used, as well as primary Pb, Ar, Xe attenuated (of a reduced intensity) ion beams in the momentum range from 13A GeV/c to 150A GeV/c. Secondary Be ions produced by the Pb beam fragmentation on the primary T2 Be target were also provided to NA61/SHINE by the H2 beamline in the same momentum range.

2.2.2 Beam detectors

A set of scintillating detectors (S1, S2, V0, $V0^p$, V1, $V1^p$) together with three precise gaseous Beam Position Detectors (BPDs) are located on the beamline upstream of the NA61/SHINE target[1]. These detectors provide precise timing reference and information on the charge and position of the incoming beam particles. Three scintillating counters (S3, S4, S5) are also placed downstream of the target. They serve as interaction detectors and allow for triggering on inelastic interactions of the beam particles inside the target. A schematic diagram of the beam counters is visible on the enlarged view in the left bottom corner of Fig. 2.1. Typical parameters of the counters are summarized in table 2.1.

Readout of the plastic scintillating detectors is performed by fast photomultiplier tubes (PMTs), which collect the light originating from scintillation and transform it into electrical signals which are passed to the readout and trigger electronics. A set of counters to be used in a given data taking campaign is carefully selected based on the beam type and trigger requirements. To minimize the number of interactions of the beam particles with

[1] Hereafter, the *target* will always refer to the NA61/SHINE target, unless explicitly stated differently.

detector	dimensions [mm]	hole [mm]	position [m]
S1	$60 \times 60 \times 5$		-36.42
S2	$\phi = 28 \times 2$		-14.42
S3	$\phi = 26 \times 5$		-6.58
S4	$\phi = 20 \times 5$		-2.11
S5	$\phi = 20 \times 5$		9.80
V0	$\phi = 80 \times 10$	$\phi = 10$	-14.61
$V0^p$	$300 \times 300 \times 10$	$\phi = 20$	$\approx$ -14
V1	$100 \times 100 \times 10$	$\phi = 8$	-6.72
$V1^p$	$300 \times 300 \times 10$	$\phi = 20$	-6.74
BPD-1	$48 \times 48 \times 32.6$		-36.20
BPD-2	$48 \times 48 \times 32.6$		-14.90
BPD-3	$48 \times 48 \times 32.6$		-6.70
Typical thin target position			-5.81

Table 2.1: Summary of typical beam detector parameters: dimensions, positions along the beamline (z coordinates) [48]. Positions of most of these detectors varied in time by a few cm due to dismounting and remounting in subsequent runs. Positions of the detectors are surveyed before each run.

the detector material, it is vital to minimize the amount of material on the beamline, especially for ion beams. In the following part of this section, the roles of the given counters in the trigger system will be discussed. A detailed description of the NA61/SHINE trigger system is provided in section 2.3.

The first detector on the beamline, S1, is a scintillating detector. S1 is equipped with four PMTs, one on each side perpendicular to the beamline, called S1_1-S1_4. Given the large transverse size of the counter, light collection from all four sides of the scintillator allows precise timing measurements, independent of the beam particle position in the scintillator plane. The signal from the first PMT of the S1 counter is used in the trigger and is commonly called S1, omitting the PMT number for convenience. S1 provides a precise timing reference for the entire Experiment. It is vital for the ToF detectors described in section 2.5, as the S1 is used as a *start* signal for the ToF readout electronics.

S2 is the second detector in the beamline. Similar to the S1, it is a scintillating counter. S2 is always used in coincidence with S1 in the trigger logic. The amount of light produced by the scintillator, and hence the amplitude of the PMT signal, is proportional to the squared charge Z^2 of the incoming particle. Therefore, the amplitudes of the S1 and S2 signals can be used to select beam particles with different charge states Z in off-line analysis or even at the trigger level.

The next group of detectors is comprised of veto counters: V0, $V0^p$, V1 and $V1^p$. These counters are plastic scintillators with small holes in the middle (see table 2.1). As the name implies, they are used in anti-coincidence (veto) mode in the trigger logic. The purpose of the veto detectors is to allow the triggering only on the central part of the beam, removing the beam halo.

S3, S4, and S5 are the interaction counters, the final group of plastic scintillator detectors used in the NA61/SHINE beamline. They are placed downstream to the target and are used to detect interactions of the beam particles. Interaction anywhere between the last counter running in coincidence (typically S2) and the given interaction counter is signaled by the absence of the beam particle signal in this counter. Hence, to detect interactions, these counters are used in anti-coincidence mode in the trigger logic. A single interaction counter is typically selected for triggering, depending on the beam type and the detector configuration.

During operation with secondary hadron beams, the beamline is equipped with a Cherenkov Differential Counters with Achromatic Ring Focus (CEDAR) [53] detector. The CEDAR belongs to the beam instrumentation and is not a part of the NA61/SHINE experimental setup. The detector uses gas as a radiator and is equipped with a dedicated optical system. Adjusting the pressure of the gas filling the detector and tuning the optics allows the CEDAR to accept only a desired hadron species. The CEDAR signal is used in coincidence mode in the trigger logic and enables selection of a desired hadron species at the trigger level. During periods where the CEDAR is not needed, it is removed from the beamline and replaced by a vacuum beam pipe to minimize the amount of the material in the beamline.

Each beam particle trajectory is measured by a telescope of three BPDs placed along the beamline upstream of the target. A schematic view of a single BPD detector is shown in Fig. 2.4. BPDs are gas detectors operated with 85/15 Ar/CO_2 mixture. Each BPD contains two planes of orthogonal readout strips, allowing position measurement in $x-y$ plane. The measurement done by the BPDs allows extrapolation of the beam particle trajectories to the target z-plane with the precision of the order of 100 µm.

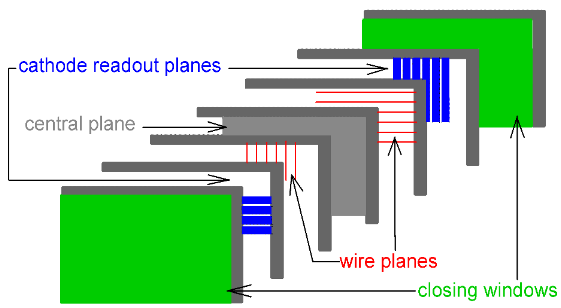

Figure 2.4: Schematic layout of a BPD detector.

2.3 Trigger system

The trigger system is an essential part of most modern high-energy physics experiments. The system aims to select a class of events that are of particular interest. The selection is made in real time and greatly reduces the data throughput that must be handled by the detector readout, reducing the overall complexity and cost of the experiment.

The NA61/SHINE spectrometer is equipped with a versatile and robust trigger system. The system employs analog signals from beam detectors listed in table 2.1 (BPDs are not included in the trigger), together with the CEDAR detector. It produces trigger decisions through simple coincidences of these signals. In principle, any analog or digital signal which arrives with a delay up to ≈300 ns relative to the S1 signal can be included in the trigger. Therefore, an analog signal produced by the PSD (see Sec. 2.6) is often included in the trigger, providing an online selection of event centrality in a collected data sample. A schematic diagram of the trigger logic used in the NA61/SHINE is shown in Fig. 2.5. The analog signals from up to 16 beam counters and other detection channels are discriminated using Constant Fraction Discriminators (CFDs) (see the following paragraph) and passed to the core of the trigger logic - unit based on Field Programmable Gate Array (FPGA). The logic programmed into the FPGA produces the Main Trigger (MT) signal and provides a set of signal outputs for monitoring purposes. The MT signal is used to start the data acquisition by detector readout electronics.

The CFD transforms analog signals into digital form if the amplitude of the input signal is of sufficiently high value. The discrimination threshold can be set independently for all input channels.

Up to four independent trigger configurations can be run simultaneously, called T1-T4. A simple set of positive and negative coincidences and anti-coincidences is employed to generate the trigger signals. An example configuration of T1-T4 trigger definitions used during data taking with secondary hadron beams is presented in table 2.2

After the T1-T4 signals are generated, they are sent to the prescaler module. The role of the prescaler is to select only a fraction of triggers of a given type that will contribute to MT generation, resulting in a smaller contribution of those triggers in the data sample saved on disk. A prescaler can be configured to pass only one of N input pulses, where $N \in [1, 4096]$ is a configurable parameter. As a result, only a fraction equal to 1/N of the total number of triggers of a given type will contribute to MT generation. The prescaling mechanism is used to achieve the desired contribution of events triggered by each of the four trigger configurations in the collected

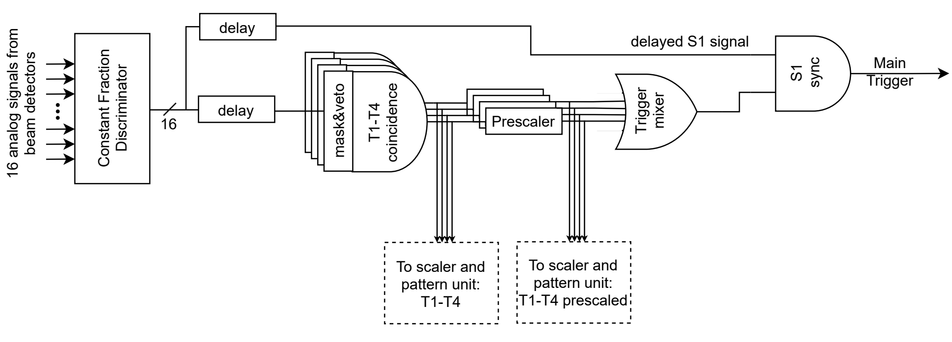

Figure 2.5: Schematic diagram of the trigger logic with the discriminator at the input.

data sample. The MT signal is generated by combining the prescaled triggers with an OR gate and is later synchronized with the delayed S1 signal via the "S1 sync" coincidence. The trigger logic, including coincidences and prescaling, runs synchronously with the FPGA clock, while the resulting MT signal is expected to be synchronous with the beam signals (S1); hence the synchronizing coincidence is employed. The main coincidence unit produces a set of signals for monitoring purposes, including raw and prescaled T1-T4 trigger signals. Those signals are connected to scalers counting the number of pulses during each spill and units registering patterns of signals present during the event readout, allowing event tagging with the trigger type to be later used in the analysis.

The simultaneous use of beam ($T_{BEAM} = T1$) and interaction ($T_{INT} = T2$) triggers allows for an approximate measurement of the interaction probability, P_{INT}:

$$P_{INT} = \frac{N(T_{INT})}{N(T_{BEAM})} \tag{2.1}$$

where $N(\cdot)$ refers to the number of triggers of a given type. Moreover, when running with secondary hadron beams, it is possible, with the use of CEDAR signal, to define such pairs of triggers for both identified and unidentified beam particles, providing two interaction probabilities (see table 2.2). The probability measurement defined above is available on the SPS spill-by-spill basis and is often used during the beam tuning and as diagnostic information during the data taking.

The time structure of the beam detected by the S1 counter is recorded by a CAEN V1290N multi-hit time-to-digital converter (MHTDC). The MHTDC registers precise timing (25 ps resolution) of all signals present in the ±25 µs time window around the triggering particle. MHTDC measurements are used to exclude events with other beam particles close in time with respect to the triggering particle.

2.4 Time Projection Chambers

The main components of the NA61/SHINE tracking system are four large-volume TPCs. TPCs are sensitive to charged particles, which are detected as three-dimensional position measurements of energy deposits in the detector active volumes.

The *Vertex* TPCs, VTPC-1 and VTPC-2 are located between the coils of two

Name	Definition	Description
T1	$S1 \cdot S2 \cdot \overline{V0} \cdot \overline{V1} \cdot CEDAR$	identified beam
T2	$S1 \cdot S2 \cdot \overline{V0} \cdot \overline{V1} \cdot CEDAR \cdot \overline{S4}$	identified interaction
T3	$S1 \cdot S2 \cdot \overline{V0} \cdot \overline{V1}$	unidentified beam
T4	$S1 \cdot S2 \cdot \overline{V0} \cdot \overline{V1} \cdot \overline{S4}$	unidentified interaction

Table 2.2: An example list of trigger definitions used during data taking with secondary hadron beams.

large superconducting dipole magnets VERTEX-1 and VERTEX-2, respectively. The magnetic field in both VERTEX magnets is oriented anti-parallel to the y axis (pointing *down*), and provides total bending power of up to 9 Tm. This magnetic field orientation results in trajectories of positively charged particles produced in an interaction being bent towards the $+x$ direction, while negatively charged ones towards the $-x$ direction. Precise measurement of deflection of charged particle track by the magnetic field allows for determination of the momentum of a particle and its charge sign. The magnitude of the fields in the VERTEX magnets is changed for each beam momentum to provide optimal acceptance in the collision center-of-mass frame of reference. To account for the magnetic field inhomogeneities at the edges of VTPC active volumes, an accurate magnetic field map is used by NA61/SHINE tracking and reconstruction software.

The remaining two large-volume *Main* TPCs, MTPC-L and MTPC-R are placed downstream to the magnets, symmetrically around the beam. The MTPCs improve the accuracy of the energy loss measurement and provide precise tracking of charged particles toward the ToF detectors. Additionally, between VTPC-1 and VTPC-2, a smaller TPC (the GAP-TPC) is located directly in the beamline. Its purpose is to measure particles with the smallest production angles outside of the acceptance of the large chambers. In 2017 the NA61/SHINE experimental setup was extended with three additional Forward TPCs: FTPC-1, FTPC-2 and FTPC-3 [54]. The FTPCs, similar to the GAP-TPC, are placed directly in the beamline between VTPC-2 and MTPCs (FTPC-1) and downstream to the MTPCs (FTPC-2/3). The FTPCs greatly improve track reconstruction capabilities in the region of tracks produced at small polar angles. The small TPCs (GAP-TPC and FTPCs) were not used in the Ar+Sc data taking campaign. During mentioned data taking, FTPCs were not yet installed, and the GAP-TPC was removed from the beamline due to high track multiplicity, as the high track density in the beam region renders the GAP-TPC unusable. The heaviest system in which the GAP-TPC was used was Be+Be.

2.4.1 Principle of operation

A simplified schematic of a TPC is shown in Fig. 2.6. The electric field is formed by a structure composed of conductive field-shaping electrodes, a cathode plate, and a readout plane, all surrounding the active region of a TPC marked in gray. Field-shaping electrodes coupled with a resistive voltage divider are used to generate a uniform electric field, called the drift field, in the active volume of a TPC. Charged particles traversing the active volume ionize detector gas molecules along their trajectory. Electrons created in this process form primary ionization clusters, shown as blue circles on Fig. 2.6. The primary ionization electrons drift under the influence of the drift field toward the readout structure with the drift velocity v_D.

The most common choice for a medium filling active volume of a TPC used in high energy physics experiments is a gas mixture composed of the better part of noble gas (e.g., Ar, Ne) with the addition of a small amount of so-called quenching gas (e.g., CO_2, CH_4). The noble component is susceptible to ionization by charged relativistic particles, while the quencher portion stabilizes the operation of the mixture and suppresses uncontrolled growth

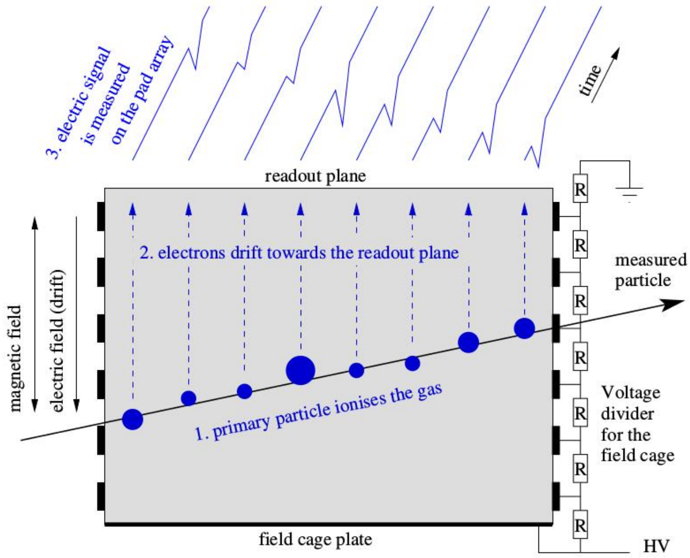

Figure 2.6: A simplified schematic presenting the principle of operation of a Time Projection Chamber. Figure taken from Ref. [55].

of electron avalanches. Stability of the gas mixture throughout the data taking periods is crucial, as variations in the mixture composition or possible contamination may change the drift velocity of electrons (v_D) or gas amplification gain, leading to the deterioration of the collected data quality.

Apart from the stated dependence of the drift velocity on mixture composition and purity, it also depends on the temperature and pressure of the gas. In NA61/SHINE, all critical parameters (v_D, temperature, pressure, mixture composition) are monitored during data taking and are later used to estimate the true drift velocity used in the reconstruction procedures. The measured drift velocity differs from the one inside the TPC due to differences in environmental conditions (temperature, pressure) between the drift velocity monitor and the chamber itself.

Typically, if the TPC is placed in a magnetic field, the direction of the field is parallel to the drift field. Such orientation minimizes the contribution of so-called $\overrightarrow{E} \times \overrightarrow{B}$ effect. The effect is caused by the Lorentz force acting on the primary ionization electrons. In the absence of the $\overrightarrow{E} \times \overrightarrow{B}$ component (parallel $\overrightarrow{E}$ and $\overrightarrow{B}$ fields), the drifting charge follows the $\overrightarrow{E}$ field lines, which greatly simplifies the reconstruction procedure.

The number of primary electrons induced in ionization clusters is too small to be directly detected by electronic readout (typically order of a few hundred per centimeter of particle path). Hence an amplification structure is necessary. The NA61/SHINE TPCs employ amplification in readout chambers based on Multiwire Proportional Chambers (MWPC) [56,57]. Presently there exist TPC designs where MWPCs are replaced with amplification based on Gas Electron Multiplier foils [58, 59]. A schematic layout of the MWPC-based TPC readout chamber is presented in Fig. 2.7. A gating grid separates the drift volume from the MWPC, which itself is made of two cathode planes surrounding a sense wire plane. The cathode plane closer to the gating grid is made of wires, while the other one is a solid plane

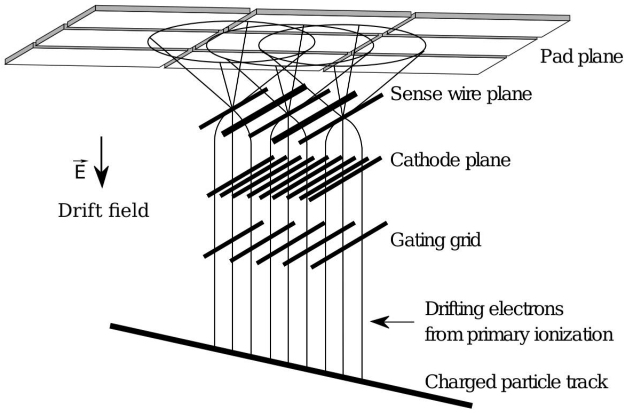

Figure 2.7: A schematic layout of the TPC readout chamber illustrating its principle of operation. Figure taken from Ref. [49].

subdivided into pads and serves as a signal readout. The ionization cluster position in the readout plane can be measured due to the segmentation of the plane into independently read-out pads. The distance of the cluster from the readout plane can be determined by measuring the drift time combined with knowledge of the electron drift velocity v_D.

The sense wire plane is made of anode wires interspaced with field (zero potential) wires. The presence of the field wires helps with shaping the electric field and allows usage of lower anode voltages (of the order of +1kV), resulting in a more stable operation of the chamber (see Ref. [60]). Primary ionization electrons are accelerated by the high electric fields generated by the anode wires. When electrons reach the vicinity of the anode wires, they experience inelastic (secondary) ionizing collisions with gas atoms, giving rise to a multiplicative avalanche. Electrons liberated in the secondary ionization processes are collected by the anode wires, while positive ions drift towards cathodes and later the gating grid. Local currents produced mainly by the movement of the positive ions [57] induce a charge on the readout pads, which is then picked up by charge-sensitive amplifiers of the Front End Electronics (FEE) [61]. High voltage on the anode wires is tuned so that MWPC operates in proportional mode. This means that the magnitude of the signal induced on the readout plane is proportional to the primary ionization charge of the cluster, which is proportional to the value of the energy deposit. The distance between the sense wire plane and the readout pad plane is small (down to 2 mm) in order to narrow the induced charge distribution width, improving two-track separation and overall measurement resolution.

The cathode wire plane aims to separate the amplification region (MWPC) and the drift volume electrically. Positive ions produced in the gas amplification process can drift back to the drift volume, accumulating a considerable amount of space charge inside the active volume, causing severe distortions in electric field distribution. The cathode wires, as a side effect, collect a large number of those ions.

An additional gating grid wire plane is used to provide better isolation of the amplification and drift volumes. The gating grid has two states: *open* and *closed*. In the *open* state, all the wires are held at the potential U_G, which makes the grid transparent to electrons drifting towards the amplification region, and ions going in the opposite direction. In the *closed* state, additional alternating $U_G \pm \Delta U$ potential is applied to every second wire (for the NA61/SHINE TPCs ΔU is of the order of 50V). It prevents ions and electrons from passing between the drift and amplification volumes. It assures that primary ionization charge is passed to the amplification structure only during charge collection (FEE sampling). Such a mechanism greatly reduces aging of anode wires and prevents space charge accumulation inside the chamber. After a valid readout trigger signal is received, the gating grid opens and the TPC FEE samples signals from all pads into 256 so-called time-slices with 5 MHz sampling frequency, leading to the charge collection window of $t_{sampling} = 51.2$ µs. This particular value of the charge collection time arises from the length of the drift volume in y coordinate - d and the electron drift velocity v_D inside the chamber, providing $t_{sampling} \simeq d/v_D$. After the sampling is done, the gate closes, and the cycle repeats with the next accepted trigger.

2.4.2 NA61/SHINE TPCs

The NA61/SHINE TPCs are cuboidal gas vessels with dimensions and other important parameters summarised in table 2.3. The dimensions are given according to TPC placement, along x (width), y (height) and z (length) axes in the NA61/SHINE coordinate system (described in Appendix A). MTPCs and VTPCs are divided into sectors, read out by independent MWPCs, while the GAP-TPC and FTPCs each consist of one single sector. The sector structure can be seen in Fig. 2.1. The topology of the NA61/SHINE TPC readout electrodes is optimized for the measurement of particles with $p_x \cdot q > 0$ (particles bent by magnetic field away from the beam axis). The readout pads in VTPCs and MTPC sectors closest to the beamline are tilted such that the angle between said tracks and readout pads is minimized (see Ref. [49]). Moreover, the TPC readout topology in NA61/SHINE allows the detection of up to 234 ionization clusters along the track, corresponding to energy loss measurements in many thin gas layers. The NA61/SHINE TPCs operate with Ar/CO_2 gas mixture. Proportions of the mixture, employed

	VTPC-1/2	MTPC-L/R	GAP-TPC	FTPC-1/2/3
Size (L×W×H) [cm]	250 × 200 × 98	390 × 390 × 180	30 × 81.5 × 70	60×71(81)×160
Drift length [cm]	66.60	111.74	58.97	101.40
Drift field [V/cm]	195	170	173	171
Gas mixture Ar/CO_2	90/10	95/5	90/10	94/6
Drift velocity [cm/µs]	1.4	2.3	1.3	2.1
Number of sectors	2 × 3	5 × 5	1	1
No. of pads/TPC	26 886(27 648)	63 360	672	1536

Table 2.3: The parameters of the NA61/SHINE Time Projection Chambers. Dimensions are given along x (width), y (height) and z (length) axes in the NA61/SHINE coordinate system (described in Appendix A). Number of pads in VTPC-2 is slightly higher than in VTPC-1. Also, FTPC-1 is 10 cm narrower than FTPC-2/3.

drift field values and resulting electron drift velocities are summarised in table 2.3.

2.4.3 Particle identification

Figure 2.8 shows the dependence of mass stopping power for muons traversing a copper medium as a function of $\beta\gamma$. For moderately relativistic particles ($0.1 \leq \beta\gamma \leq 500$), the mean rate of energy loss in medium is given by the Bethe-Bloch formula [13]:

$$\left\langle -\frac{\mathrm{d}E}{\mathrm{d}x} \right\rangle = Kz^2 \frac{Z}{A} \frac{1}{\beta^2} \left[\frac{1}{2} \ln \frac{2m_e c^2 \beta^2 \gamma^2 W_{\mathrm{max}}}{I^2} - \beta^2 - \frac{\delta(\beta\gamma)}{2} \right] \tag{2.2}$$

where $K = 0.307$ MeV mol^{-1} cm^2 is a constant, z is the charge of the incident particle, Z and A are atomic and atomic mass number of the absorber, $\beta = v/c$ is the velocity of the particle, m_e is the electron mass, I denotes mean excitation energy of the absorber, W_{max} is the maximal possible energy transfer in a single collision, and $\delta(\beta\gamma)$ refers to density effect correction to ionisation energy loss. The fragment of the curve in Fig. 2.8 highlighted with red line corresponds to the region described by formula 2.2. Energy loss per unit length depends on the velocity of the particle, thus independent measurements of mean energy loss and particle momentum allow for particle mass determination.

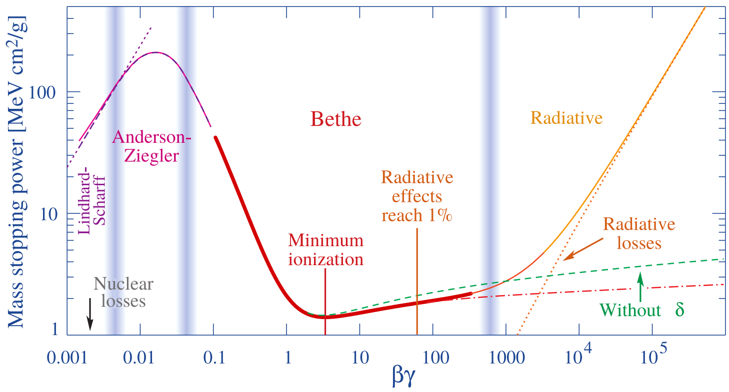

Figure 2.8: Energy loss per unit length $\left\langle -\frac{\mathrm{d}E}{\mathrm{d}x} \right\rangle$ as a function of $\beta\gamma$. Thick red line marks the region relevant for TPC operation in a typical high energy physics experiment. Figure taken from Ref. [13].

For a single ionizing particle traversing a TPC energy deposits of measured clusters follow a Landau distribution, presented on the left panel of Fig 2.9. The distribution is characterized by a long tail towards large energy deposition values. Hence large fluctuations in the measurements are expected. The impact of the fluctuations on energy loss measurement is reduced by employing the so-called truncation procedure, demonstrated in the right panel of Fig. 2.9. This procedure discards 50% of clusters with the highest charges, effectively suppressing the long tail of the Landau distribution. The truncation procedure improves energy loss measurement resolution by up to 20% [49].

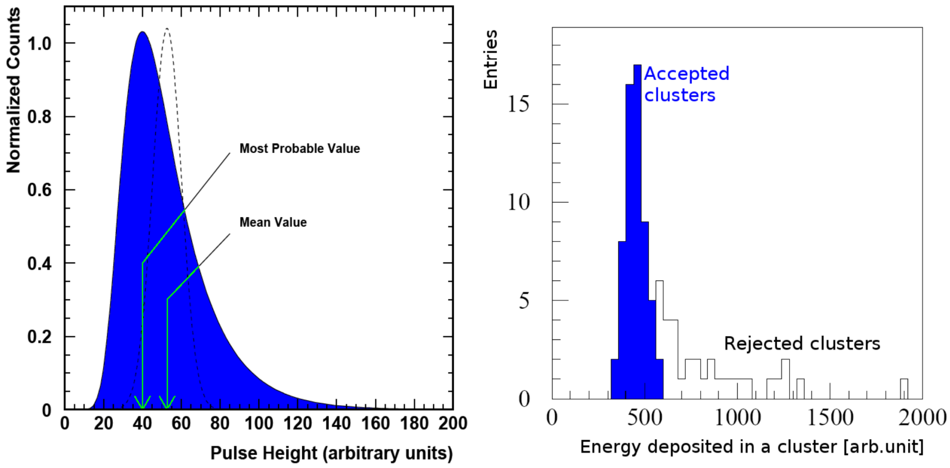

Figure 2.9: *Left*: Landau distribution describing charge distribution in primary ionization clusters marked with the shaded blue area. A gaussian peak of a comparable width is shown with a dashed line for reference. *Right*: A sample distribution of measured cluster energy deposits, showing the principle of the truncation procedure. Small deposit clusters (blue area) are accepted for the energy-loss measurement. Figure taken from Ref. [55].

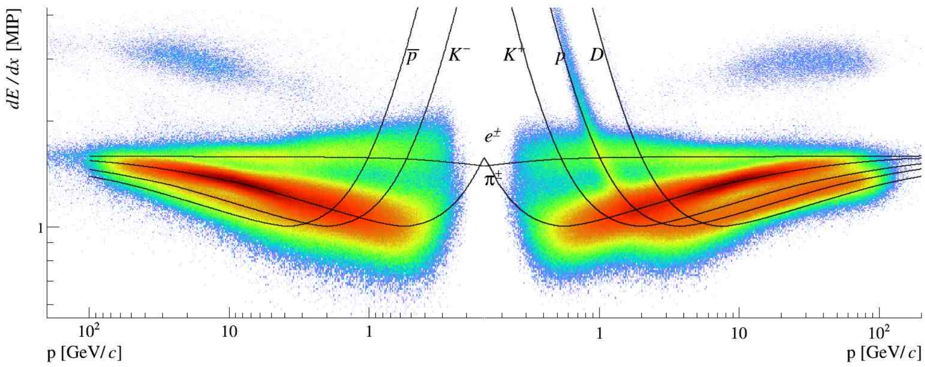

Figure 2.10: Distribution of energy loss versus momentum measured by the NA61/SHINE TPCs in Ar+Sc collisions at 150*A* GeV/*c*. Solid lines show theoretical Bethe-Bloch function (Eq. 2.2) values for different particle species. The clouds visible for $p > 10$ GeV/*c* above the main part of the distribution correspond to heavier fragments produced in Ar+Sc interactions.

A sample energy loss distribution measured by the NA61/SHINE TPCs as a function of particle momentum is shown on Fig. 2.10. The black lines correspond to the Bethe-Bloch (Eq. 2.2) parameterisation for different particle types. In the 1-5 GeV/*c* momentum region Bethe-Bloch curves corresponding to different particles overlap, impeding particle identification. Particle identification is however possible outside this region, even though the distributions corresponding to different particle types overlap (e.g. pion and kaon distribution for $p > 5$ GeV/*c*). Such identification method is referred as the dE/dx identification method.

2.5 Time of Flight detectors

The TPC tracking system is supplemented with detectors capable of time of flight measurements, providing additional and independent particle identification. The left and right ToF walls (ToF-L and ToF-R) are placed behind the MTPCs, symmetric about the beamline. An additional forward ToF detector (ToF-F) was introduced in NA61/SHINE to extend identification capabilities to the forward region for neutrino physics measurements. The ToF-F is placed behind the MTPCs, filling the gap between the ToF-L and ToF-R detectors (see Fig. 2.1). Initially, before the installation of FTPCs, the ToF-F filled the entire available space between ToF-L and ToF-R.

2.5.1 Particle identification

ToF detectors measure the time taken by a particle to travel between the production point and the detector, called t_{flight}. The distance traveled by the particle, l, as well as its momentum p are measured using the reconstructed particle trajectory. In the case of NA61/SHINE this distance is of the order of 14 m. Combining the distance, momentum, and time of flight, it is possible to determine the squared mass of the particle:

$$m^2 = p^2\left(\left(\frac{c \cdot t_{flight}}{l}\right)^2 - 1\right). \tag{2.3}$$

2.5.2 ToF-L and ToF-R

The two ToF-L and TOF-R walls have a total surface area of 4.4 m^2. The schematic layout of the TOF-L wall is shown in Fig. 2.11. Each wall consists of 891 rectangularly-shaped plastic scintillators. A single PMT is glued to the smallest side of each scintillator. The scintillators are formed in three different widths. The shortest ones are placed closest to the beamline, and the width is increased away from the beamline. The largest side is oriented perpendicular to incoming particles. Such configuration provides higher

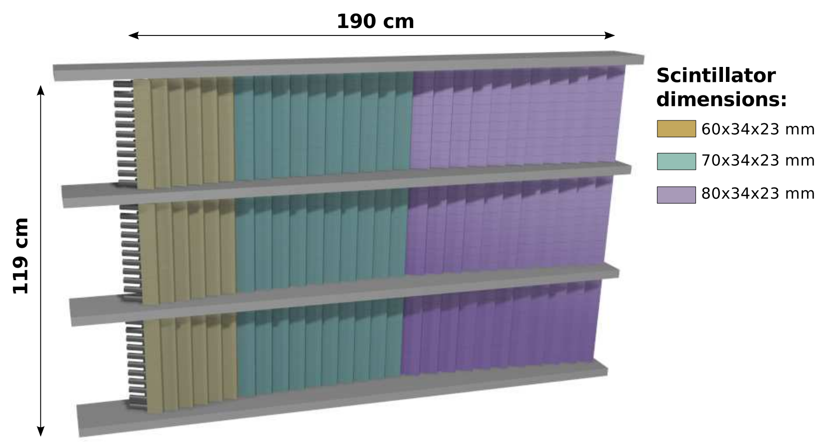

Figure 2.11: Schematic layout of scintillators in the TOF-R detector. TOF-L detector layout is a mirror reflection of the TOF-R with respect to the beam. Figure taken from Ref. [48].

detector granularity in the region with a larger track density. The ToF-L/R detectors are pixelated. Therefore a single scintillator (or a scintillator together with a PMT) will be referred to as *pixel*.

Analog PMT signals are split, with one line going to a charge-sensitive analog-to-digital converter (QDC), while the other one is sent to a CFD followed by the time-to-digital converter (TDC). The TDCs measure time between the start signal provided by the S1 beam counter (see Sec. 2.2.2) and digital signals provided by the CFDs if the amplitude on the input is sufficiently high. The resolution of the timing measurement is of the order of 100 ps for ToF-L and 80 ps for ToF-R. The slight difference in the resolution comes from the fact that the two detectors were built separately with non-identical components (PMTs, readout electronics).

A sample distribution of the squared mass measured by the ToF-L/R detectors as a function of particle momentum is presented in Fig. 2.12. The time resolution reported above is sufficient to separate kaons and pions up to a momentum of around 2 GeV/*c*. Note that negative values of m^2 are also present in the distribution due to the finite measurement resolution. For higher momenta, t_{flight} information is combined with TPC dE/dx measurement, giving the $tof - dE/dx$ identification method. This method supplements the TPC measurements and provides particle identification in the crossover region of the Bethe Bloch curves.

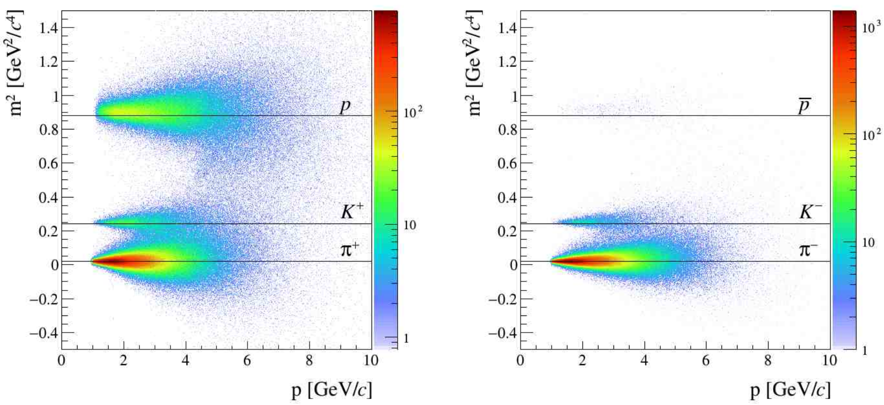

Figure 2.12: A squared mass versus momentum distribution measured by TOF-L (*left*) and TOF-R (*right*) in Ar+Sc collisions at 30*A* GeV/*c*. Solid lines show PDG values for squared masses of different hadrons taken from Ref. [13].

2.5.3 TOF-F

Hadron production measurements for neutrino physics require particle identification in the forward phase space region of particles produced with small polar angles θ, not covered by the TOF-L/R. An additional forward time of flight detector (ToF-F) was constructed to meet those requirements. Initially, the ToF-F consisted of 80 scintillator bars oriented vertically and staggered with 1 cm overlap with respect to each other to ensure complete coverage. The detector filled the gap between ToF-L and ToF-R in the downstream end of the MTPC. Each scintillator bar was equipped with two PMTs at its ends (top and bottom). The readout was very similar to the one used for the ToF-L and ToF-R walls. The detector layout presented in Fig. 2.1

shows the situation after the installation of the FTPCs in 2017, after which the number of ToF-F scintillators was reduced to 16 behind each MTPC. In 2017 the readout electronics was exchanged for a system based on the Domino Ring Sampling version 4 chips (DRS4, [62]). The ToF-F, contrary to the TOF-L/R, features low granularity, which makes it unusable for measurements with a high multiplicity of produced particles. Hence, the ToF-F was not used in Ar+Sc data taking.

2.6 Projectile Spectator Detector

The PSD is a zero-degree hadron calorimeter providing precise measurement of projectile spectators' energy in nucleus-nucleus collisions. Energy deposit measured by the PSD, E_{PSD}, is later used in the offline analysis for the determination of collision centrality (see chapter 5).

A schematic view of the detector is shown in the left panel of Fig. 2.13. The PSD calorimeter consists of 44 modules of varying sizes. 16 smaller modules with dimensions 10×10 cm^2 are located in the central part of the detector. The outer part consists of 28 modules of size 20×20 cm^2. Smaller transverse dimensions of central modules improve the reconstruction of a reaction plane by decreasing the occupancy of a single module. Each module,

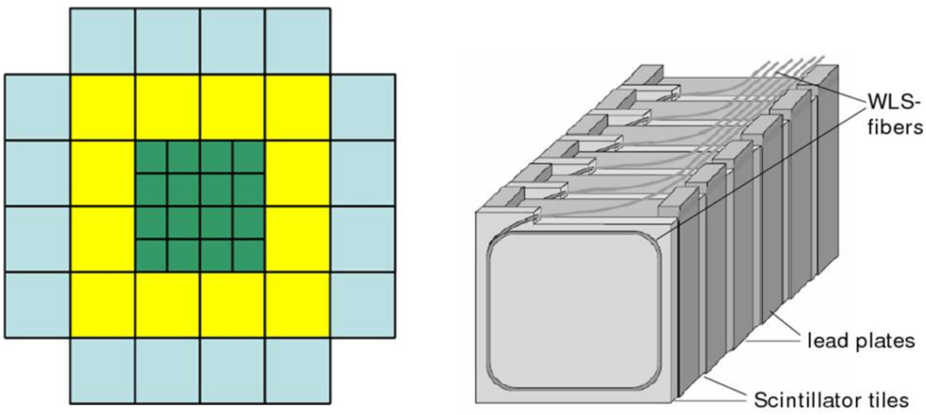

Figure 2.13: *Left*: A schematic view of the PSD front face. *Right*: A schematic view of a single PSD module. Figure taken from Ref. [48].

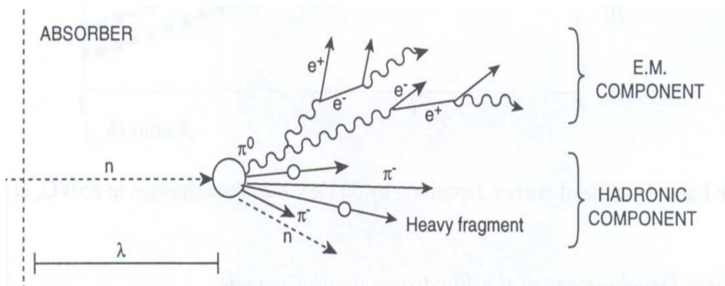

Figure 2.14: An example of the cascade induced by a single neutron. The cascade is composed of hadronic and electromagnetic components. Figure taken from Ref. [30].

schematically shown in the right panel of Fig. 2.13, consists of 60 alternating lead and scintillating layers with 16 mm and 4 mm thickness, respectively. The incident particle hitting the given module produces a particle cascade, visualized in Fig. 2.14. This cascade includes electromagnetic and hadronic components produced in various processes (e.g., ionization, excitation, inelastic interactions). The cascade propagating through the module deposits energy in the detector material, which is sampled by the scintillator plates. Wavelength Shifting optical fibers (WLS-fibers) connect scintillators to light-sensitive readout. The WLS-fibers from each longitudinal section consisting of 6 consecutive scintillator plates are routed to a single connector at the end of the module. An array of 10 Micro-Pixel Avalanche Photodiodes (MAPD) is used to detect light induced in the scintillator material. The emission spectrum of the scintillators is shifted towards shorter wavelengths with respect to the MAPD response spectrum. Therefore the WLS-fibers are used to achieve high detection efficiency. Custom electronics based on flash-ADCs controlled by the FPGA is used for the MAPD signal digitization and processing. The longitudinal segmentation into 10 sections ensures good uniformity in light collection and allows measurement of the longitudinal profile of the generated cascade. Moreover, a signal corresponding to a fast, analog sum of all signals delivered by the selected set of modules can be generated. The amplitude of such signal is proportional to the total energy deposit in the selected fragment of the calorimeter and hence can be used to select event centrality at the trigger level (see Sec. 2.3).

2.7 Small Acceptance Vertex Detector

The SAVD is a silicon pixel detector. It was employed for the first time in NA61/SHINE in 2017 for Xe+La data taking. Precise vertexing provided

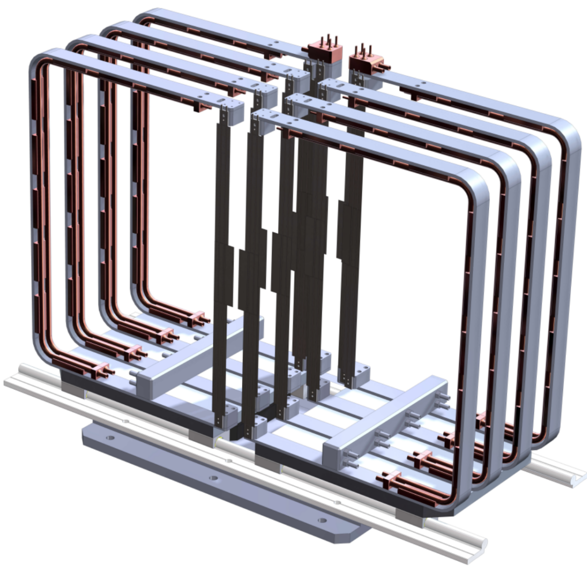

Figure 2.15: A schematic layout of the SAVD. 'C' shaped frames located on two movable arms serve as a mechanical mounting structures for the sensors, limiting amount of the material in the region directly behind the target. Figure taken from Ref. [63].

by the SAVD allows direct measurement of open charm (D^0) production in heavy-ion collisions at the SPS energy range.

The SAVD schematic is shown in Fig. 2.15. It integrates 16 50 µm thick MIMOSA-26AHR [64, 65] sensors with total surface area of ≈ 32 cm^2. Sensors are attached to ultra-light actively cooled carbon fiber structures, which are mounted on two movable arms and are organized in 4 stations. This provides up to 4 measurements per particle track. Despite its small active surface area, the SAVD can detect about 4% of all $D^0 \to K + \pi$ decays at the maximal SPS energy due to the strong forward boost of the particles. As mentioned in section 2.1, the SAVD integrates a target holder with a dedicated movement system.

Chapter 3

Data processing and simulations

Before it is analyzed, data collected by the NA61/SHINE detector are calibrated and reconstructed. In this chapter, a brief description of the reconstruction procedure will be given. Afterward, the NA61/SHINE simulation chain will be discussed.

3.1 Reconstruction

Data collected by the NA61/SHINE detector are stored in the form of *events*. Each event corresponds to a single recorded trigger and comprises digitized signals from all detection system components. Usually, data straight from the detector are referred to as the *raw data*. The reconstruction process translates raw quantities recorded by the detector into particle trajectories and quantities associated with them. An example of a reconstructed ^{40}Ar+^{45}Sc collision is presented of Fig 3.1. Starting with detector raw data, the event reconstruction procedure can be broken into the following steps, performed sequentially:

BPD reconstruction

- A dedicated algorithm extracts positions of the beam particles registered by three BPDs. The three measured points in space are then fit with a straight line, providing the trajectory of the beam particle.

TPC reconstruction

- **Cluster finding.** In the first step, the reconstruction algorithm searches for signals in TPC pads and time-slices. Groups of signals present in adjacent pads and time slices are flagged as clusters. If two distinct maxima are found in the connected charge region, the algorithm assumes they belong to two separate clusters and splits them in two. The position of the cluster is calculated with the center of gravity method using measured charges as weights. Total cluster charge (ADC integral over pads and time slices associated with a given cluster) is also recorded.

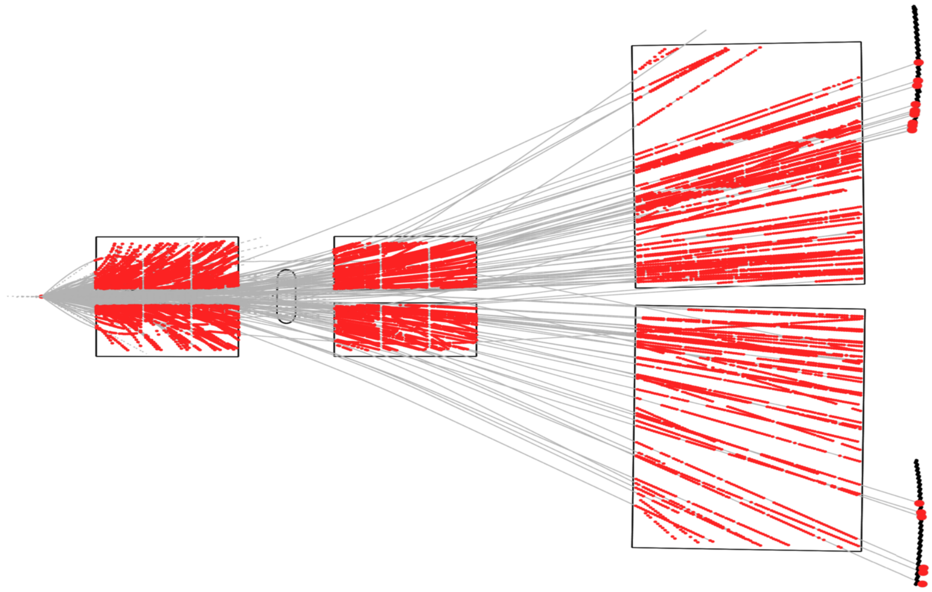

Figure 3.1: An example of reconstructed ^{40}Ar+^{45}Sc collision at 150A GeV/c. Red points denote clusters measured in TPCs and signals in ToF, gray lines - reconstructed tracks (for reference see the detector layout on Fig. 2.1).

- **Local tracking.** The clusters lying in close spatial proximity are merged into local track fragments for each TPC. Apart from the spatial proximity of clusters, a geometrical topology is required: straight lines in MTPCs and curved ones in VTPCs due to the magnetic field.
- **Global tracking.** Local track fragments found in different TPCs are then merged, forming so-called global tracks. Track momentum is determined by the measurement of the track curvature in the known magnetic field configuration. Typical resolution of momentum reconstruction is at the level of $\sigma_p/p^2 = 0.3 \cdot 10^{-4}(\text{GeV}/c)^{-1}$ [49].

Reconstruction of vertices

- **Primary vertex fitting.** The beam particle trajectory measured by the BPDs is extrapolated to the target plane, providing x and y coordinates of the interaction vertex in NA61/SHINE coordinate system (described in Appendix A). All global tracks are extrapolated to the approximate target z-plane ($z = -580$ cm). A global track fit is used to find the z coordinate of the interaction vertex. The vertex fitting algorithm returns a result flag indicating the quality of the fit. The `ePerfect` value marks events with the best quality, and `eBad` the ones in which the fitting procedure failed.
- **Secondary vertex fitting.** The reconstruction algorithm checks each pair of tracks in search of secondary vertices. Usually a secondary vertex distant from the target can be associated with a weak decay of a neutral hadron (e.g., Λ, K^0_S).

TOF reconstruction

- Tracks are extrapolated to the ToF detectors, and matching is performed between the tracks and hits recorded by the ToF readout. The matched tracks are assigned with ToF-related quantities (t_{flight}, m^2, charge recorded by the QDC) in this step.

PSD reconstruction

- As the last step, the raw signals recorded by the PSD readout electronics are translated into energy deposits in sections of modules, single modules, and the whole calorimeter.

As the output of the procedure described above, each event contains information on beam particle trajectory, trigger configuration, energy deposit in the PSD, and a list of tracks. Each track possesses momentum, charge sign, mean energy loss, and the number of measured clusters. Moreover, tracks hitting the ToF detectors will also have time-of-flight related information.

3.2 Monte Carlo simulations

Monte Carlo (MC) simulations are used in the NA61/SHINE to correct analysis results for various effects connected with the detector efficiency, its geometrical acceptance, and performance of the reconstruction algorithms. In order to mimic particle production in a real physical interaction, a MC generator is employed. Based on a study of different MC generators performed for *p+p* data analysis [66], the generator based on Epos1.99 model [67], offering good agreement of model predictions with experimental results and continuous support from the developers, was selected. The other advantage of the Epos model, significant for analysis of ion-ion collisions, is that it provides fragmentation of colliding nuclei. Simulation of the interactions of the generated particles with the detector material is done with the GEometry ANd Tracking (Geant) 3.21 framework [68]. A dedicated detector response simulation is integrated into the NA61/SHINE implementation of the Geant simulation. The simulation output is stored in a format identical to the data recorded by the detector and is then processed by the reconstruction algorithm, identical to the one used for experimental data. Such configuration allows comparison of MC-generated and reconstructed quantities, allowing estimation of the efficiency of the reconstruction procedure, starting from the TPC cluster finding. The output of the described procedure consists of the two components:

- **Generated events, $\mathbf{MC_{gen}}$**: a set of pure simulated events, originating from the MC generator. Information on momenta, species, trajectory, and origin (primary interaction, decay, or secondary interaction) of the produced particles is included.

- **Reconstructed events, $\mathbf{MC_{rec}}$**: generated events are first processed by the detector response simulation based on the Geant package and are then reconstructed in the same manner as the experimental data. MC_{rec} data sample includes most of the information present for reconstructed experimental data (ToF response is not simulated).

A link between reconstructed and generated tracks is provided with a so-called matching procedure. Each reconstructed track is assigned with a generated track with the highest number of geometrically common points along it. The matching procedure also allows to estimate the number of secondary particles wrongly reconstructed as primary ones - so-called feed down.

The NA61/SHINE MC chain does not include the simulation of the ToF detectors. The response of these detectors is driven by efficiency factors individually calculated for each ToF pixel based on experimental data. Each extrapolated MC track hitting the ToF detector is weighted with the appropriate pixel efficiency factor, providing a means to correct for ToF efficiency. This procedure is described in detail in chapter 5.

Chapter 4

Ar+Sc data set

The data on ^{40}Ar+^{45}Sc collisions were collected in 2015 by the NA61/SHINE collaboration during a single data taking campaign. The data were registered at six beam momenta: p_{beam}=13A, 19A, 30A, 40A, 75A and 150A GeV/c. During the Ar+Sc data taking, a common beam and detector configuration was used for all beam momenta. This chapter contains the description of the beam, target, and trigger configurations utilized in the Ar+Sc data taking.

4.1 Beam

The ^{40}Ar beam was created and accelerated by the CERN accelerator complex and finally delivered to NA61/SHINE detector by the H2 beamline (see Sec. 2.2.1). It was a primary beam from the SPS, slowly extracted to the North Area. The SPS cycle consisted of a 10 s spill, during which around 100k ^{40}Ar ions were delivered to the NA61/SHINE, followed by ≈30 s break, resulting in the duty cycle of about 25%.

4.1.1 Beam profile

A set of three BPDs measured each beam particle trajectory in the $x - y$ plane. Fig. 4.1 shows the beam profiles at the target z-plane and divergences for 19A and 150A GeV/c argon beam momenta. The source of horizontal and vertical patterns visible in the beam profiles is the readout strip structure in the BPD detectors. A circular cut-off of the profile is caused by the hole in the V1 counter included in the trigger (see Sec. 2.2.2 and 4.3). Visible broadening of the beam at lower momentum comes from the fact that the H2 beamline was designed to transport heavy-ion and hadron beams at the maximal SPS energy.

4.1.2 Time structure

The beam extracted to NA61/SHINE has a flat time structure. Such a beam property is desirable because it ensures that the contribution of so-called pileup events, where the detector registers interaction of more than one beam particle in a single event, is minimal. The time structure of the beam recorded on the S1 counter is presented in Fig. 4.2.

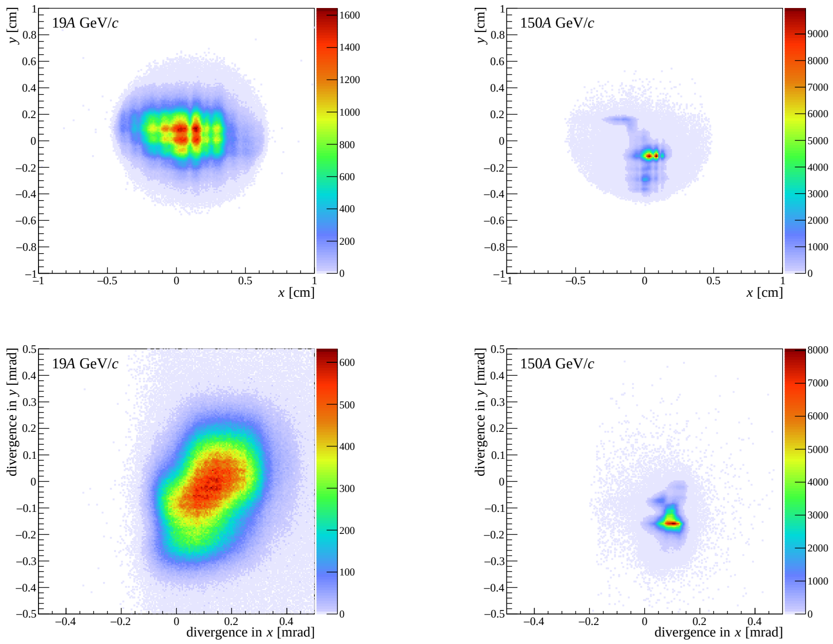

Figure 4.1: *Top*: The beam profiles at the target z-plane for 19A (*left*) and 150A (*right)* GeV/c beam momentum. Straight lines fitted to points measured by the BPDs are extrapolated to z=-580cm (target position). *Bottom*: The beam divergence (angle between the fitted beam track and the z axis) for 19A (*left*) and 150A (*right)* GeV/c beam momentum. Structures visible on the plots correspond to the topology of the BPD readout (see Sec. 2.2.2).

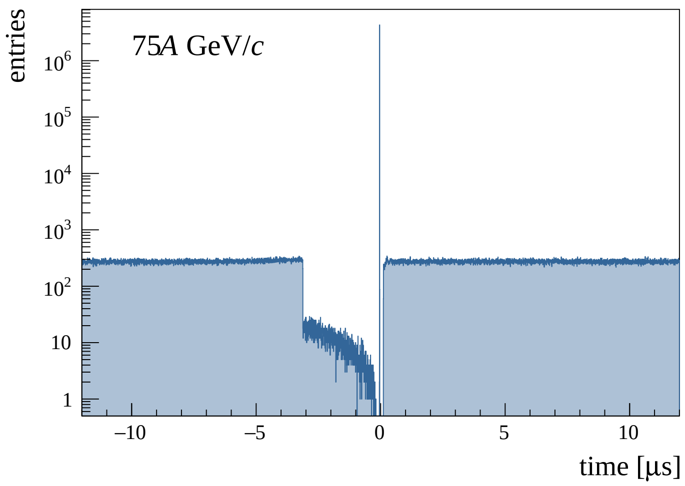

Figure 4.2: The time distribution of beam particles hitting the S1 detector close in time to the triggering particle for the Ar beam at 75A GeV/c. The region of ±11 μs around the triggering particle at t = 0 is shown.

The sharp peak at t=0 corresponds to the triggering beam particle. The small gap after the trigger is caused by the fact that the width of discriminated S1 signal is around 100 ns, and the system does not register any particles in this time window after the triggering one. The source of the wider depletion region on the time structure plot preceding the trigger is the ToF readout electronics. The ToF TDCs are started with an S1 signal (see Sec.

2.5) without a full trigger decision. When an accepted readout trigger does not follow the S1 signal, the TDCs must be cleared (a so-called fast-clear mechanism). The fast clear of TDCs takes around 3 μs, during which ToF readout is *busy* (no triggers can be accepted). As a result, a fast-clear mechanism demands no S1 signals for about 3 μs before the trigger. The particles present in this time window, visible in Fig. 4.2, originate from configurations where an additional beam particle was present *during* the process of ToF fast-clear. The rest of the time structure histogram is flat ($t < 3$ μs and $t > 0.1$ μs), indicating a uniform random distribution of the beam particles in time.

4.2 Target

The target used in Ar+Sc data taking was a stack of 6 square ^{45}Sc plates of 2.5×2.5 cm^2 area and 1 mm thickness. The target was placed at z=-580 in a dedicated helium-filled container equipped with a pneumatic movement system (see Sec. 2.1). The purity of the scandium target was measured at Jan Kochanowski University in Kielce, Poland using the WDXRF method. The content of ^{45}Sc in the target was at the level of 99.3%. The most abundant impurities in the target were identified to be: Ti (0.16%), Al (0.14%) Fe (0.13%), Cu (0.07%), and Ta (0.07%). The influence of these other elements on the mean multiplicity of negatively charged particles in the SPS energy range was estimated to be less than 0.2% [69]. The effect on the positive particle multiplicity was assumed to be on the same level. Corresponding contribution to the systematic uncertainty of the final results presented in this thesis was neglected, as it is more than one order of magnitude smaller than the estimated systematic uncertainty coming from other sources (see Sec. 5.6.2).

The data were taken using two target configurations: target inserted (target IN) and target removed (target OUT). Approximately 90% of accumulated statistics was collected with target IN. The target OUT data was collected to correct for interactions of beam particles with the material surrounding the target (off-target interactions). Table 4.1 summarizes the statistics collected for all six momenta of the Ar beam.

Beam momentum [GeV/c]	Target IN	Target OUT
13A	$3.9 \cdot 10^6$	$2.3 \cdot 10^5$
19A	$4.2 \cdot 10^6$	$2.3 \cdot 10^5$
30A	$5.2 \cdot 10^6$	$2.6 \cdot 10^5$
40A	$1.0 \cdot 10^7$	$8.7 \cdot 10^5$
75A	$4.8 \cdot 10^6$	$2.9 \cdot 10^5$
150A	$3.7 \cdot 10^6$	$2.3 \cdot 10^5$

Table 4.1: A summary of the statistics collected during Ar+Sc data taking campaign

4.3 Trigger

The trigger during Ar+Sc data taking was derived from signals produced by the detectors schematically shown on Fig. 4.3. Beam counters marked in green were used in coincidence, while the detectors marked in red served as vetos. Four trigger patterns were defined during this data taking campaign: *beam* trigger, *central interaction* trigger, *beam halo* trigger, and *minimum bias interaction* trigger. The trigger definitions in terms of signal (anti-) coincidences are summarized in table 4.2. Trigger definitions were common throughout the whole data taking. However, signal delays and discriminator thresholds were fine-tuned for each collected beam momentum.

Name	Definition	Description	Fraction of data
T1	$S1 \cdot S2 \cdot \overline{V1}$	beam	1.16%
T2	$S1 \cdot S2 \cdot \overline{V1} \cdot \overline{S5} \cdot \overline{\mathrm{PSD}}$	central interaction	92.61%
T3	$S1 \cdot S2$	beam halo	0.18%
T4	$S1 \cdot S2 \cdot \overline{V1} \cdot \overline{S5}$	min. bias interaction	7.13%

Table 4.2: A list of trigger definitions used during Ar+Sc data taking. The rightmost column shows a fraction of data corresponding to an unbiased sample of a given trigger type.

Data sample proportions corresponding to the triggers used during data taking were set with prescaling factors (see Sec. 2.3). Fractions of data stored on a disk containing prescaled samples of given triggers are listed in table 4.2. Most of the data sample consists of central interaction triggers. Additionally, a small amount of beam and minimum bias triggers was collected for monitoring and cross-section analysis. Notably, the sum of all fractions exceeds 100%, as, for example, some prescaled T1 triggers also belong to the group of prescaled T2 triggers.

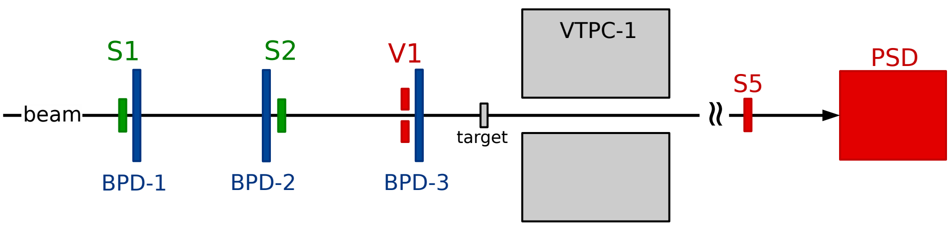

Figure 4.3: A schematic layout of the beam and trigger detectors used during Ar+Sc data taking. Elements working in coincidence mode are marked with green color, the ones working as vetos with red color.

Chapter 5

Analysis

The analysis procedure of the ^{40}Ar+^{45}Sc dataset (described in chapter 4) is thoroughly discussed in this chapter. The analysis input constitutes a set of calibrated and reconstructed ^{40}Ar+^{45}Sc events at 13*A*, 19*A*, 30*A*, 40*A*, 75*A*, and 150*A* GeV/*c* beam momenta. First, the analysis acceptance is defined (Sec. 5.1). The actual analysis starts with event (Sec. 5.2) and track (Sec. 5.3) selection, providing a high quality data sub-sample for the following analysis steps. Then, particle identification is performed using the $tof - \mathrm{d}E/\mathrm{d}x$ method (Sec. 5.4). Subsequently, MC correction factors are calculated and applied, leading to final particle production spectra (Sec. 5.5). The analysis procedure is concluded by calculating statistical uncertainties and estimating the systematic ones (Sec. 5.6). The final results presented as two-dimensional multiplicities of charged hadrons as a function of rapidity y and transverse momentum p_T are shown in chapter 6. Section 5.7 describes alternative approaches to the analysis of Ar+Sc data.

5.1 Acceptance

The kinematic region in which particle identification with the $tof - \mathrm{d}E/\mathrm{d}x$ analysis is possible is determined by detector geometry and the analysis technique itself. Particle production spectra are presented in $y - p_\mathrm{T}$ space, while the geometry of (mainly) ToF detectors selects a particular fragment of the momentum $p - p_\mathrm{T}$ phase space, independently of the particle type. An example of acceptance of the $tof - \mathrm{d}E/\mathrm{d}x$ analysis method in both mentioned phase spaces for the most abundant charged hadrons produced in Ar+Sc collisions is presented in Fig. 5.1. The gray shaded area denotes the phase space region accepted due to detector geometry under a particular magnetic field configuration. The phase space region selected for analysis (meshed blue area) is limited by additional conditions imposed in momentum space originating from the analysis technique (see Sec. 5.4). The corresponding accepted rapidity - transverse momentum region, together with the binning used in the analysis, is shown for K, π, and p. The binning choice is arbitrary and compromises phase space granularity and statistics accumulated in a single bin. Bins located on the edges of acceptance may be sparsely populated. Although this effect is taken into account during calculation of the MC corrections, bins having less than 30% overlap with the acceptance are discarded from the analysis. The magnetic field for different beam momenta from the range available at the SPS is set such that the ToF acceptance coincides with the mid-rapidity region of charged kaons.

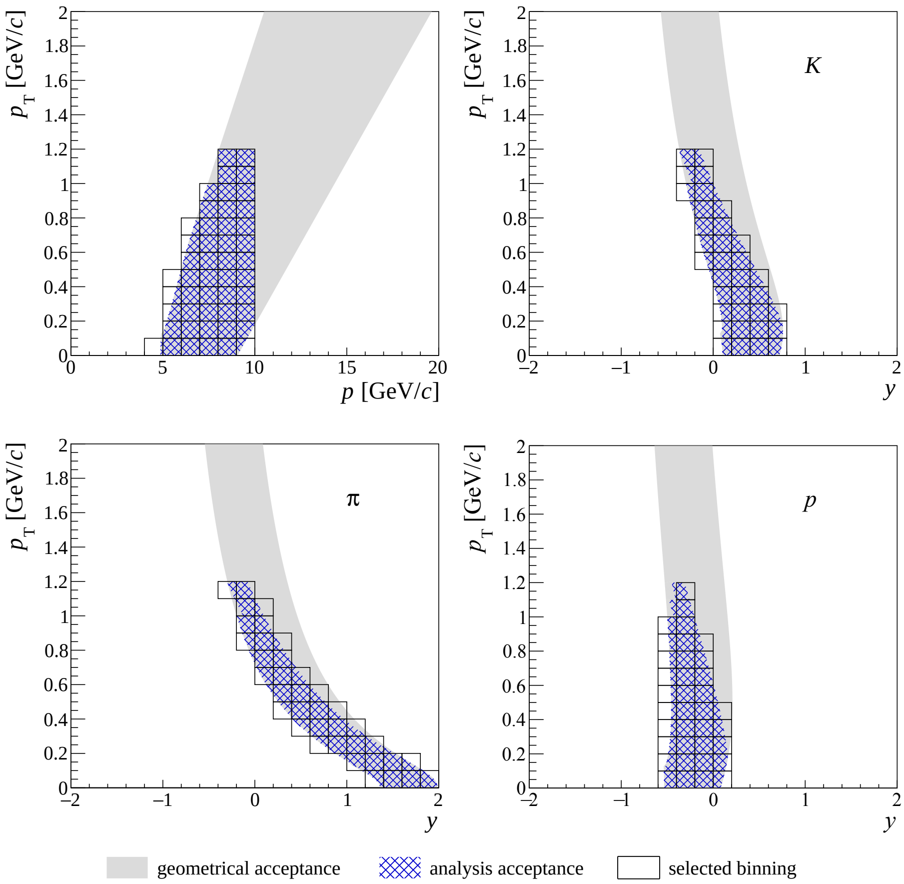

Figure 5.1: Example of the $tof - dE/dx$ analysis acceptance for $150A\,\text{GeV}/c$ presented in $p - p_T$ space (*top left*) and $y - p_T$ space for kaons (*top right*), pions (*bottom left*) and protons (*bottom right*). Gray shaded area denotes the geometrical acceptance of the TPC-ToF detection system. Blue mesh represents region accepted for the analysis in bins defined by the solid black lines.

5.2 Event selection

The sub-sample consisting of central interactions of ^{40}Ar beam ions with ^{45}Sc target nuclei selected on the trigger level - T2 triggers - was analyzed. A sequence of event selection criteria was imposed on the T2 trigger sample, ensuring the highest quality of the analyzed data and proper, well-defined event centrality interval. The applied criteria can be sub-divided into two groups. The first group consists of criteria concerning beam properties - non-biasing event selection, while the second one concerns off-target interactions, reconstruction capabilities, and event centrality selection - biasing selection criteria.

5.2.1 Non-biasing event selection criteria

The group of non-biasing event selection criteria consists of:

1. Beam quality
2. Beam off-time

The criteria are applied sequentially in the order they are listed. Their application selects events with a well-measured beam particle trajectory, providing there was only a single interaction of the beam ion with the target.

Beam quality

A precise measurement of the beam particle trajectory is required. The presence of the signal from BPD-3 (closest to the target), together with a signal from either of the other beam position detectors (BPD-1 or BPD-2) is required. Such conditions allow the fitting of the beam trajectory and its extrapolation to the target area. Furthermore, it also provides that the beam particle did not interact upstream of the BPD-3.

Beam off-time

This criterion reduces the contribution of events in which there was an additional beam particle, which could interact with the target or the detector material in close time proximity to the triggering particle. All events with an additional beam particle occurring within ±4 μs or a minimum bias interaction within ± 25μs window around the triggering particle were excluded from the analysis. Off-time particle registration has a dead time of around 100 ns (see Sec. 4.1.2). The possible contamination of the data sample by off-time interactions not registered by the MHTDC was estimated to be at the level of 0.01%. It was neglected during estimation of the systematic uncertainty, as it is several orders of magnitude lower than other contributions (see Sec. 5.6.2).

5.2.2 Biasing event selection criteria

The criteria presented in this section concern selection of events based on reconstructed quantities and should be considered as potentially biasing. The selection procedure includes:

1. Reconstructed interaction vertex properties
2. Event centrality

Reconstructed interaction vertex properties

This analysis concerns charged particles produced in primary ^{40}Ar+^{45}Sc interactions. Two interaction vertex quality criteria are imposed on the data.

The first one selects only events for which primary vertex reconstruction was successful with the best fit quality (`ePerfect`, provided by the reconstruction procedure). As described in section 3.1, x and y components of the interaction vertex position are taken from the BPD trajectory fit, while the z position is fitted with tracks of secondary particles.

The second one concerns the z-position of the interaction vertex. A sample distribution of interaction vertex z-positions for 150A GeV/c beam momentum is shown in Fig. 5.2. The plot presents distributions for target inserted (IN) and target removed (OUT) data sets. Target removed distribution was normalized to agree with the target IN distribution for $z < -640$. Events with a primary vertex position within ±10 cm around the target, marked

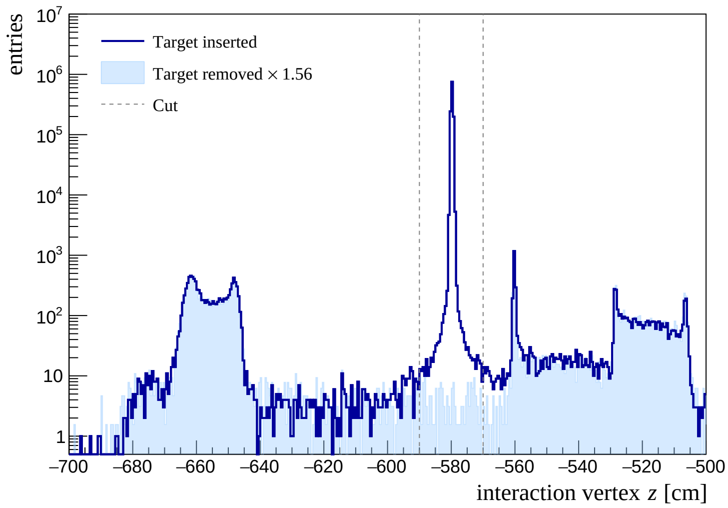

Figure 5.2: Primary vertex position along the beam axis for 150*A* GeV/*c* beam momentum. Solid blue line represents target IN data. The shaded area corresponds to scaled-up target OUT data. The dashed lines present the range of values accepted for the analysis.

with dashed lines, were accepted for the analysis. The broadening of the peak corresponding to the interactions inside the target is caused by the finite resolution of the vertex reconstruction. Other maxima visible in the distribution in Fig. 5.2 correspond to the detector components surrounding the target area. Note that the target OUT distribution does not show the peak corresponding to interactions inside the target, leaving only the structures coming from the detector components.

Centrality selection

The analysis presented in this thesis concerns 10% of the most *central* ^{40}Ar+^{45}Sc collisions. A brief description of the procedure defining *central* collisions is given in this section. A detailed discussion of the procedure can be found in Refs. [35, 70, 71].

Event centrality for experimental data was derived from the measurements of the PSD calorimeter. The PSD measures the energy of projectile spectators (nucleons and nuclear fragments) and the energy of produced particles within its geometrical acceptance. The more central the event, the less energy is carried by the spectators. Hence less energy is deposited in the PSD. During data taking, an integrated analog signal from the 16 central PSD modules was included in the T2 trigger definition (see Fig. 5.3 and Sec. 4.3). The discriminator was tuned to select ≈30% of the most central Ar+Sc collisions independently for each beam momentum. A dedicated procedure allowing precise centrality determination based on PSD measurements was developed and is described below.

The first step in centrality determination is to select PSD modules in which the energy is deposited primarily by projectile spectators. A correlation between energy deposit in a given module and the total multiplicity of particles produced in the event (registered in TPCs) is studied to select such

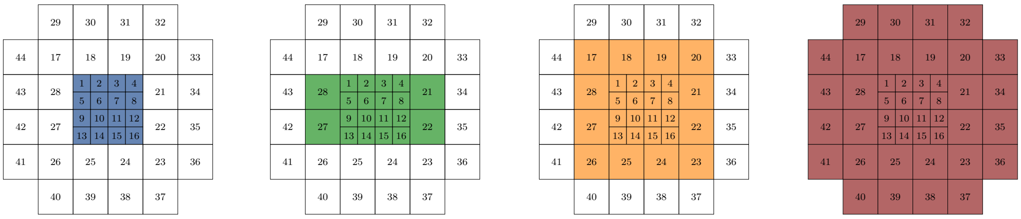

T2 trigger — 150*A* GeV/*c* — 30*A*, 40*A*, 75*A* GeV/*c* — 19*A*, 13*A* GeV/*c*

Figure 5.3: PSD modules used in the online and offline event selection. The T2 trigger is derived from the energy deposited in the central 16 modules, while the set of modules used to determine the PSD energy E_{PSD} varies with beam momentum.

modules. An example of this correlation for two PSD modules is presented in Fig. 5.4. A positive correlation, visible in the right panel of Fig. 5.4, suggests that produced particles contribute the most to the energy deposited in the given module. On the other hand, a desired negative correlation, visible on the left panel of the same figure, indicates that the module is occupied mainly by the spectators. To be more precise, it indicates that the energy in the given module is deposited mainly by the projectile spectators. Fig. 5.3 shows the PSD modules used in the offline centrality selection for all analyzed beam momenta. Spectator occupancy of the PSD modules established with this method was later verified with MC simulations. The energy measured by selected PSD modules will be further referred to as E_{PSD}.

The E_{PSD} values defining specific centrality intervals are identified with the use of a specially-prepared sample of minimum bias data, a subset of the T1 beam triggers. The minimum bias sample is selected by requiring the presence of a reconstructed vertex in the target vicinity, i.e., the interaction of a beam particle inside the target. Measured distributions of E_{PSD} for minimum-bias and T2-selected events for 19*A* and 150*A* GeV beam momenta are shown in Fig. 5.5. The two distributions were normalized to agree in the region of small energy deposits, marked with a dashed line.

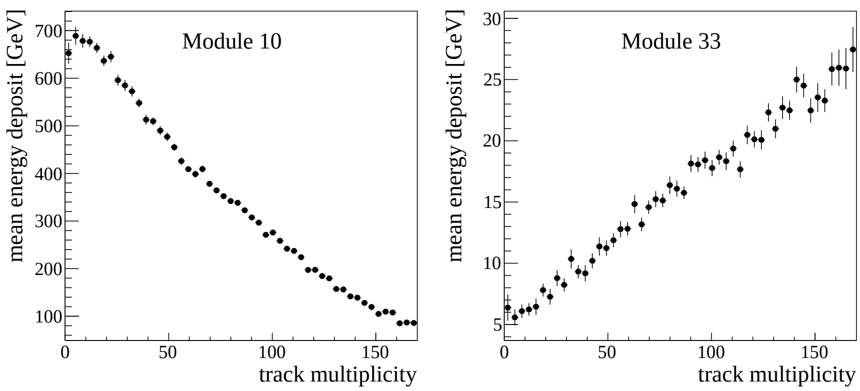

Figure 5.4: The mean energy deposit measured by module 10 (dominated by projectile spectators, *left*) and module 33 (dominated by the produced particles, *right*) of the PSD (see Fig. 5.3 for the numbering scheme) as a function of particle multiplicity measured in TPCs in Ar+Sc collisions at 150*A* GeV/*c*. Distributions correspond to a sample of minimum bias (T4 trigger) Ar+Sc collisions.

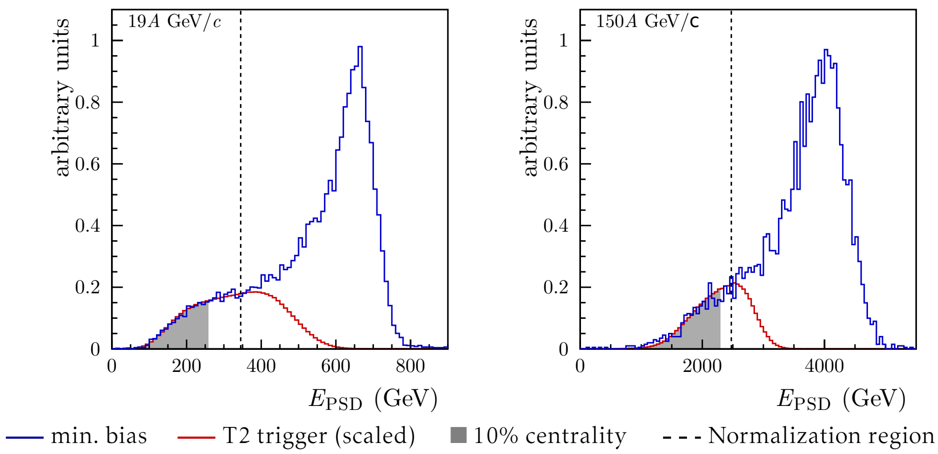

Figure 5.5: Event centrality selection using the energy $E_{\rm PSD}$ measurement. Distributions are shown for minimum-bias selected (blue histograms) and T2 selected (red histograms) events for 19A (left plot) and 150A GeV/c (right plot) beam momentum. Histograms are normalized to agree in the overlap region (limited by the black dashed line). The accepted region corresponding to the 10% collisions with the smallest $E_{\rm PSD}$ is indicated by shaded area.

The shaded area depicts the region of 10% Ar+Sc events with the smallest measured $E_{\rm PSD}$, called "10% of the most *central* Ar+Sc events". The values of the threshold energies $E_{\rm PSD}^{cut}$ defining 10% centrality are listed in table 5.1.

To enable comparison of experimentally-obtained *centrality* selection criteria with theoretical models and MC simulations, a three-dimensional acceptance map was created [73]. The map describes the acceptance of the PSD detector as a function of momentum p, transverse momentum $p_{\rm T}$, and azimuthal angle ϕ of the produced particle in the laboratory frame of reference. The map allows calculation of the forward energy $E_{\rm F}$, the energy carried by all particles within the PSD acceptance, without any knowledge of the NA61/SHINE detector geometry. The *central* events are defined as 10% of the events with smallest $E_{\rm F}$. The centrality of all events simulated with different theoretical models used for comparison in chapter 6 was selected with this procedure.

$p_{\rm beam}$ [GeV/c]	13A	19A	30A	40A	75A	150A
$\langle\pi^-\rangle_{E_{\rm F}}$	43.69	51.63	64.11	70.68	84.70	103.97
$\langle\pi^-\rangle_{E_{\rm PSD}}$	43.47	51.42	64.00	70.43	84.29	103.66
$\langle\pi^-\rangle_{E_{\rm F}}/\langle\pi^-\rangle_{E_{\rm PSD}}$	1.005	1.004	1.002	1.004	1.005	1.003
$E_{\rm PSD}^{cut}$ [GeV]	142.7	264.2	446.4	665.6	1290.6	2276.0

Table 5.1: The numerical values of the mean π^- multiplicities for the two selections of the 10% of the most central Ar+Sc collisions in the simulated data done with $E_{\rm F}$ and $E_{\rm PSD}$. The ratio of the two multiplicities is also listed. The multiplicity values come from Ref. [72]. The last row lists the PSD energy thresholds. The 10% centrality is selected by $E_{\rm PSD} < E_{\rm PSD}^{cut}$ criterion.

MC simulations were performed to study a potential bias on centrality selection caused by the finite resolution of the PSD and other detector effects. First, a minimum bias EPOS data sample was generated. Next, the centrality of simulated events was selected in two ways, with one method using E_{F} calculated with the acceptance map and the other using simulated PSD response E_{PSD}. Then, the mean multiplicities of π^- obtained from the two centrality-selected sub-sets of the EPOS data were compared. The results are summarised in table 5.1. The differences in the π^- mean multiplicities with the two centrality selections range from 0.2% to 0.5%. According to the WNM (see Sec. 1.4.1 and Ref. [29]), the mean multiplicity of produced particles scales with the mean number of wounded nucleons $\langle W \rangle$ for a given centrality selection. The differences in $\langle W \rangle$ for the two centrality selections are small and therefore WNM scaling is assumed to be valid. Thus, the same relative scaling is expected for $K^{\pm}$, p, $\bar{p}$, and π^+, as the one determined for π^-. In summary, the maximal bias on the final results introduced by the centrality selection was estimated to be less than 0.5%. This value is an order of magnitude smaller than other estimated contributions to the systematic uncertainty (discussed in Sec. 5.6.2) and is therefore neglected in the final uncertainty calculation.

5.2.3 Experimental data and Monte Carlo statistics

Event selection criteria presented in this section were applied to target OUT and target IN data. Furthermore, biasing criteria were also applied to the reconstructed MC data. Statistics of data collected with both target configurations and generated MC sample, before and after event selection, is presented in table 5.2. Since the selected target OUT samples consist of less than ten events per energy (order of a few parts-per-million of the target IN statistics), the contribution of the off-target interactions is estimated to be negligible.

p_{beam}	Target IN		Target OUT		EPOS	
[GeV/c]	before selection	after selection	before selection	after selection	before selection	after selection
13A	$3.9 \cdot 10^6$	$5.0 \cdot 10^5$	$2.3 \cdot 10^5$	1	$3.9 \cdot 10^6$	$7.9 \cdot 10^5$
19A	$4.2 \cdot 10^6$	$5.3 \cdot 10^5$	$2.3 \cdot 10^5$	5	$4.9 \cdot 10^6$	$4.9 \cdot 10^6$
30A	$5.2 \cdot 10^6$	$9.1 \cdot 10^5$	$2.6 \cdot 10^5$	0	$9.2 \cdot 10^6$	$9.2 \cdot 10^5$
40A	$1.0 \cdot 10^7$	$1.3 \cdot 10^6$	$8.7 \cdot 10^5$	3	$5.0 \cdot 10^6$	$5.0 \cdot 10^5$
75A	$4.8 \cdot 10^6$	$1.1 \cdot 10^6$	$2.9 \cdot 10^5$	9	$2.0 \cdot 10^7$	$2.0 \cdot 10^6$
150A	$3.7 \cdot 10^6$	$1.1 \cdot 10^6$	$2.3 \cdot 10^5$	2	$6.5 \cdot 10^6$	$6.5 \cdot 10^5$

Table 5.2: A summary of the statistics collected during Ar+Sc data taking campaign.

5.3 Track selection

This section describes the track selection criteria imposed on the reconstructed particle tracks. Analysis is performed on so-called primary tracks, which originate from the main reconstructed interaction vertex.

Track selection criteria are divided into two groups. *Standard track selection criteria* are widely used in the NA61/SHINE community during the analysis of different data sets. Particular cut values of the selection criteria were tuned to the Ar+Sc data sample. The analysis of the time of flight detector data requires an additional set of quality criteria: *ToF-related selection criteria*.

The selection criteria described in this section are applied sequentially in the order they are described.

5.3.1 Standard track selection criteria

Standard track selection criteria include:

1. Impact point
2. Number of reconstructed clusters
3. Track topology

Impact point

The distance between the track extrapolated to the target z-plane and the reconstructed vertex is called the impact point $\vec{b}$. Tracks accepted for further analysis are expected to have absolute values of horizontal (b_x) and vertical (b_y) impact point components smaller than 4 cm and 2 cm, respectively. Fig. 5.6 shows example distributions of b_x (left panel) and b_y (right panel). Values satisfying the criterion are marked with shaded areas. This condition reduces the contribution of particles originating from weak decays of neutral hadrons, which are typically not well extrapolated towards the main interaction vertex.

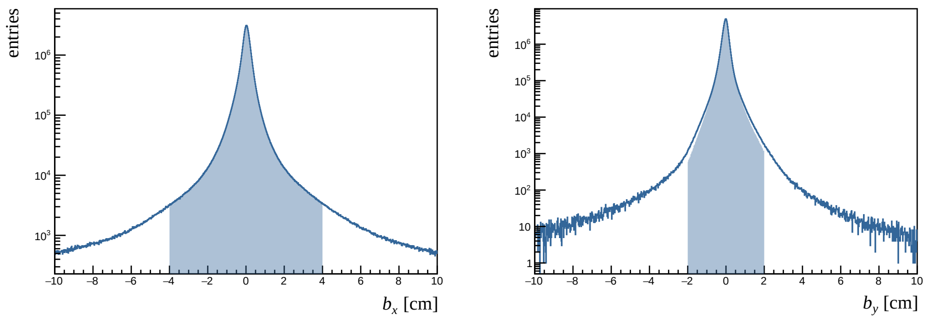

Figure 5.6: Example distributions of b_x (*left*) and b_y (*right*) impact point components for ^{40}Ar+^{45}Sc interactions at 150*A* GeV/*c* beam momentum before (blue line) and after (shaded area) application of the impact point selection criterion.

Number of clusters

A minimal number of measured clusters on a track is required to ensure a good reconstruction of momentum and reliable measurement of the mean energy loss.

Tracks are accepted if the number of clusters measured in the VTPCs is larger than 15 to ensure proper momentum reconstruction and simultaneously, the total number of measured clusters is greater than 30 for an adequate energy loss measurement.

Track topology

Reconstructed tracks in NA61/SHINE are customarily divided into two groups, so-called right-side-tracks (RSTs) and wrong-side-tracks (WSTs). The RST is defined using the following relation:

$$p_x \cdot q > 0 \tag{5.1}$$

where q is the charge sign of the particle and p_x is the momentum component along the x axis. WSTs is the class complementary to RSTs, defined with $p_x \cdot q < 0$. The magnetic field is anti-parallel to the y axis, so RSTs are always bent in the direction of p_x, therefore away from the beamline. Example RST and WST are presented in Fig. 5.7.

The topology of the readout in the NA61/SHINE is optimized for the detection of RSTs (see Sec. 2.4 and Ref. [49]).Therefore, only RSTs are accepted for this analysis.

5.3.2 ToF-related selection

The selection procedure strictly related to the *tof* − dE/dx analysis of Ar+Sc data concerns:

1. Last point of the track measured in TPCs
2. ToF detector acceptance

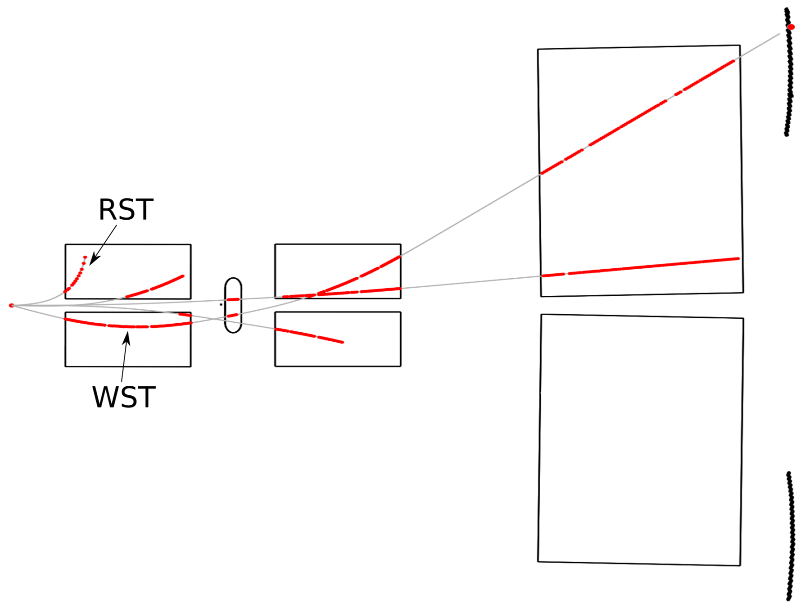

Figure 5.7: Example of a right-side- and a wrong-side-tracks in a reconstructed event.

3. ToF TDC/QDC signal quality
4. ToF pixel efficiency

Last point in TPCs

The tracks measured by the TPCs are extrapolated towards the ToF detectors. The last point measured on the particle trajectory is required to be located in the most downstream sectors of the MTPC-L or MTPC-R at $z > 650$ cm. Additionally, the residual distance, $\vec{d}$, between the reconstructed particle trajectory (global track) and the last point measured on the track by the MTPC (mentioned above) was restricted. Fig 5.8 shows a sample distribution of such residual distances. Tracks accepted for the analysis with $|\vec{d}| < 4$ cm are marked with the red circle. These conditions provide reliable extrapolation of the MTPC trajectories toward the ToF detectors.

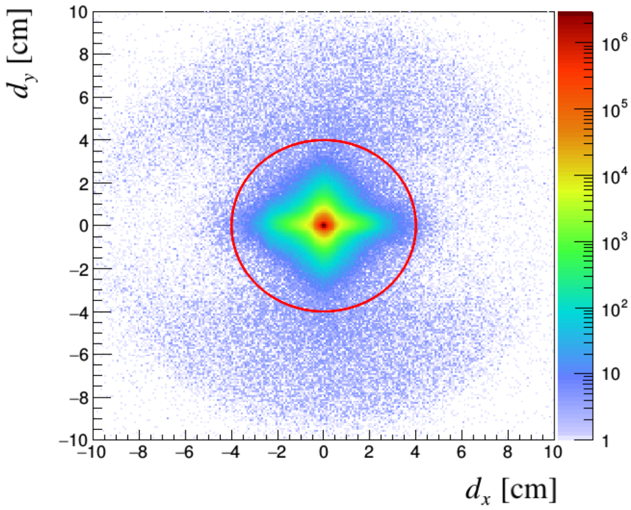

Figure 5.8: A sample distribution of residuals between the reconstructed track and the last measured point in the TPCs for 75*A* GeV beam momentum. The inside of the red circle represents the tracks accepted for analysis.

ToF detector acceptance

A straight line is fitted to 10 last points measured by the MTPCs on each track, satisfying the *last point in TPCs* selection criterion. The track is accepted for the analysis if the extrapolated straight line hits at least one scintillator of the ToF-L/R walls and TDC/QDC signals from the corresponding pixel are present.

ToF TDC/QDC signal quality

The selection of high-quality ToF data is utilized. It concerns raw values of measured timing (TDC) and charge (QDC) for a particular hit. Hits with overflow TDC values (value exceeding the range of the converter) are excluded. Most of such hits come from particles generated in the off-time interactions happening after the readout trigger. An off-time interaction occurring before the triggering particle would result in presence of the TDC *stop* signal before the *start* signal (effectively, absence of the *stop* signal), leading to TDC overflow condition.

The normalized QDC (QDC_{norm}) is a dimensionless quantity created from QDC measurements of all pixels in a given ToF wall. The normalization procedure scales the QDC response linearly, effectively shifting pedestal (no hit) and signal (hit present) values to 0 and 1, respectively. An example distribution of normalized QDC is presented in Fig. 5.9. The hits are accepted for the analysis if the QDC_{norm} is greater than 0.5 and smaller than 2, as shown on the plots with dashed lines. Rejected values of $QDC_{norm}<0.5$ correspond to particles hitting edges of the ToF scintillators, producing low amplitude signals. Values exceeding 2, on the other hand, may be caused by a heavy fragment or more than one particle hitting the pixel. Both cases are excluded, as the heavier fragments are not of interest to this analysis, and multiple hits in a single pixel prevent unambiguous assignment of timing information to the particle tracks.

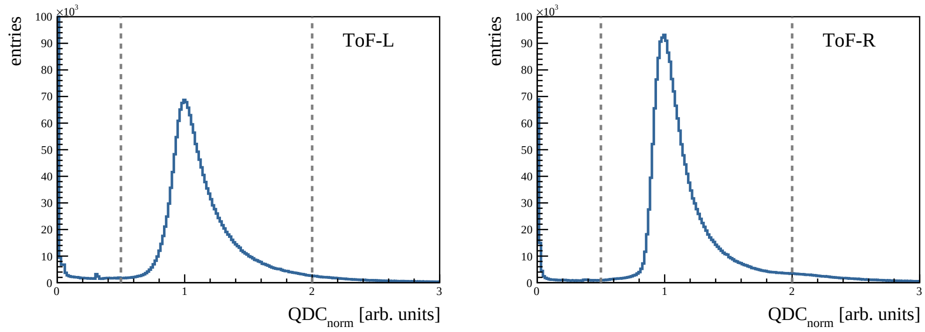

Figure 5.9: An example distribution of the normalized QDC of hits from ToF-L (*left*) and ToF-R (*right*) for 150*A* GeV beam momentum. Dashed lines indicate the quality cut values.

ToF efficiency

After the application of, described above, ToF-related track selection criteria, efficiencies of all ToF pixels are calculated independently based on the experimental data. The k-th pixel efficiency ϵ_k is defined as follows:

$$\epsilon_k = \frac{ToFhit_k^{good}}{ToFhit_k^{all}}, \tag{5.2}$$

where the denominator denotes the number of extrapolated MTPC tracks hitting a given pixel, the numerator counts tracks passing the described ToF quality criteria. Pixels with efficiency smaller than 50% were recognized as inefficient and unreliable. Hence, all particles hitting inefficient pixels were not taken into account in the analysis.

5.4 Particle identification

Identification of charged particles produced in inelastic Ar+Sc collisions for the purpose of this thesis was performed with the use of the ToF information, which provides m^2 values of the produced particles, combined with the energy loss measurement in the TPCs, giving the *tof* – dE/dx identification method. For low momentum particles (p<2 GeV/c), identification was based on the m^2 measurements, whereas in the higher momentum region (p>2 GeV/c), the ToF information was combined with the dE/dx measurement. Both approaches will be discussed in this section.

5.4.1 *tof* – dE/dx method

Low momentum particles

As stated in Sec. 2.5, the resolution of the NA61/SHINE time-of-flight measurement is sufficient to separate different produced hadron species up to momenta of around 2 GeV/c. The distribution of m^2 as a function of particle momentum for 19A GeV/c beam momentum is presented in the left panel of Fig. 5.10. The dashed vertical line marks the applicability limit of this method. Hadron type, p, π or K, is assigned to a particle based on the m^2 measurement and pre-defined intervals, shown with red horizontal lines and summarized below:

$$\begin{aligned} I_\pi &= [-0.10, 0.17[\ \text{GeV}^2/c^4 \\ I_K &= [0.17, 0.50[\ \text{GeV}^2/c^4 \\ I_p &= [0.50, 1.30[\ \text{GeV}^2/c^4 \end{aligned} \tag{5.3}$$

In this approach, identified pions can be contaminated with electrons, as their small squared-mass difference $m_\pi^2 - m_e^2$=0.018 GeV$^2/c^4$ makes them indistinguishable with the m^2 measurement only (see Fig. 5.11 in the next section). Electrons are removed imposing dE/dx <1.4 cut, presented in the right panel of Fig. 5.10. The dE/dx cut is applied only for particles passing the pion m^2 criterion, in order not to influence protons, with their high dE/dx values in this low momentum region (see Fig. 2.10).

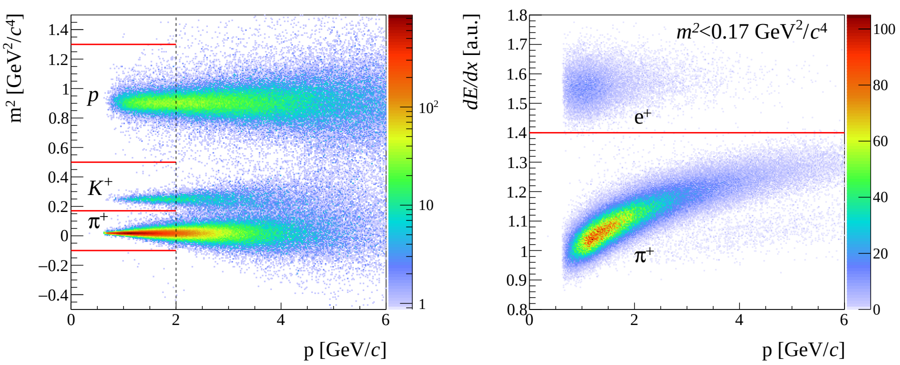

Figure 5.10: *Left*: The distribution of m^2 as a function of momentum for positive particles at 19A GeV/c beam momentum. Dashed line shows applicability limit of the *tof* identification. Red vertical lines present cut values separating different particle species. *Right*: Distribution of dE/dx as a function of momentum for positive particles produced at 19A GeV/c beam momentum. The distribution is limited to particles with m^2<0.17 GeV$^2/c^4$, allowing direct separation of pions and (anti)electrons. Red line denotes the cut value.

For compatibility with the rest of the identification procedure, each particle is assigned with a set of three probabilities in the following way:

$$P_{j=\{p,\pi,K\}}(m^2) = \begin{cases} 1 & \text{if } m^2 \in I_j \\ 0 & \text{otherwise} \end{cases} \tag{5.4}$$

Specific intervals I_j in the formula above are defined with Eq. 5.3.

High momentum particles

For identification of particles with $p>2$ GeV/c, the *full tof* – dE/dx method was employed. An example distribution of particles in the m^2–dE/dx plane for selected Ar+Sc interactions at 30A GeV/c is presented in Fig. 5.11. Simultaneous utilization of *tof* and dE/dx measurements provides excellent separation of different particle species, thus allowing efficient particle identification.

Particle identification is performed in $p - p_\mathrm{T}$ phase space, for positively and negatively charged particles separately. The $p - p_\mathrm{T}$ phase space is subdivided into rectangular, linear bins of 1 GeV/c in total momentum and 0.1 GeV/c in transverse momentum. The m^2 – dE/dx distribution in each phase space bin, containing at least 500 particles, is independently fitted with two-dimensional function presented below:

$$\begin{aligned} \rho(x,y) &= \sum_{j=p,\pi,K,e} \rho_j(x,y) \\ &= \sum_j \frac{N_j}{2\pi\,\sigma_x} e^{-\frac{(x-x_j)^2}{2\sigma_x^2}} \left(\frac{f}{\sigma_{y_1}} e^{\frac{(y-y_j)^2}{2\sigma_{y_1}^2}} + \frac{(1-f)}{\sigma_{y_2}} e^{\frac{(y-y_j)^2}{2\sigma_{y_2}^2}} \right), \end{aligned} \tag{5.5}$$

where N_j and f are amplitudes and weighting parameter, respectively, x_j and σ_x are mean and width of the dE/dx Gaussian, and y_j, σ_{y_1} , σ_{y_2} are mean and widths of the two m^2 Gaussians. For simplicity of notation, dE/dx is denoted by x and m^2 by y. The function 5.5 is a linear combination of single-particle contributions corresponding to p, π, K and e. A product of a single Gaussian in dE/dx and weighted sum of two Gaussians centered around the

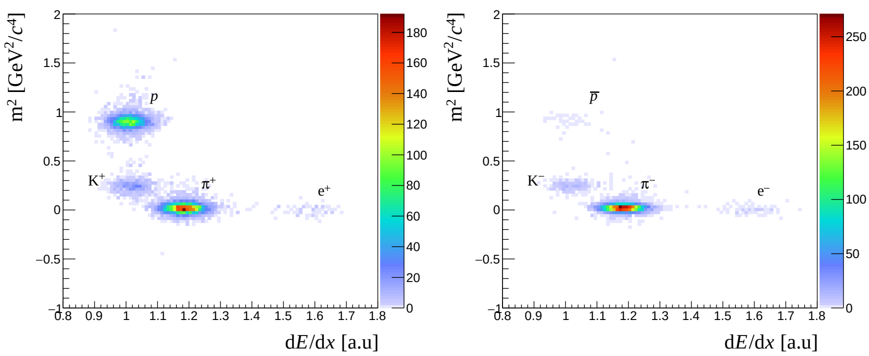

Figure 5.11: Example distributions of m^2 versus dE/dx in a single phase space bin (2 GeV/c < p < 3 GeV/c, 0.5 GeV/c < p_T < 0.6 GeV/c) for positively (*left*) and negatively (*right*) charged particles measured in Ar+Sc collisions at 30A GeV.

same value in m^2 was chosen as a single particle distribution. The double Gaussian structure of the m^2 part of the distribution was chosen to properly describe long tails of the m^2 distribution. In this scope, σ_{y_1} describes width of the central part of the distribution, while σ_{y_2} is responsible for the tails, implying $\sigma_{y_2} > \sigma_{y_1}$. An example $tof - \mathrm{d}E/\mathrm{d}x$ fit performed in a single phase space bin for Ar+Sc at 30*A* GeV/*c* is presented on Fig. 5.12.

Fits were performed in the total momentum range 2-10 GeV/*c* and transverse momentum range 0-2 GeV/*c*. The upper limit on the total momentum of particles accepted for the analysis comes from the fact, that m^2 distributions become wide for large momenta, impeding particle identification. The fit result allows calculation of the probability P_i, that a measured particle is of a given type $i = p, \pi, K$ in the following way:

$$P_i(p, p_\mathrm{T}, \mathrm{d}E/\mathrm{d}x, m^2) = \frac{\rho_i^{p,p_\mathrm{T}}(m^2, \mathrm{d}E/\mathrm{d}x)}{\rho^{p,p_\mathrm{T}}(m^2, \mathrm{d}E/\mathrm{d}x)} \tag{5.6}$$

Here, as well as in the previous section, electrons are omitted, as their identification is not of interest for the purpose of this thesis. Note that in formula 5.6 the electron term is is still present in the denominator (ρ is the full fitted function, Eq. 5.5).

For illustration, probabilities of hadron species for positively and negatively charged particles produced in Ar+Sc collisions at 19*A* and 150*A* GeV/*c* are presented in Fig. 5.13. In the case of perfect particle identification, the probability distribution would be binary, i.e., it will have entries at 0 and

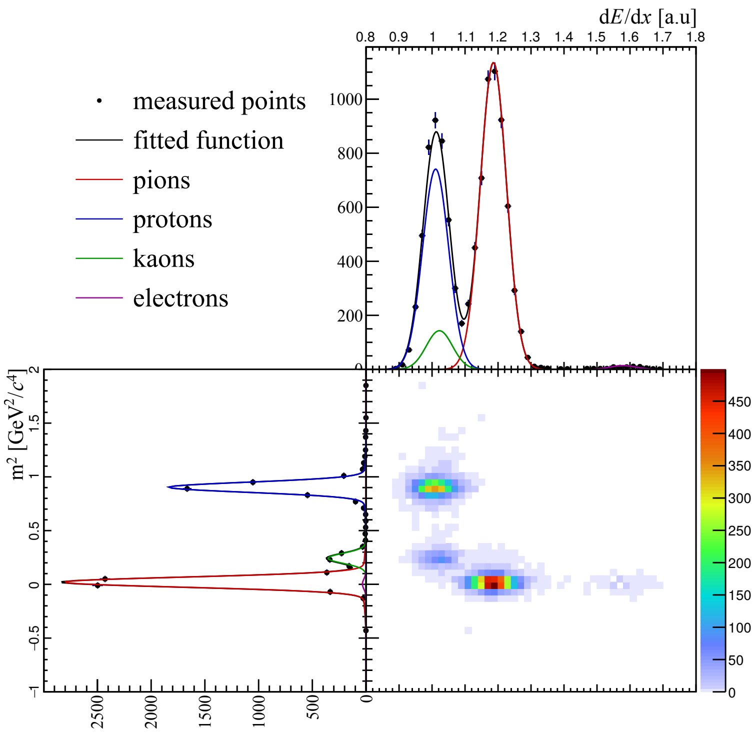

Figure 5.12: An example distribution of m^2 versus $\mathrm{d}E/\mathrm{d}x$ in a single phase space bin (2 GeV/*c* $< p <$ 3 GeV/*c*, 0.5 GeV/*c* $< p_\mathrm{T} <$ 0.6 GeV/*c*) with fitted $tof - \mathrm{d}E/\mathrm{d}x$ function for positively charged particles measured in Ar+Sc collisions at 30*A* GeV.

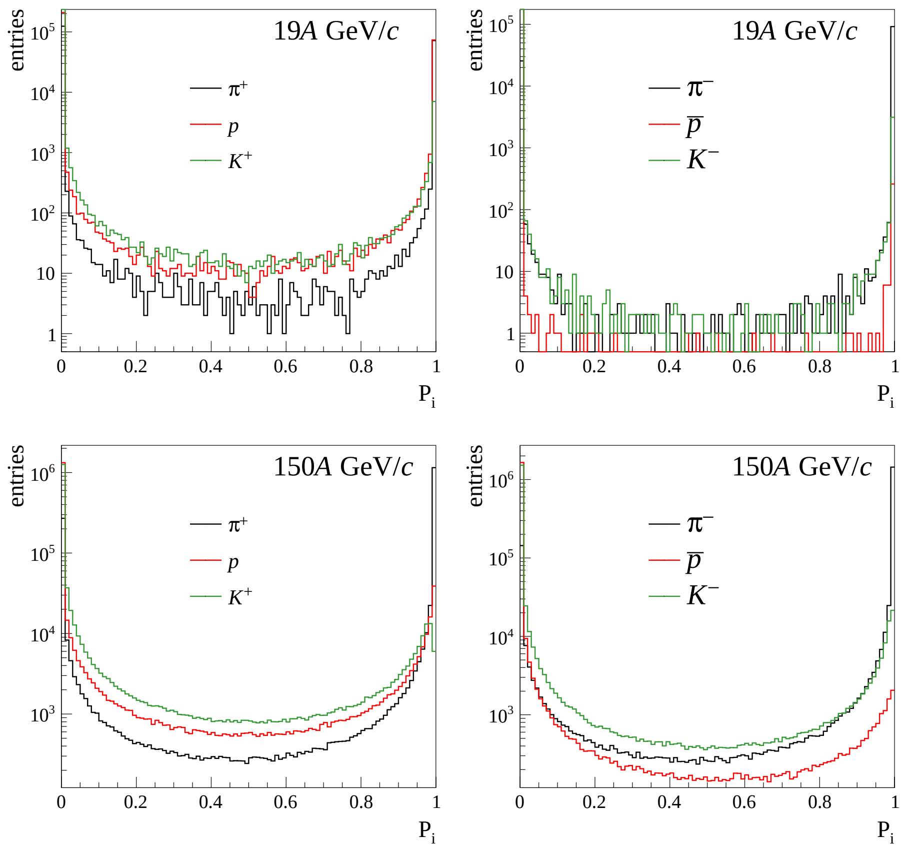

Figure 5.13: Probability of a track being a pion, kaon or proton for positively (*left*) and negatively (*right*) charged particles in Ar+Sc collisions at 19*A* (*top*) and 150*A* GeV/*c* (*bottom*).

1 only. This is the case for the low momentum variant of the $tof - dE/dx$ method described in the previous section. However, the probability can be of any value from $[0,1]$ interval for the full variant of the $tof - dE/dx$ method. Thus the intermediate parts of the distributions in Fig. 5.13 are populated.

5.4.2 Identity method

Particle identification is performed in $p - p_T$ phase space, as it offers common kinematic acceptance defined by the detector geometry for different kinds of particles. In order to transform identified particles from momentum - transverse momentum to rapidity - transverse momentum phase space, the so-called identity method [74] is employed. Multiplicities of different particle types ($i = p, \pi, K$) in $y - p_T$ space are calculated as follows:

$$n_i^{raw}(y, p_T) = \sum_{j=1}^{N_{trk}} P_i(p, p_T), \tag{5.7}$$

where P_i is the probability of the track being the particle type i given by Eqs. 5.4 and 5.6 calculated in $p - p_T$ space. The summation runs over all selected particles in a given $y - p_T$ bin, N_{trk} denotes number of particles in the said bin. The identity method allows allows changing of variables describing physical quantities with particle identification based on probabilities (P_i can take any value from [0,1] interval). The transformation relations between the two sets of variables are often non-trivial, as in the case of $(p, p_T) \rightarrow (y, p_T)$ transformation discussed here.

5.5 Corrections

Raw particle production multiplicities obtained in the previous section (Eq. 5.7) suffer from distortions caused by various effects. The biasing effects include detector acceptance and efficiency, reconstruction procedure efficiency, the contribution of particles from weak decays of unstable particles. A method based on the MC simulations enabling correction of the mentioned effects was developed and will be described in this section.

The correction factors are computed and applied to raw multiplicities bin-by-bin in $y - p_T$ space for all particle types i ($i \in \{p, \bar{p}, \pi^{\pm}, K^{\pm}\}$) individually. Partial contributions to the correction factors coming from the following effects are also studied:

1. Detector geometry
2. Inefficient ToF pixels
3. ToF pixel efficiency
4. Weak decays of charged hadrons

Contributions listed above are computed in $p - p_T$ space, unlike the total correction factors. The momentum space was chosen for this study because it offers common kinematic acceptance for different particle types defined by the ToF geometry.

Detector geometry

The first correction concerns the geometrical acceptance of the detector and efficiency of the reconstruction procedure. It also includes effects of biasing event and track selection criteria described in sections 5.2 and 5.3. It is defined as follows:

$$\varepsilon_i^{geo} = \frac{(n_i)^{geo}_{MCrec}}{(n_i)_{MCgen}}, \tag{5.8}$$

where $(n_i)^{geo}_{MCrec}$ is the multiplicity of reconstructed particles of type i passing all the selection criteria, while $(n_i)_{MCgen}$ stands for the multiplicity of the same kind of particles generated by the EPOS model, including only primary particles. Thus, the results at this stage are corrected for contamination by products of weak decays. Both multiplicities correspond to the same centrality interval (10% of the most central Ar+Sc events). The selection criteria imposed on the MC sample require that the last point measured on the reconstructed track is in the most downstream part of MTPC-L/R. This criterion implies that this correction factor also includes contributions from particles that did not reach the back face of the MTPC due to interaction with the detector material or a weak decay. An example ε_i^{geo} corrections obtained for Ar+Sc interactions at 75A GeV/c are presented in

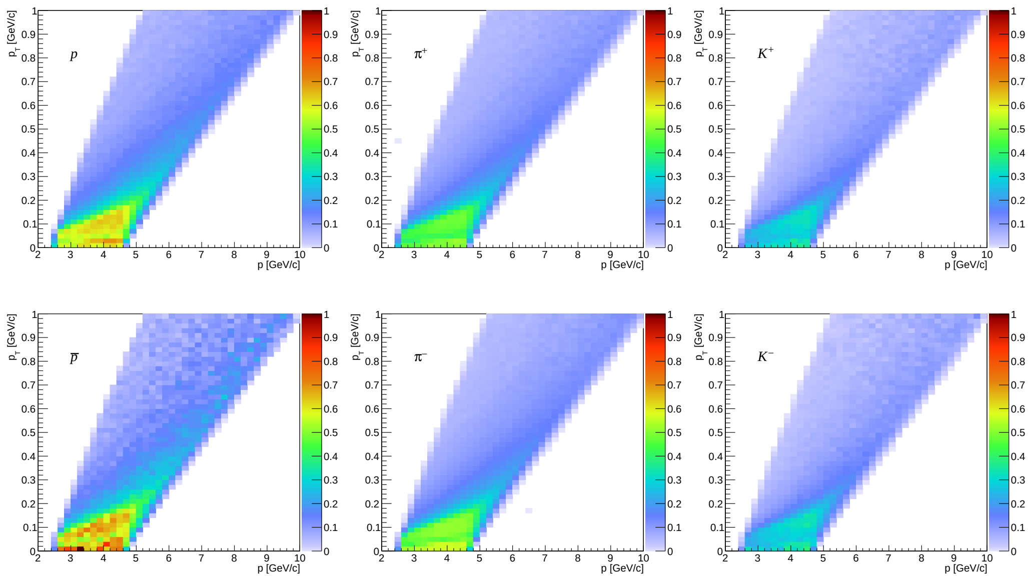

Figure 5.14: MC correction factors for geometrical acceptance of the ToF detectors and decays before the two last padrows of of MTPC for Ar+Sc collisions at 75*A* GeV/*c*.

Fig. 5.14. The visible quantitative differences in the values of the correction factors originate mostly from the weak decays of $K^{\pm}$ and $\pi^{\pm}$ with different lifetimes.

ToF detector efficiency

The next two partial corrections concern the efficiency of the ToF detector. The ToF efficiency is obtained from the experimental data, as described in section 5.3. Contribution of the inefficient ($\epsilon_k < 50\%$, see Sec. 5.3 for details) ToF pixels is calculated as the ratio of the multiplicity of simulated tracks extrapolated to properly working pixels $(n_i)^{dead}_{MCrec}$ and the multiplicity of tracks extrapolated to any ToF pixel - $(n_i)^{geo}_{MCrec}$:

$$\varepsilon_i^{dead} = \frac{(n_i)^{dead}_{MCrec}}{(n_i)^{geo}_{MCgen}} \tag{5.9}$$

Values of this partial contribution obtained for Ar+Sc at 75*A* GeV/*c* are presented in Fig. 5.15. The ε_i^{dead} correction depends only on spatial distribution of inefficient pixels in the ToF wall. Thus its values are the same for particles with the same charge signs.

To simulate the efficiency of the *working* ToF pixels, each track that was extrapolated to the efficient ToF pixel is weighted with the efficiency ϵ of the given pixel (Eq. 5.2). This procedure results in the weighted multiplicity of particles hitting *working* Tof pixels - $(n_i)^{eff}_{MCrec}$. The corresponding correction factor is expressed with the following formula:

$$\varepsilon_i^{eff} = \frac{(n_i)^{eff}_{MCrec}}{(n_i)^{dead}_{MCgen}} \tag{5.10}$$

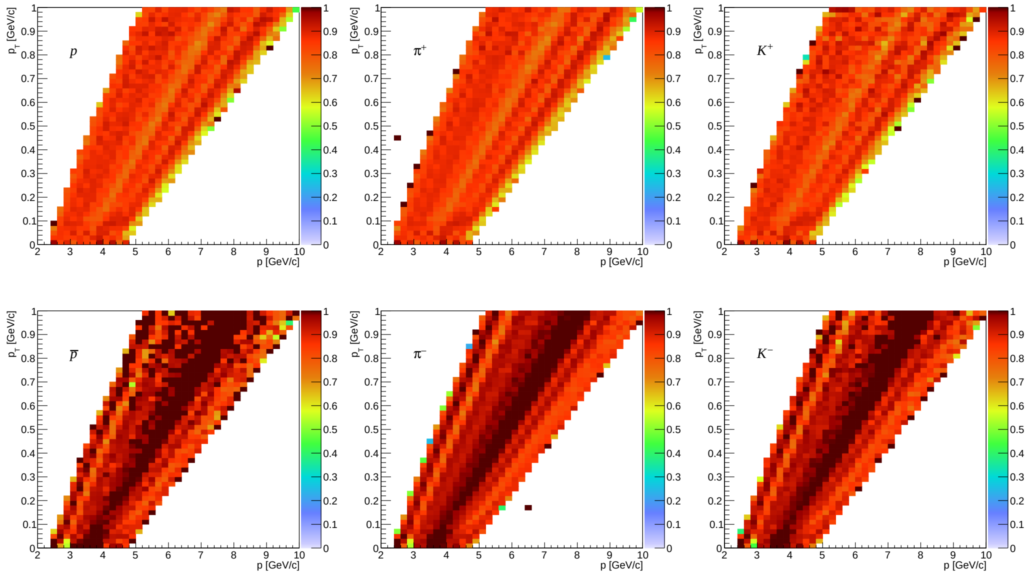

Figure 5.15: MC correction factors for inefficient (<50%) ToF pixels for Ar+Sc collisions at 75A GeV/c.

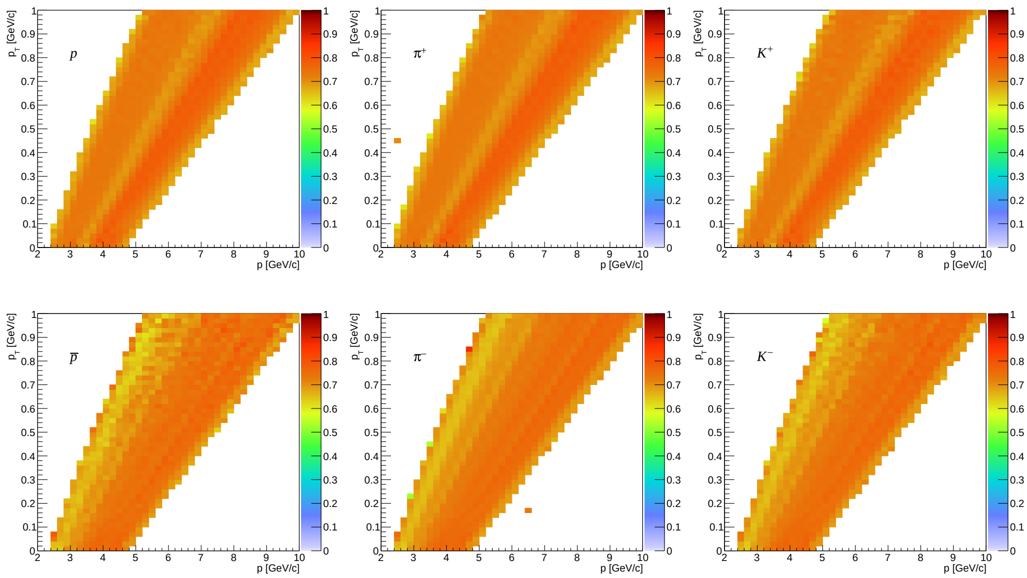

Figure 5.16: MC correction factors for ToF pixel efficiency for Ar+Sc collisions at 75A GeV/c.

Example values of the pixel efficiency correction factors are shown in Fig. 5.16.

Weak decays

The last partial correction describes the influence of particles that weakly decayed or interacted with the detector material between the last point measured on the track in MTPCs and the ToF detector. Tracks of such particles will be successfully extrapolated to the ToF detector. Simulated decays and interactions allow obtaining the multiplicity of particles of a given type that reach the ToF pixels and are weighted with their respective efficiencies - $(n_i)^{decay}_{MCrec}$. The value of this correction factor is given, as for the previous ones, in form of the ratio:

$$\varepsilon_i^{decay} = \frac{(n_i)^{decay}_{MCrec}}{(n_i)^{eff}_{MCgen}} \tag{5.11}$$

This contributions can be seen in Fig. 5.17. Again, quantitative differences between π and K come from their different lifetimes for weak decays.

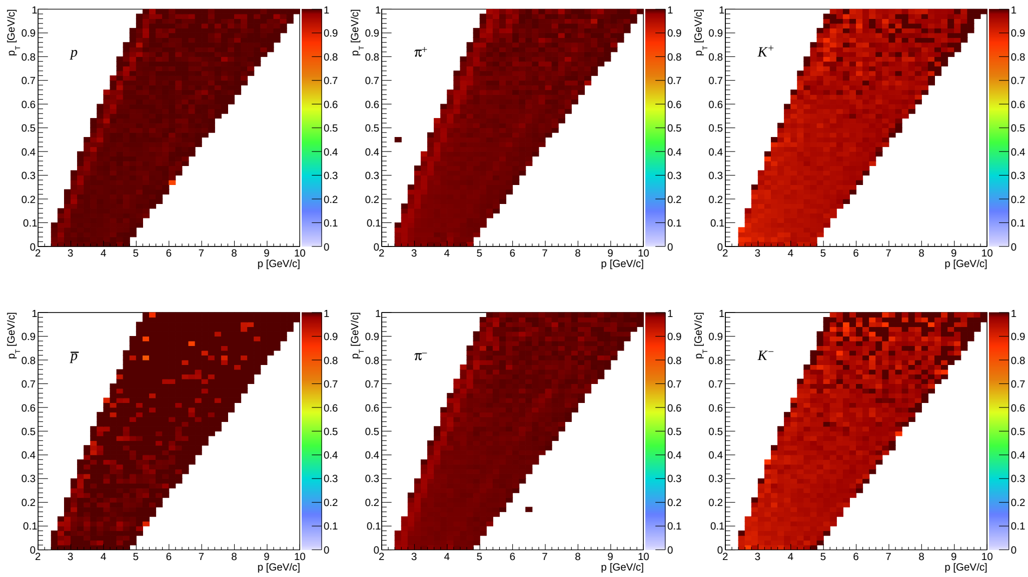

Figure 5.17: MC correction factors decays and interactions with the detector material between the last point measured in MTPC and the ToF walls for Ar+Sc collisions at 75*A* GeV/*c*.

Total correction and final spectra

The total correction is given by the product of partial corrections defined with Eqs. 5.8, 5.9, 5.10 and 5.11:

$$\varepsilon_i = \varepsilon_i^{geo} \cdot \varepsilon_i^{dead} \cdot \varepsilon_i^{eff} \cdot \varepsilon_i^{decay} = \frac{(n_i)_{MCrec}}{(n_i)_{MCgen}} \tag{5.12}$$

$(n_i)_{MCrec}$ is equal to $(n_i)^{decay}_{MCrec}$ truncated to the kinematic region in which the identification of particles was possible ($p - p_T$ bins with at least 500 entries and at least 30% coverage with geometrical acceptance, see Sec. 5.4). Application of the same acceptance to the simulated data provides that resulting reconstructed MC directly corresponds to the reconstructed experimental data. The total correction factors ε_i are calculated in $y - p_T$ phase space. Examples of generated MC, reconstructed MC and the resulting correction factors calculated for Ar+Sc interactions at 75*A* GeV/*c* are presented in Fig. 5.18.

Final, double differential particle production spectra in y and p_T are obtained by normalisation of the raw multiplicities (Eq. 5.7) to the number

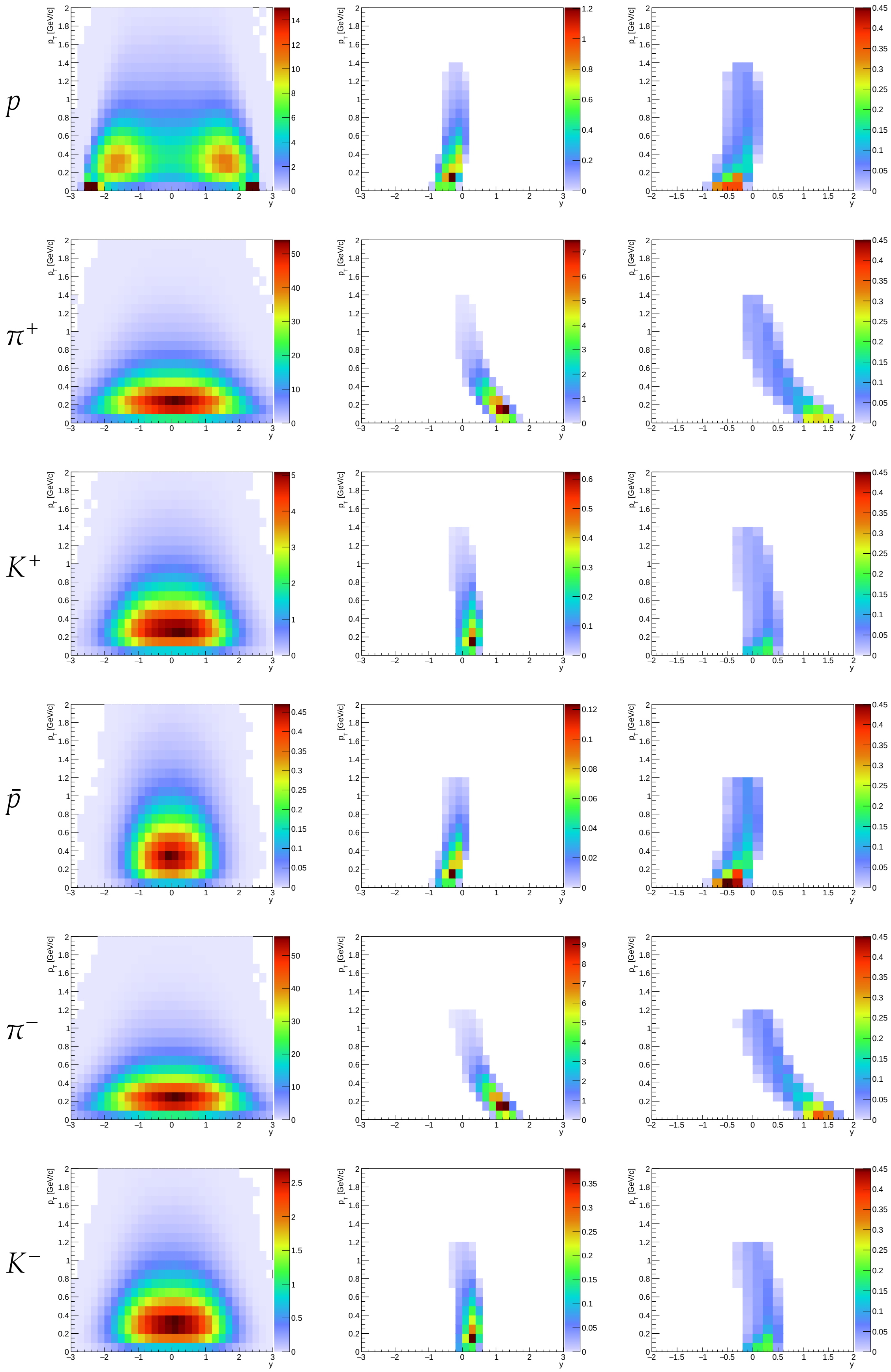

Figure 5.18: An example of generated MC (*left column*), reconstructed MC after application of the selection criteria (*middle column*) and the resulting correction factors (*right column*) for Ar+Sc at 75*A* GeV simulation.

of events used in the analysis (N_{ev}) and size of the $y - p_{\mathrm{T}}$ bin ($\Delta y \cdot \Delta p_{\mathrm{T}}$), followed by multiplicative application of the correction factor (Eq. 5.12):

$$\frac{\mathrm{d}^2 n_i}{\mathrm{d}y\mathrm{d}p_{\mathrm{T}}} = \frac{1}{N_{\mathrm{ev}} \cdot \Delta y \cdot \Delta p_{\mathrm{T}}} \cdot n_i^{raw} \cdot \frac{1}{\varepsilon_i} \tag{5.13}$$

5.6 Uncertainties

5.6.1 Statistical uncertainties

Final particle production spectra in Ar+Sc collisions are obtained with finite statistics of experimental data and simulated events. The corresponding statistical uncertainties will be discussed in this section.

The uncertainty calculation of raw multiplicities is performed in a bin-by-bin manner under the assumption of Poissonian statistics in a single bin and no correlation between the bins. The resulting statistical error is therefore given by the following formula:

$$\sigma_{(n_i)^{raw}} = \sqrt{\sum_{j=0}^{N_{\mathrm{trk}}} P_i^2}, \tag{5.14}$$

where $\sigma_{(n_i)^{raw}}$ is the statistical uncertainty of the raw particle multiplicity for particle of type i (given by Eq. 5.7) and N_{trk} is the number of tracks in a given bin.

Similarly to the raw production spectra, the uncertainties of the MC corrections were obtained for all bins independently and assumed to be uncorrelated. Here, the reconstructed MC is a subset of the generated MC, and thus has a binomial distribution. The statistical uncertainties of the correction factors were calculated as follows:

$$\sigma_{\varepsilon_i} = \varepsilon_i \sqrt{\frac{(n_i)_{MCgen} - (n_i)_{MCrec}}{(n_i)_{MCgen} \cdot (n_i)_{MCrec}}} \tag{5.15}$$

The final uncertainty of the double-differential corrected particle production spectrum (Eq. 5.13) takes the following form:

$$\sigma_{\mathrm{stat}}^2 = \frac{1}{\left(N_{\mathrm{ev}} \cdot \Delta y \cdot \Delta p_{\mathrm{T}}\right)^2} \left[\left(\frac{\sigma_{(n)^{raw}}}{\varepsilon} \right)^2 + \left(\frac{\sigma_{\varepsilon} \cdot (n)^{raw}}{\varepsilon^2} \right)^2 \right], \tag{5.16}$$

where $\sigma_{(n)^{raw}}$ is the uncertainty of the uncorrected multiplicity $(n)^{raw}$ (Eqs. 5.7 and 5.14), σ_{ε} denotes the uncertainty of the correction factor ε (Eqs. 5.12 and 5.15), and N_{ev} is the total number of accepted events. The index i denoting the particle type was skipped for the notation clarity. The uncertainty is calculated for all particle types independently. Example distributions of the relative statistical uncertainties for different particle species produced in Ar+Sc collisions at $75A\,\mathrm{GeV}/c$ are presented in Fig. 5.19.

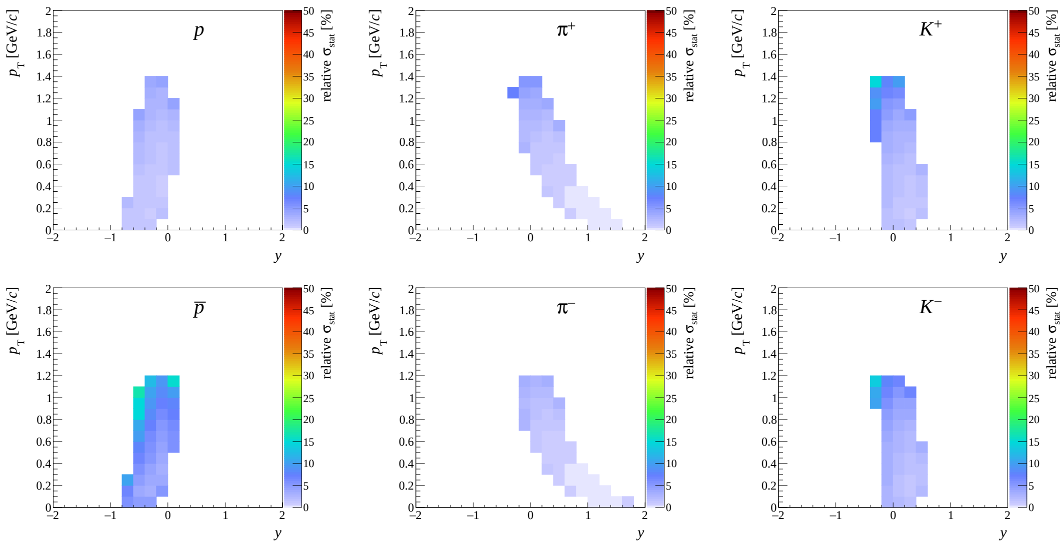

Figure 5.19: An example of the statistical uncertainty calculated for charged hadrons produced in Ar+Sc collisions at 75*A* GeV/*c*.

5.6.2 Systematic uncertainties

The choice of selection criteria in event and track selection and the analysis procedure itself may cause a systematic bias of the final results. A procedure allowing estimation of the possible systematic biases was developed and applied. The values of all biasing factors are independently varied in the procedure, and the whole analysis is repeated (event and track selection, particle identification, MC correction calculation, and application). The resulting particle spectra are compared with the *nominal* ones, and the most considerable difference between the two is assigned as a systematic uncertainty connected with a given biasing factor. The uncertainties are estimated bin-by-bin in $y - p_T$ space for all particle kinds separately.

In this analysis, contributions from the following biasing factors to the systematic uncertainties were considered:

(i) Event and track selection criteria - σ_i

(ii) ToF detector performance - σ_{ii}

(iii) particle identification - σ_{iii}

The criteria were varied between the *loose* (less restrictive than *nominal*) and *tight* (more restrictive than *nominal*) values. Values of particular selection parameters employed in the systematic uncertainty estimation are summarised in table 5.3.

Event and track selection criteria

Values of biasing event and track selection criteria were varied in a broad range allowing estimation of the systematic uncertainty. The impact of the following factors was studied:

- Allowed *z*-position range of the reconstructed interaction vertex was varied between ±5 cm and ±15 cm with respect to the center of the target position,

- Number of required reconstructed points in the magnetic field (VTPC clusters) was changed by ±5 with respect to its nominal value,
- Restriction of impact point $\vec{b}$ components was adjusted in the range 2-6 cm for the x component and 1-4 cm for the y component,
- The distance between the reconstructed track and last measured point $|\vec{d}|$ was varied in the range 3-8 cm.

ToF detector performance

For the selection criteria influencing efficiency of the ToF detector, parameters listed below were taken into account:

- Range of accepted normalized QDC values, as in table 5.3,
- Threshold for determination of non-working ToF pixels was changed as in table 5.3.

Here, the two biasing factors listed above are correlated, so to determine their joint contribution to the systematic uncertainty, they are varied simultaneously within mentioned limits. The maximal deviation between the resulting spectrum and the *nominal* one is assigned to the contribution coming from ToF detector performance.

Identification procedure

Possible bias from the identification procedure was also estimated. For the low momentum $tof - \mathrm{d}E/\mathrm{d}x$ identification, the separation of different particle species with m^2 cut is unequivocal (distributions corresponding to different particles in the left panel of the Fig. 5.10 do not overlap). Hence, the systematic uncertainty of this identification method was estimated to be negligible. For the high momentum variant of the identification method, all fitted mean values of the two-dimensional Gaussians (x_i and y_i, see Eq. 5.5) were changed by ±1%.

Selection criteria	Cut values		
	tight	*nominal*	*loose*
interaction vertex z	(-580 ± 5) cm	(-580 ± 10) cm	(-580 ± 15) cm
impact point x	$\|b_x\|$ <2 cm	$\|b_x\|$ <4 cm	$\|b_x\|$ <6 cm
impact point y	$\|b_y\|$ <1 cm	$\|b_y\|$ <2 cm	$\|b_y\|$ <3 cm
last clus. dist. $\vec{d}$	$\|\vec{d}\|$ <3 cm	$\|\vec{d}\|$ <4 cm	$\|\vec{d}\|$ <8 cm
min. num. of VTPC clusters	20	15	10
ToF norm. QDC	[0.8,1.5]	[0.5,2.0]	[0.3,3.0]
ineff. ToF pixel threshold	60%	50%	40%

Table 5.3: The summary of the cut parameter values used for the estimation of the systematic uncertainties.

The contributions listed above were added in quadrature, resulting in total systematic uncertainty:

$$\sigma_{\text{sys}} = \sqrt{\sigma_i^2 + \sigma_{ii}^2 + \sigma_{iii}^2} \tag{5.17}$$

The overall uncertainties (both statistical and systematic) along with partial contributions for charged kaons at two different beam momenta as a function of the transverse momentum in mid-rapidity are shown in Fig. 5.20. Example distributions of the estimated relative systematic uncertainties for different particle species produced in Ar+Sc collisions at 75*A* GeV/*c* are presented in Fig. 5.21.

5.7 Alternative analysis methods

Determination of the spectra of charged particles produced in the interactions studied by the NA61/SHINE experiment is performed with three main analysis methods. In the case of the Ar+Sc data set, the analyses described in this section are performed independently by different members

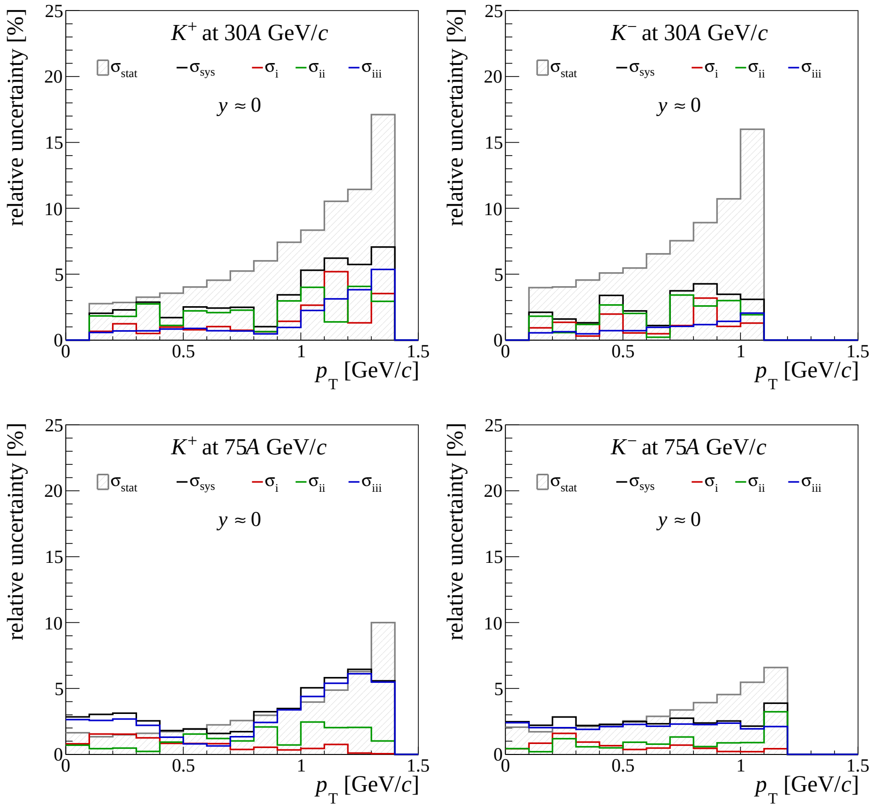

Figure 5.20: Relative contributions to systematic uncertainty (σ_{sys}) including partial contributions from: event and track selection criteria (σ_i), identification procedure (σ_{ii}), and ToF detector performance (σ_{iii}) for positively (*left*) and negatively (*right*) charged kaons in mid-rapidity produced in Ar+Sc collisions at 30*A* (*top*) and 75*A* GeV (*bottom*). Statistical uncertainty (σ_{stat}) is also presented for reference with shaded area.

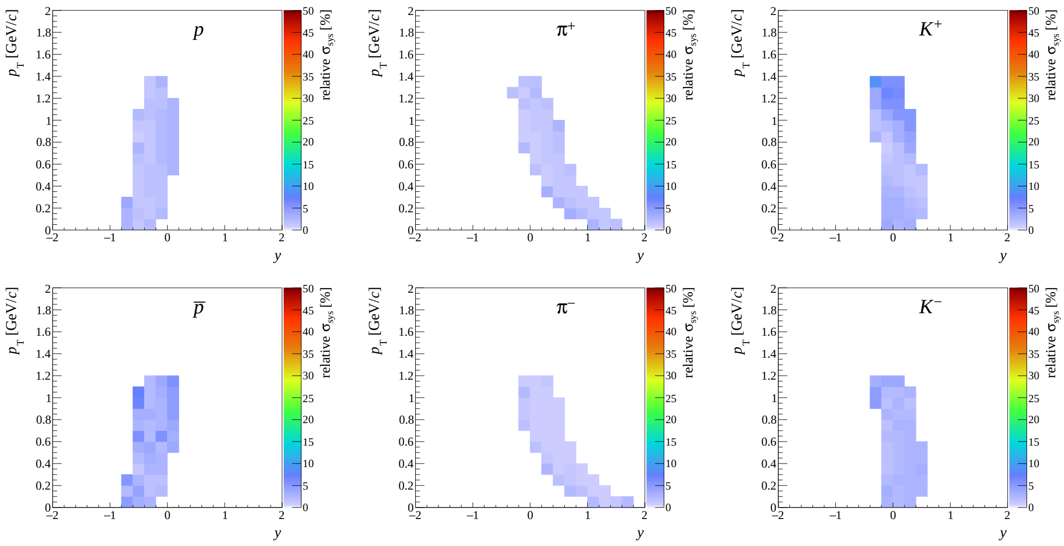

Figure 5.21: An example of the total systematic uncertainty estimation for charged hadrons produced in Ar+Sc collisions at 75*A* GeV/*c*.

of the NA61/SHINE collaboration. The *tof* − d*E*/d*x* analysis method described and employed in this thesis is supplemented with the two analyses described below.

The first method, called the h^- method, is based on the fact that the vast majority of the produced negatively charged hadrons are negative pions in the SPS energy range. The contribution of the other negative particles (anti-protons, kaons, and heavier ones), is removed with model-based MC-derived correction factors. The h^- method acceptance covers the whole forward hemisphere, and for some energies extends to the backward-rapidity region. The results on π^- multiplicity in Ar+Sc collisions were recently published in Ref. [70].

The second analysis, d*E*/d*x* analysis, is based solely on energy loss measurements in the TPCs. Particle identification is based on one-dimensional, TPC-measured energy loss distributions in phase space bins, similarly to the *tof* − d*E*/d*x* method. The applicability of this method is limited to particles with p >5 GeV/*c* due to crossing Bethe-Bloch curves in the low momentum region (see Sec. 2.4.3). The results of the d*E*/d*x* method were presented in Ref. [75].

Figure 5.22 presents a comparison of acceptances of the three mentioned analysis methods for Ar+Sc collisions at 40*A* GeV/*c*. Combined acceptance of all methods employed in NA61/SHINE provides broad coverage of the forward rapidity hemisphere. Moreover, non-empty overlaps between acceptances of the analyses allow direct comparison of the obtained results, already on the level of the $y - p_T$ spectra.

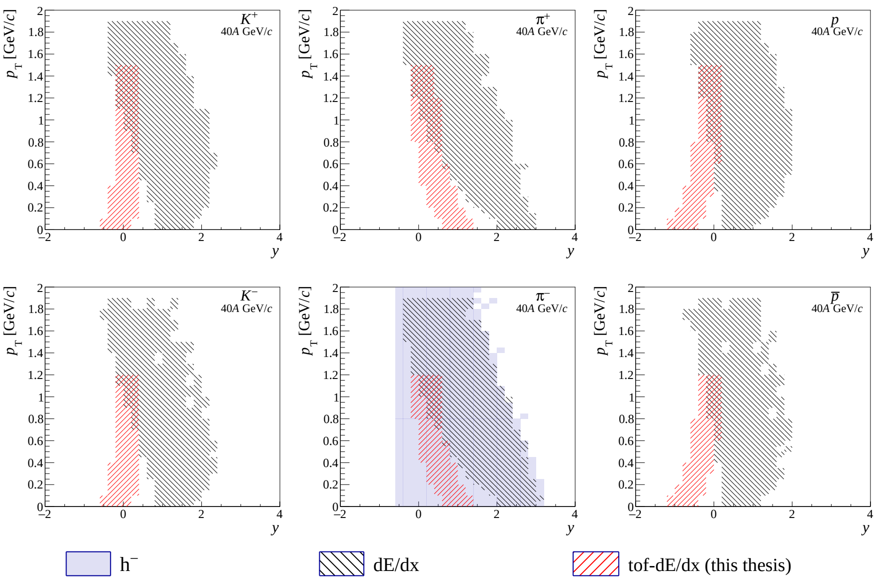

Figure 5.22: Comparison of acceptances of three different analysis methods employed in the NA61/SHINE at 40*A* GeV/*c* beam momentum for positively (*top*) and negatively (*bottom*) charged particles. Acceptances are presented for kaons (*left*), pions (*middle*), and protons (*right*).

Chapter 6

Results

This chapter contains experimental results on inclusive charged hadron production spectra in central Ar+Sc collisions in the SPS energy range. The results are presented as double-differential spectra in rapidity-transverse momentum space (Sec. 6.1), as well as one-dimensional p_T spectra in rapidity slices (Sec. 6.2). Spectra in rapidity slices are compared with the results of h^- [70] and dE/dx analyses [75]. Next, mid-rapidity spectra of kaons and protons are presented (Sec. 6.3). The properties of kaon production in mid-rapidity are then studied in the scope of the onset of deconfinement (Sec. 6.4). Subsequently, system size dependence of the important properties of strangeness production in mid-rapidity is shown (Sec. 6.5). Finally, a comparison of the obtained results with calculations based on the theoretical models is provided (Sec. 6.6).

6.1 Double differential spectra of charged hadrons

The double differential particle production spectra $\frac{\mathrm{d}^2 n}{\mathrm{d}y\mathrm{d}p_\mathrm{T}}$ of K^+, K^-, π^+, ,π^-, p and $\bar{p}$ were calculated as a function of rapidity and transverse momentum for six beam momenta: 13A, 19A, 30A, 40A, 75A, and 150A GeV/c. Obtaining the $\bar{p}$ spectra for 13A and 19A GeV/c was not possible due to limited statistics and the low $\bar{p}$ production yield. The value of the spectrum in a particular phase space bin corresponds to the multiplicity of a given particle produced in strong and electromagnetic processes in a single event per unit of $y - p_\mathrm{T}$ space in this bin.

The results for all beam momenta are presented in figures 6.1 - 6.6. They are grouped by the particle kind in the following way:

- Fig. 6.1 - positively charged kaons,
- Fig. 6.2 - negatively charged kaons,
- Fig. 6.3 - positively charged pions,
- Fig. 6.4 - negatively charged pions,
- Fig. 6.5 - protons,
- Fig. 6.6 - anti-protons.

The numerical values of the double differential spectra, together with statistical and systematic uncertainties, are tabulated and presented in Appendix C.

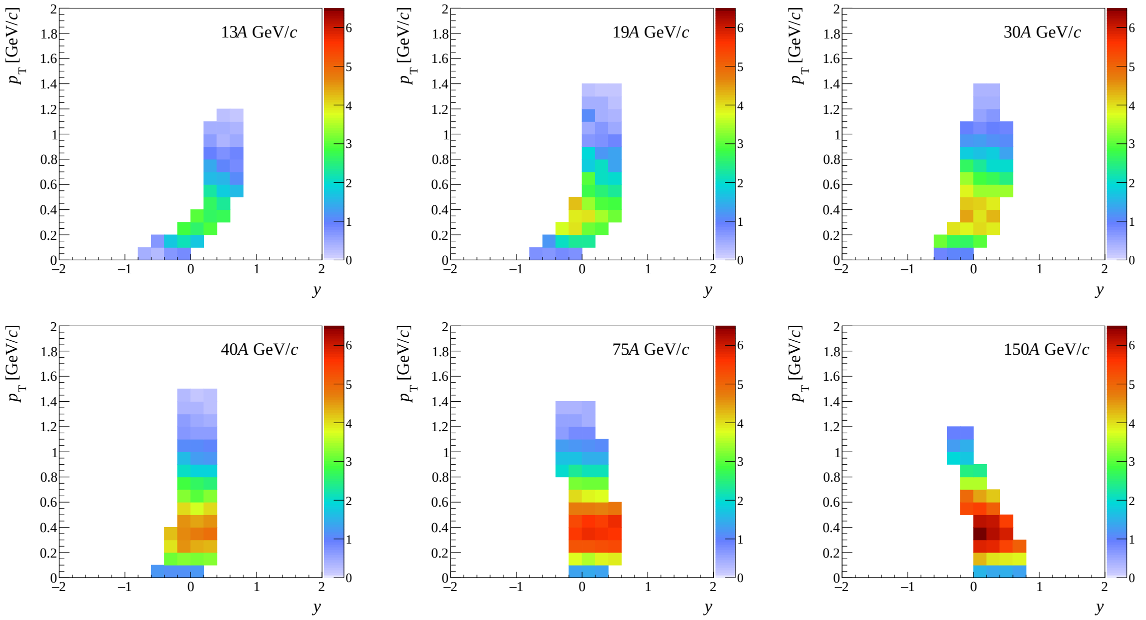

Figure 6.1: The double differential spectra of positively charged kaons produced in central Ar+Sc collisions at 13*A*, 19*A*, 30*A*, 40*A*, 75*A*, and 150*A* GeV/*c* beam momenta.

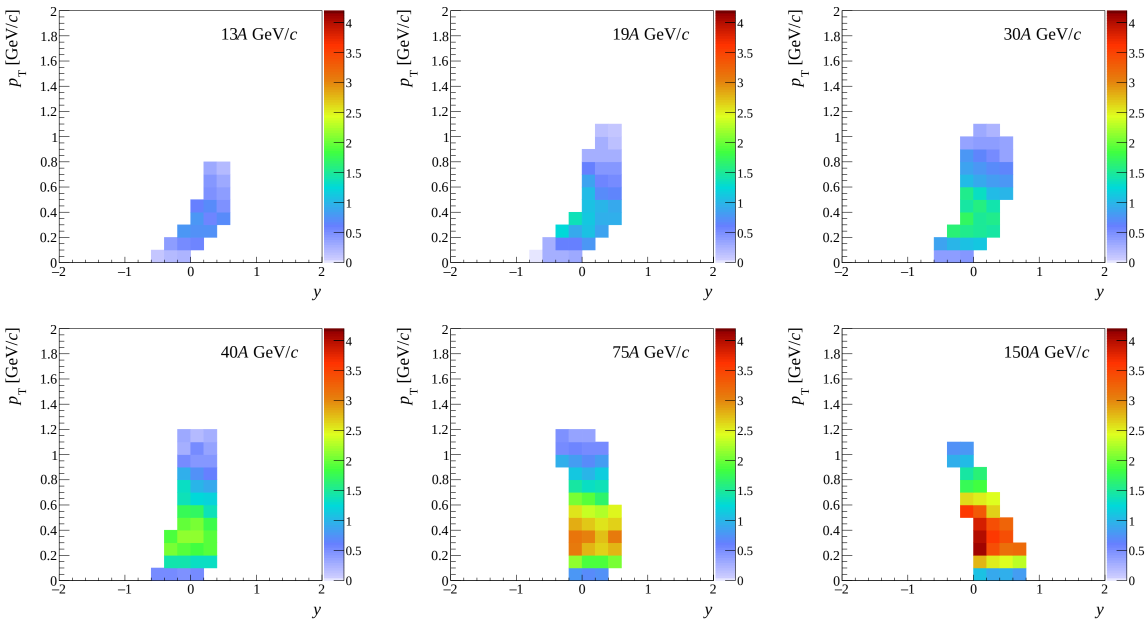

Figure 6.2: The double differential spectra of negatively charged kaons produced in central Ar+Sc collisions at 13*A*, 19*A*, 30*A*, 40*A*, 75*A*, and 150*A* GeV/*c* beam momenta.

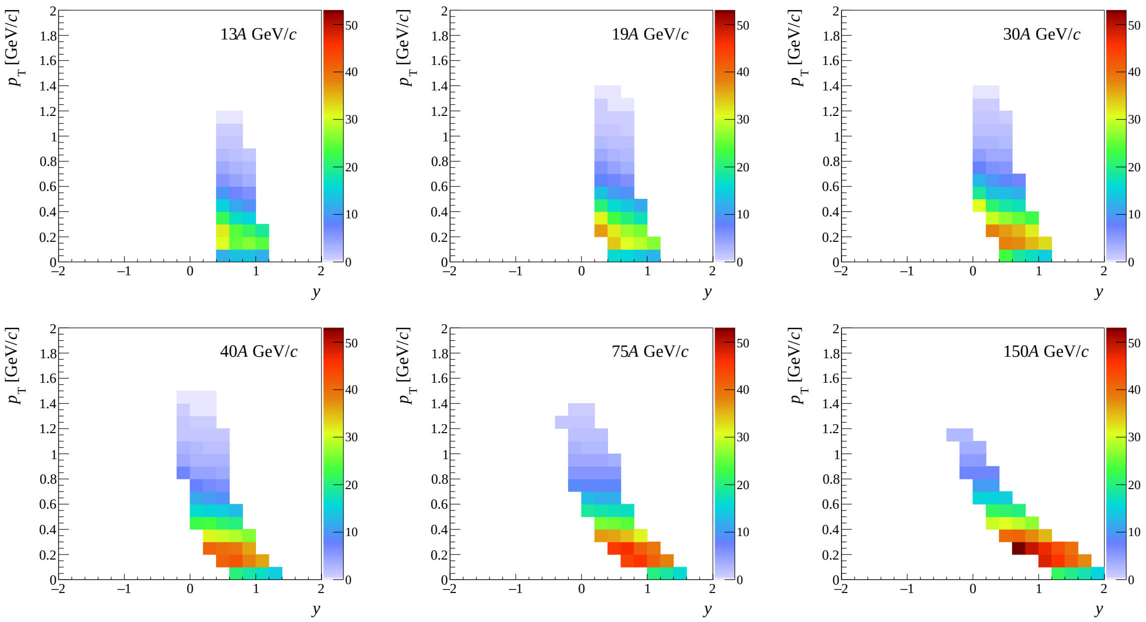

Figure 6.3: The double differential spectra of positively charged pions produced in central Ar+Sc collisions at 13*A*, 19*A*, 30*A*, 40*A*, 75*A*, and 150*A* GeV/*c* beam momenta.

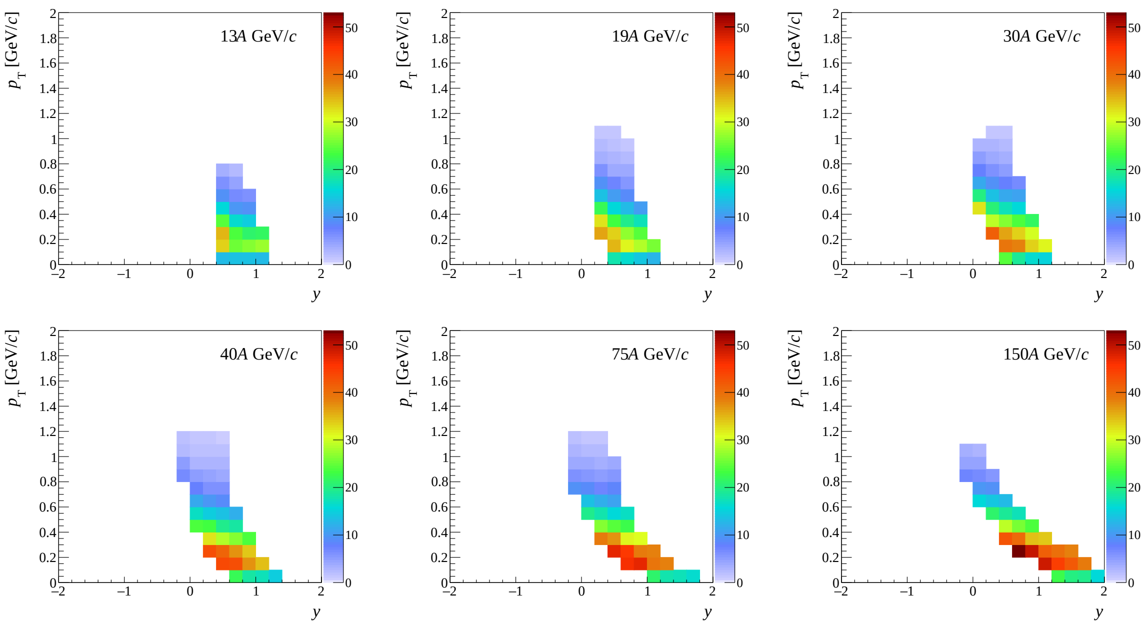

Figure 6.4: The double differential spectra of negatively charged pions produced in central Ar+Sc collisions at 13*A*, 19*A*, 30*A*, 40*A*, 75*A*, and 150*A* GeV/*c* beam momenta.

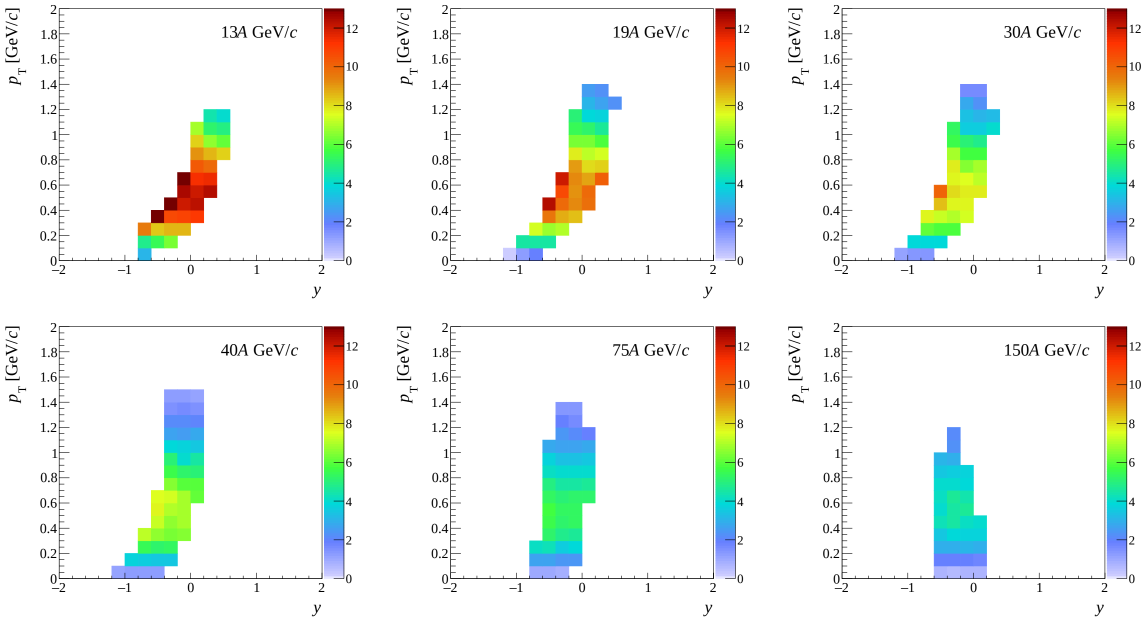

Figure 6.5: The double differential spectra of protons produced in central Ar+Sc collisions at 13*A*, 19*A*, 30*A*, 40*A*, 75*A*, and 150*A* GeV/*c* beam momenta.

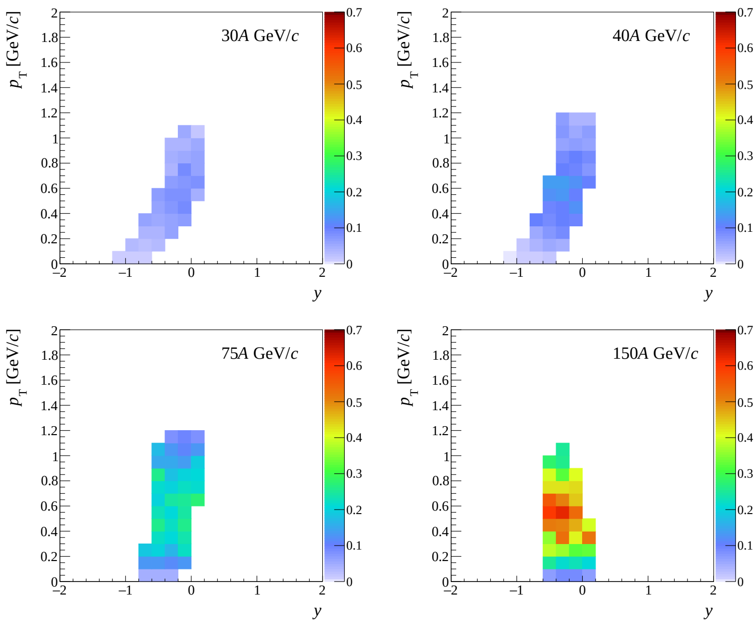

Figure 6.6: The double differential spectra of anti-protons produced in central Ar+Sc collisions at 30*A*, 40*A*, 75*A*, and 150*A* GeV/*c* beam momenta.

6.2 Particle spectra in rapidity slices

The double differential spectra presented in the previous section were also studied as a function of transverse momentum in rapidity slices. The (y, p_T) spectra were projected on the p_T axis for all y bins separately. The results of such projections are presented in Figs. 6.7-6.12. The spectra corresponding to different rapidities are scaled for ease of viewing, and they are plotted with statistical uncertainties (error bars) and systematic uncertainties (shaded bands). Spectra obtained with the $tof-\mathrm{d}E/\mathrm{d}x$ analysis described in this thesis are shown in red.

On the plots presenting spectra of K^+ (Fig. 6.7), K^- (Fig. 6.8), π^+ (Fig. 6.9), p (Fig. 6.11) and $\bar{p}$ (Fig. 6.12) results obtained in the framework of this thesis are presented together with $\mathrm{d}E/\mathrm{d}x$ points from Ref. [75] (see Sec. 5.7), shown in grey. The $\mathrm{d}E/\mathrm{d}x$ spectra were truncated to p_T=1.5 GeV/c to emphasize the low p_T region. Moreover, the $\mathrm{d}E/\mathrm{d}x$ results are plotted only in the rapidity slices for which at least one $tof-\mathrm{d}E/\mathrm{d}x$ point is available. Note that the $tof-\mathrm{d}E/\mathrm{d}x$ method employed in this thesis provides identification of charged kaons in the mid-rapidity region, down to low p_T, for all beam momenta in the SPS energy range not covered by the $\mathrm{d}E/\mathrm{d}x$ method. The results obtained with the two analysis methods agree in the region of overlapping acceptance, although for low beam momenta the overlap between the $tof-\mathrm{d}E/\mathrm{d}x$ and $\mathrm{d}E/\mathrm{d}x$ is small. Non populated bins inside the spectrum for some rapidity slices, prominent for the low beam momenta, correspond to acceptance gaps between the two analysis methods (see Fig. 5.22).

The spectra of negative pions (Fig. 6.10) were compared with the results of the h^- analysis [70]. The results reported in Ref. [70] refer to π^- production in 5% of the most central Ar+Sc collisions. To allow a direct comparison with the results presented in this thesis they were scaled to 10% centrality by means of the mean number of wounded nucleons $\langle W \rangle$:

$$\left(\frac{\mathrm{d}^2 n_{\pi^-}}{\mathrm{d}y\mathrm{d}p_\mathrm{T}}\right)_{10\%} = \left(\frac{\mathrm{d}^2 n_{\pi^-}}{\mathrm{d}y\mathrm{d}p_\mathrm{T}}\right)_{5\%} \cdot \frac{\langle W \rangle_{10\%}}{\langle W \rangle_{5\%}}, \tag{6.1}$$

The values of the mean numbers of wounded nucleons used for scaling were summarised in table 6.1.

p_beam [GeV/c]	13A	19A	30A	40A	75A	150A
$\langle W \rangle_{5\%}$	68.0	68.0	67.9	68.0	68.0	68.1
$\langle W \rangle_{10\%}$	62.2	62.2	62.1	62.2	62.2	62.3
$\langle W \rangle_{10\%}/\langle W \rangle_{5\%}$	0.915	0.915	0.915	0.915	0.915	0.915

Table 6.1: Numerical values of mean number of wounded nucleons in 5% and 10% of the most central Ar+Sc collisions. Values for 5% taken from Ref. [70], while the ones for 10% come from Ref. [72].

6.3 Transverse momentum spectra in mid-rapidity

Transverse momentum spectra at mid-rapidity are obtained from double-differential spectrum as described in the previous section. The mid-rapidity

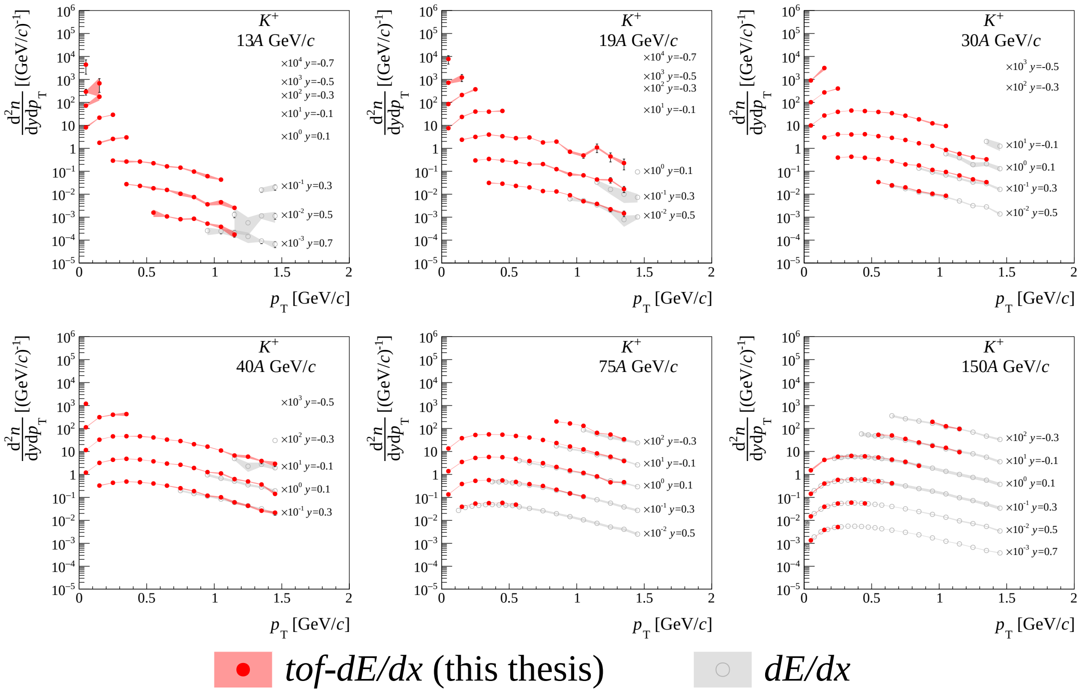

Figure 6.7: Transverse momentum spectra in rapidity slices of positively charged kaons (plotted with red color). Rapidity values given on the plots correspond to the center of the given interval. Shaded bands show systematic uncertainties. Spectra were scaled for ease of viewing. Results of the dE/dx analysis [75] are shown for the comparison (shown in grey).

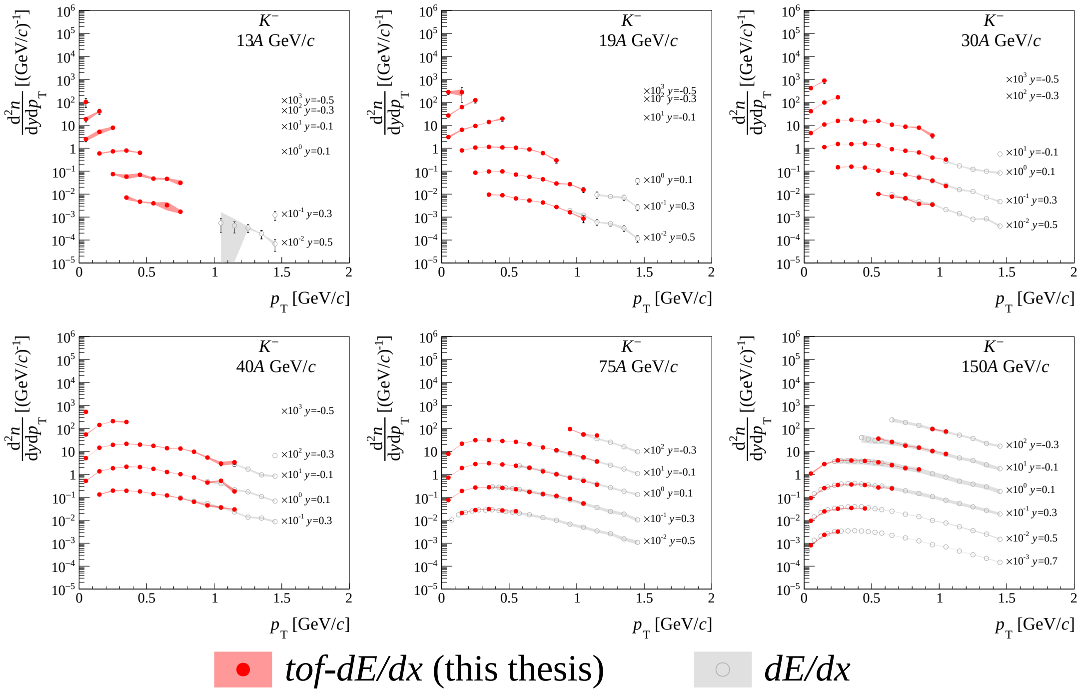

Figure 6.8: Transverse momentum spectra in rapidity slices of negatively charged kaons (plotted with red color). Rapidity values given on the plots correspond to the center of the given interval. Shaded bands show systematic uncertainties. Spectra were scaled for ease of viewing. Results of the dE/dx analysis [75] are shown for the comparison (shown in grey).

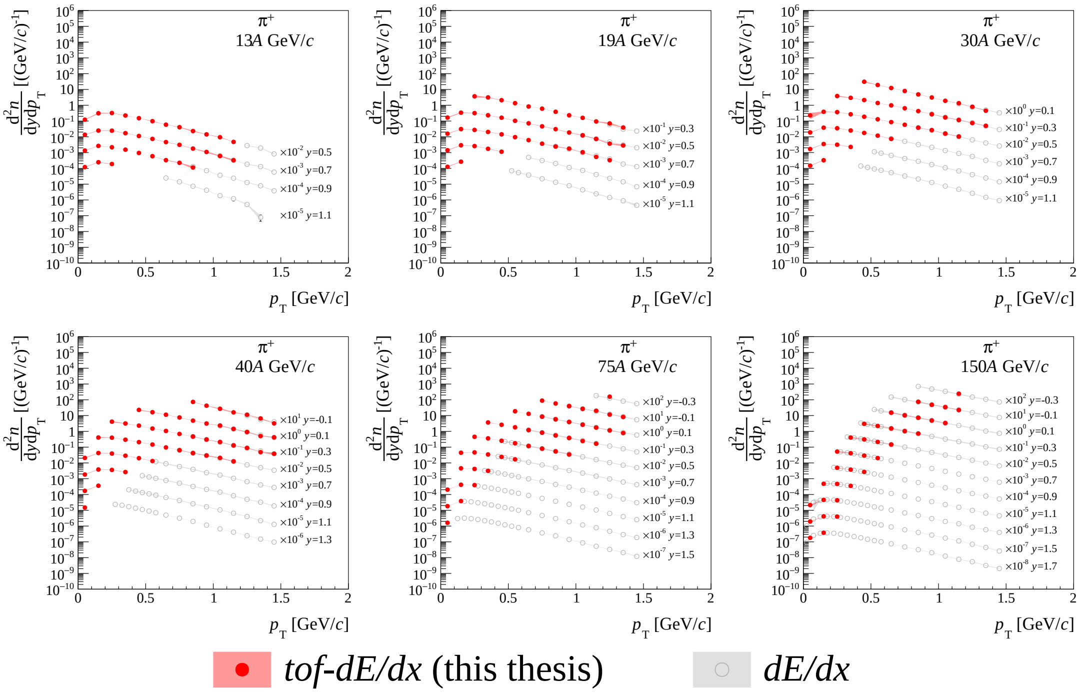

Figure 6.9: Transverse momentum spectra in rapidity slices of positively charged pions (plotted with red color). Rapidity values given on the plots correspond to the center of the given interval. Shaded bands show systematic uncertainties. Spectra were scaled for ease of viewing. Results of the dE/dx analysis [75] are shown for the comparison (shown in gray).

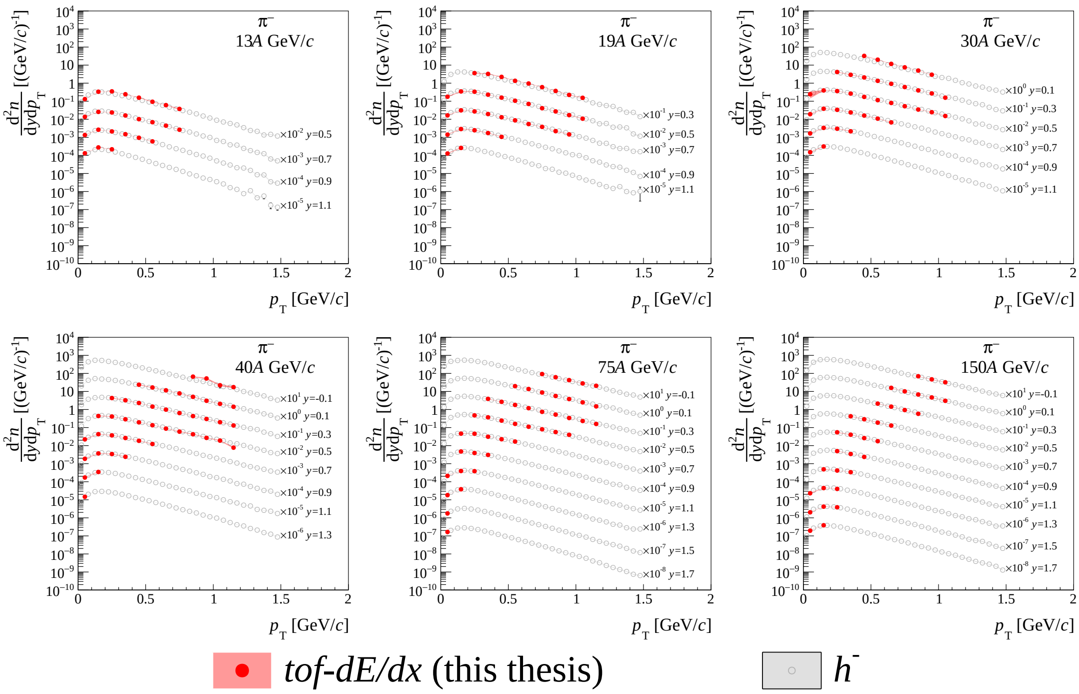

Figure 6.10: Transverse momentum spectra in rapidity slices of negatively charged pions (plotted with red color). Rapidity values given on the plots correspond to the center of the given interval. Shaded bands show systematic uncertainties. Spectra were scaled for ease of viewing. Results of the h^- analysis [70] are shown for the comparison (shown in grey).

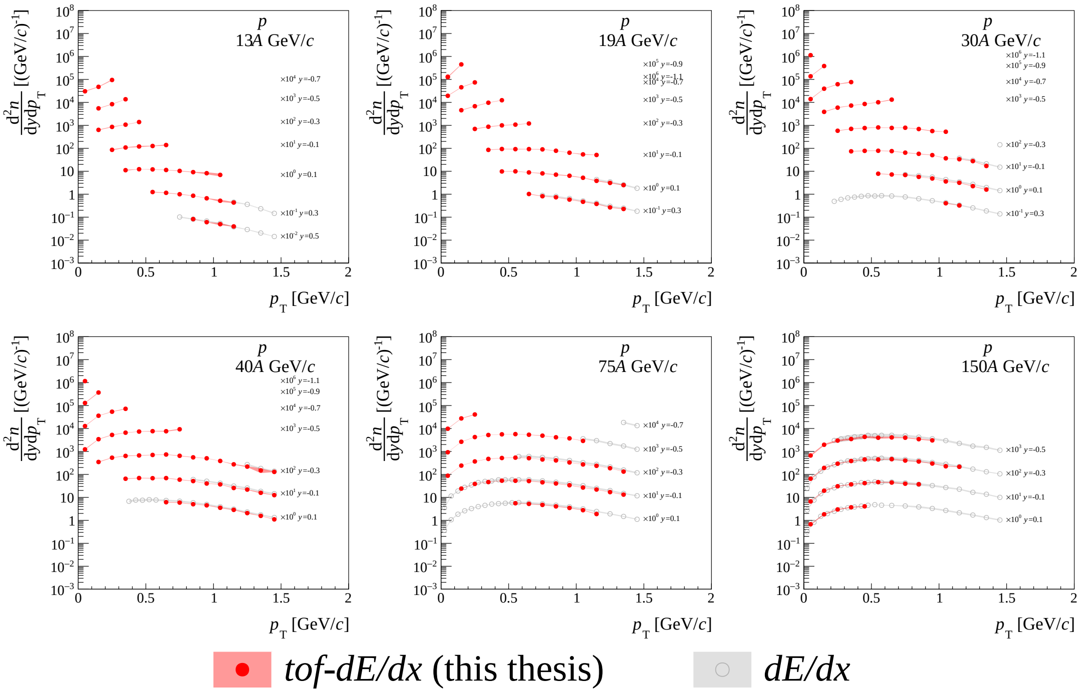

Figure 6.11: The transverse momentum spectra in rapidity slices of protons (plotted with red color). Rapidity values given on the plots correspond to the center of the given interval. Shaded bands show systematic uncertainties. Spectra were scaled for ease of viewing. Results of the dE/dx analysis [75] are shown for the comparison (shown in gray).

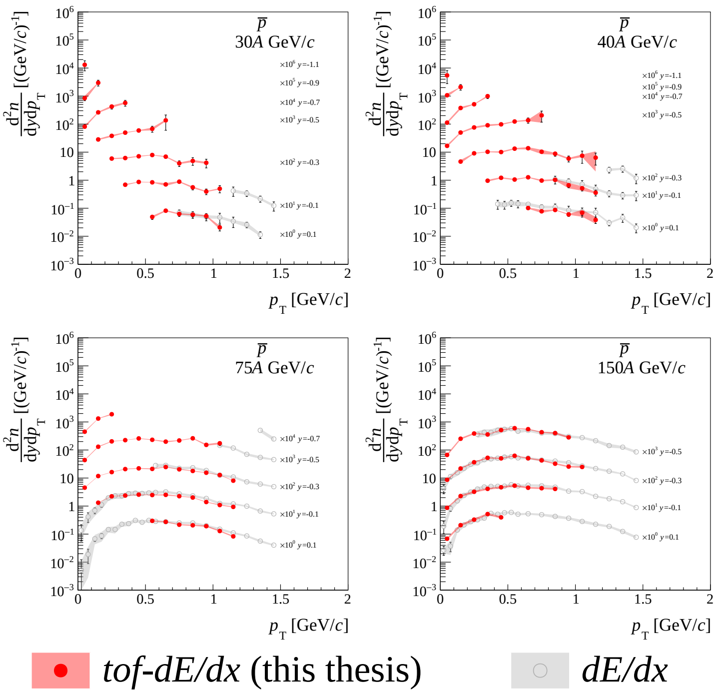

Figure 6.12: The transverse momentum spectra in rapidity slices of anti-protons (plotted with red color). Rapidity values given on the plots correspond to the center of the given interval. Shaded bands show systematic uncertainties. Spectra were scaled for ease of viewing. Results of the dE/dx analysis [75] are shown for the comparison (shown in gray).

interval definition was selected (individually for all beam momenta) to be closest to $y \approx 0$, depending on the available acceptance. The exact values of the intervals are specified in table 6.2. The p_{T} spectra are parametrised with the following exponential function (Eq. 1.6, transformed to p_{T} space):

$$f(p_{\mathrm{T}}) = S \cdot p_{\mathrm{T}} \cdot \exp\left(-\frac{\sqrt{p_{\mathrm{T}}^2 + m^2} - m}{T}\right), \quad (6.2)$$

where T is the so-called *inverse slope parameter*, S is the normalisation factor and m denotes the rest mass of the particle in consideration.

Parametrisation of the spectrum with equation 6.2 allows its extrapolation toward the unmeasured region, up to $p_{\mathrm{T}} = 2$ GeV/c. Direct measurements of the spectrum combined with the extrapolation allow calculation of the particle yield at mid-rapidity ($\mathrm{d}n/\mathrm{d}y$). The $\mathrm{d}n/\mathrm{d}y$ is calculated as the sum of the measured points and the integral of the function 6.2 beyond the measurement range:

$$\frac{\mathrm{d}n}{\mathrm{d}y} = \sum_i \Delta p_{\mathrm{T}} \cdot \left(\frac{\mathrm{d}^2 n}{\mathrm{d}y \mathrm{d}p_{\mathrm{T}}}\right)_{\mathrm{measured}} + \int_0^{p_{\mathrm{T}}^{\mathrm{min}}} f(p_{\mathrm{T}}) \mathrm{d}p_{\mathrm{T}} + \int_{p_{\mathrm{T}}^{\mathrm{max}}}^{2} f(p_{\mathrm{T}}) \mathrm{d}p_{\mathrm{T}}, \quad (6.3)$$

where Δp_{T} is the width of the transverse momentum bin, $p_{\mathrm{T}}^{\mathrm{min}}$ and $p_{\mathrm{T}}^{\mathrm{max}}$ denote the lower and the upper limit of the measurement acceptance in transverse momentum, respectively. The summation is over all measured points of the spectrum. To account for possible bias caused by the arbitrary choice of the function 6.2, a quarter of the total contribution to the yield coming from the extrapolation is added in quadrature to the systematic uncertainty of the mid-rapidity yield.

6.3.1 Kaon spectra in mid-rapidity

The transverse momentum spectra of charged kaons in mid-rapidity for six beam momenta are presented in Fig. 6.13. The exact mid-rapidity interval definition is given in table 6.2. Shaded bands show the systematic uncertainties of the measurements. The symmetry of the $K^{\pm}$ spectra with respect

p_{beam} [GeV/c]	$y_K \approx 0$		$y_p \approx 0$	
	y_{min}	y_{max}	y_{min}	y_{max}
13A	0.2	0.4	0.0	0.2
19A	0.0	0.2	-0.2	0.0
30A	0.0	0.2	-0.2	0.0
40A	0.0	0.2	-0.2	0.0
75A	0.0	0.2	-0.2	0.0
150A	0.0	0.2	-0.2	0.0

Table 6.2: Definition of the mid-rapidity intervals $[y_{min}, y_{max}]$ for kaons ($y_K \approx 0$) and protons ($y_p \approx 0$).

to $y = 0$ was verified with available theoretical models to be within 1%. Thus for 13A, 19A and 30A GeV/c the missing points in the low p_T region (see Fig. 6.1 and Fig. 6.2) are complemented with measured reflections of the spectrum with respect to $y = 0$. The solid lines correspond to the fitted function (Eq. 6.2, with $m \to m_K$ substitution). The function is fitted to the measured spectrum and the reflected points. The exponential dependence describes the kaon p_T spectra at mid-rapidity well.

The dn/dy yield of charged kaons in mid-rapidity is obtained from the measured spectrum (including points reflected with respect to $y = 0$) and fitted function with the use of Eq. 6.3. The yields of K^+ and K^- calculated with this procedure, together with statistical and systematic uncertainties, are summarised in table 6.3. Values of the inverse slope parameter T resulting from the fit of p_T spectra of $K^\pm$ with function 6.2 can be found in table 6.4.

The properties of the charged kaon production in mid-rapidity are of particular interest for studies of the onset of deconfinement [76]. A more detailed look at the quantities obtained in this section will be given in Sec. 6.4

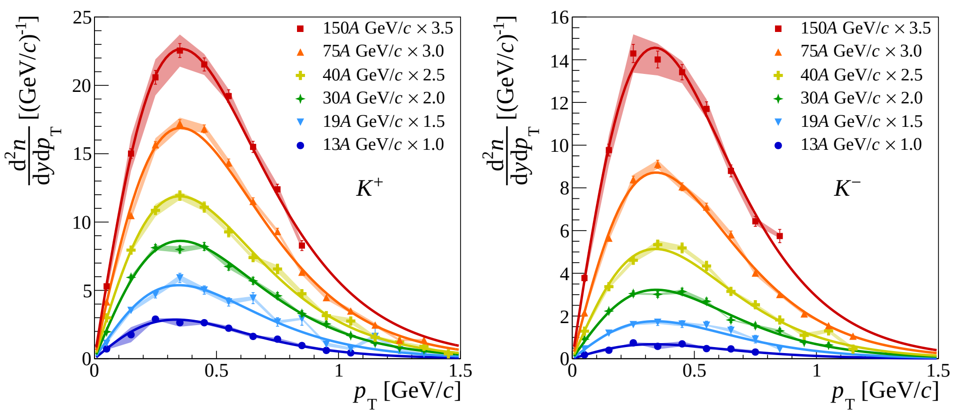

Figure 6.13: Transverse momentum spectra of K^+ (*left*) and K^- (*right*) in mid-rapidity produced in inelastic Ar+Sc interactions. Shaded bands show systematic uncertainties. The lines represent fitted functions (Eq. 6.2, with $m \to m_K$ substitution). The spectra were scaled for better readability.

p_{beam} [GeV/c]	$\left(\frac{dn}{dy}\right)_{y\approx 0}(K^+)$	$\left(\frac{dn}{dy}\right)_{y\approx 0}(K^-)$	$\left(\frac{K^+}{K^-}\right)_{y\approx 0}$
13A	$1.879 \pm 0.042 \pm 0.073$	$0.454 \pm 0.023 \pm 0.030$	$4.140 \pm 0.230 \pm 0.476$
19A	$2.633 \pm 0.082 \pm 0.040$	$0.811 \pm 0.034 \pm 0.029$	$3.247 \pm 0.169 \pm 0.192$
30A	$3.026 \pm 0.038 \pm 0.027$	$1.113 \pm 0.020 \pm 0.016$	$2.717 \pm 0.059 \pm 0.068$
40A	$3.346 \pm 0.041 \pm 0.035$	$1.424 \pm 0.023 \pm 0.019$	$2.349 \pm 0.048 \pm 0.060$
75A	$4.036 \pm 0.025 \pm 0.036$	$2.000 \pm 0.016 \pm 0.023$	$2.018 \pm 0.020 \pm 0.044$
150A	$4.632 \pm 0.043 \pm 0.165$	$2.814 \pm 0.031 \pm 0.102$	$1.646 \pm 0.024 \pm 0.125$

Table 6.3: Numerical values of the K meson yields (dn/dy) in mid-rapidity. The values are provided with statistical (σ_{stat}) and systematic (σ_{sys}) uncertainties in the form: dn/d$y \pm \sigma_{stat} \pm \sigma_{sys}$.

p_{beam} [GeV/c]	$T(K^{+})$ [MeV]	$T(K^{-})$ [MeV]
13A	$187.20 \pm 6.19 \pm 2.59$	$188.81 \pm 17.38 \pm 10.04$
19A	$199.12 \pm 6.03 \pm 2.81$	$194.14 \pm 11.47 \pm 3.22$
30A	$204.20 \pm 2.67 \pm 1.23$	$195.82 \pm 4.51 \pm 1.51$
40A	$202.20 \pm 2.32 \pm 1.57$	$192.77 \pm 3.09 \pm 1.69$
75A	$206.27 \pm 1.19 \pm 1.43$	$195.95 \pm 1.57 \pm 1.13$
150A	$209.25 \pm 2.73 \pm 3.83$	$191.87 \pm 2.91 \pm 3.51$

Table 6.4: Numerical values of the inverse slope parameter T of the K meson p_{T} spectra in mid-rapidity. The values are provided with statistical (σ_{stat}) and systematic (σ_{sys}) uncertainties in the form: $T \pm \sigma_{\text{stat}} \pm \sigma_{\text{sys}}$.

6.3.2 Proton and anti-proton spectra in the mid-rapidity

The transverse momentum spectra of protons and anti-protons in mid-rapidity for six beam momenta (four for anti-protons) are presented in Fig. 6.14. The exact mid-rapidity intervals are given in table 6.2. The shaded bands show systematic uncertainties of the measurements. The solid lines correspond to the fitted exponential function (Eq. 6.2, with $m \to m_p$ substitution).

The dn/dy yield of protons and anti-protons in mid-rapidity is obtained in the same way as for kaons (Eq. 6.3). The resulting yields of p and $\bar{p}$, together with statistical and systematic uncertainties, are summarised in table 6.5.

6.4 Study of the onset of deconfinement

In this section signatures of the onset of deconfinement studied in the scope of this thesis will be presented. The energy dependence of strangeness production properties in Ar+Sc collisions is compared with the available data on p+p ([36, 77, 77–80]), Be+Be ([34]), Au+Au ([81–86]), and Pb+Pb ([32,

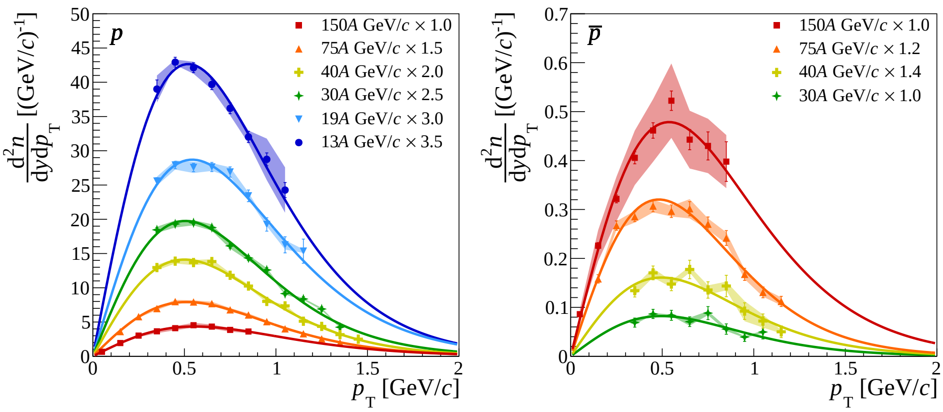

Figure 6.14: Transverse momentum spectra of p (*left*) and $\bar{p}$ (*right*) produced at mid-rapidity in inelastic Ar+Sc interactions. Shaded bands show systematic uncertainties. The lines represent fitted functions (Eq. 6.2, with $m \to m_p$ substitution). The spectra were scaled for better readability.

p_{beam} [GeV/c]	$\left(\frac{dn}{dy}\right)_{y\approx0}(p)$	$\left(\frac{dn}{dy}\right)_{y\approx0}(\bar{p})$
13A	$11.910 \pm 0.109 \pm 0.503$	-
19A	$9.757 \pm 0.133 \pm 0.409$	-
30A	$7.467 \pm 0.047 \pm 0.128$	$0.077 \pm 0.004 \pm 0.003$
40A	$6.598 \pm 0.045 \pm 0.083$	$0.108 \pm 0.004 \pm 0.004$
75A	$5.074 \pm 0.021 \pm 0.089$	$0.240 \pm 0.004 \pm 0.006$
150A	$4.673 \pm 0.026 \pm 0.426$	$0.495 \pm 0.016 \pm 0.044$

Table 6.5: Numerical values of the p and $\bar{p}$ yields (dn/dy) in mid-rapidity. The values are provided with statistical (σ_{stat}) and systematic (σ_{sys}) uncertainties in the form: $dn/dy \pm \sigma_{stat} \pm \sigma_{sys}$.

80, 87–89]) collisions. The world data originate from various experiments at the AGS, SPS, RHIC, and LHC accelerators.

6.4.1 *The Step* - energy dependence of the inverse slope parameter T

The simple exponential parametrisation of the kaon transverse momentum spectra (Eq. 6.2) yields values for the inverse slope parameter T, summarized in table 6.4. The T values obtained for Ar+Sc collisions at six beam momenta from the CERN SPS energy range as a function of the collision energy ($\sqrt{s_{NN}}$) for positively and negatively charged kaons are presented in Fig. 6.15. The energy dependence of the inverse slope parameter in Ar+Sc collisions exhibits a characteristic plateau in the SPS energy range, visible prominently in Pb+Pb data. Ar+Sc values of the T parameter are located slightly below Pb+Pb, yet still significantly higher than Be+Be.

The value of the inverse slope parameter within hydrodynamical models is interpreted as a kinetic freeze-out temperature with modifications from

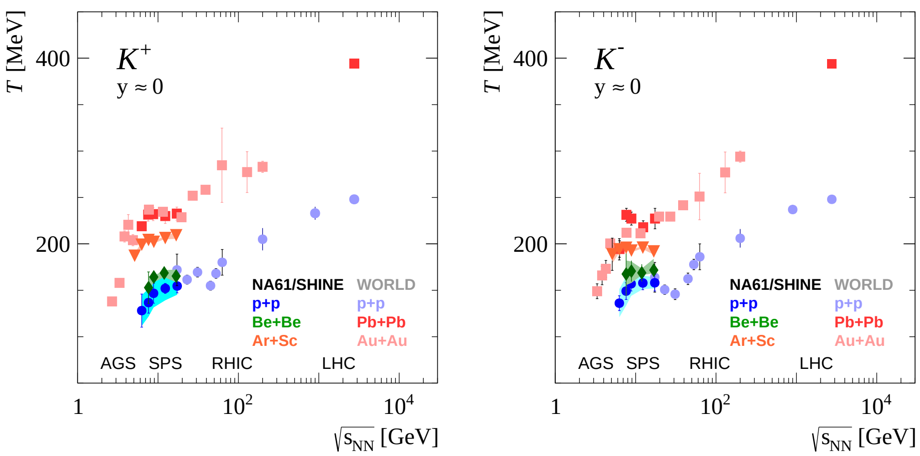

Figure 6.15: The energy dependence of the inverse slope parameter T of the K transverse momentum spectra in mid- rapidity. Parameter presented for positively (*left*) and negatively (*right*) charged kaons. Results for p+p ([36,77,77–80]), Be+Be ([34]), Ar+Sc (this thesis), Au+Au ([81–86]), and Pb+Pb ([32,80,87–89]) are shown.

transverse flow (see Ref. [76] and Eq. 1.7). In this scope, the results presented in this thesis may indicate that the kinetic freeze-out temperature values in Ar+Sc are closer to Pb+Pb (a large system) than Be+Be (a small system).

6.4.2 *The Horn* - energy dependence of K/π ratio

The second observable of the onset of deconfinement is the energy dependence of the strangeness to entropy ratio. The calculation of the K^-/π^- ratio is straightforward, as the π^- spectra are measured in a broad acceptance, including mid-rapidity, by the h^- method [70]. The h^- analysis results are scaled to 10% centrality with the procedure described in Sec. 6.2. Unfortunately, neither the $tof - \mathrm{d}E/\mathrm{d}x$ nor the $\mathrm{d}E/\mathrm{d}x$ identification methods offer acceptance for a direct π^+ meson measurement in the mid-rapidity region. A study with available theoretical models showed that the differences of π^+ and π^- mid-rapidity yields in Ar+Sc collisions are below 8%. Fig. 6.16 presents the π^+/π^- multiplicity ratio in mid-rapidity based on model predictions as a function of collision energy. Hence, for calculating the K^+/π^+ ratio, the π^- multiplicity from the h^- method scaled to 10% centrality with Eq. 6.1 was taken. The possible differences in the real $\pi^\pm$ multiplicities were accounted for, based on model studies, by adding in quadrature 8% of the K^+/π^+ ratio to its systematic uncertainty.

Fig. 6.17 presents the energy dependence of the K/π ratio for both charge signs, together with a comparison with available world data on *p*+*p*, Be+Be, Au+Au, and Pb+Pb interactions. The values of the K^+/π^+ measured for Ar+Sc are situated between Be+Be and Pb+Pb, similarly to the inverse slope parameter. The ratio shows systematic growth with collision energy within total uncertainties. The values are between large (Pb+Pb) and small (*p*+*p*, Be+Be) systems for low SPS energies, while at the maximal SPS energy measured K^+/π^+ is close to the Pb+Pb value. The non-monotonic energy dependence of the K^+/π^+ ratio, prominent in Pb+Pb measurements, is not

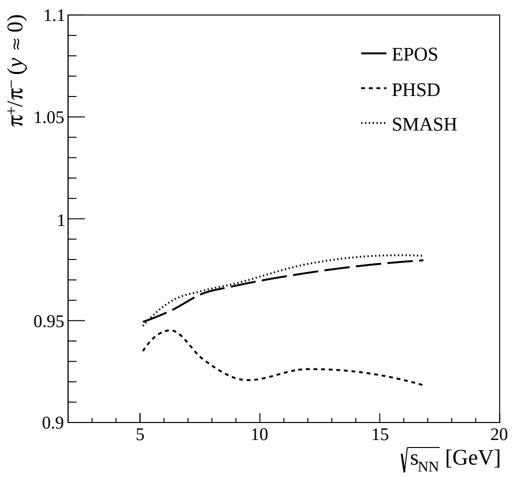

Figure 6.16: The π^+/π^- multiplicity ratio at mid-rapidity calculated based on predictions of EPOS 1.99 [67, 90], PHSD 4.0 [91–93] and SMASH 2.0 [94, 95] models (see Sec. 6.6).

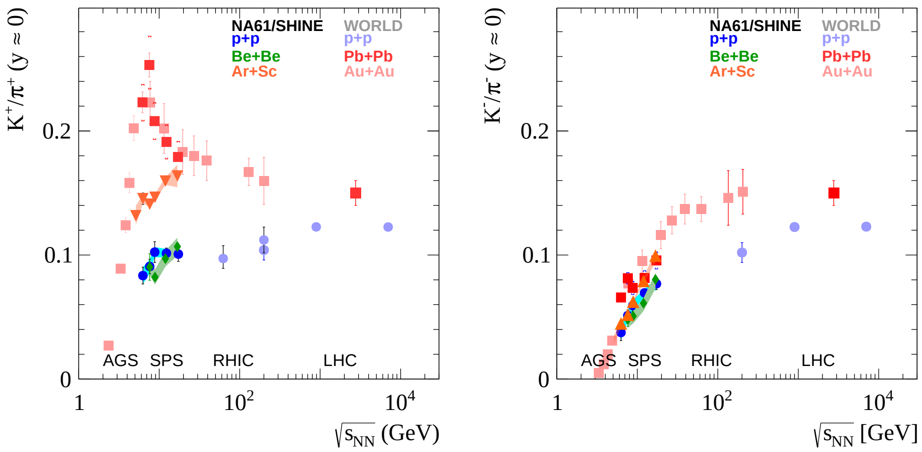

Figure 6.17: Energy dependence of the K/π ratio in mid-rapidity. Ratio presented for positively (*left*) and negatively (*right*) hadrons. Results for p+p ([36,77,77–80]), Be+Be ([34]), Ar+Sc (this thesis), Au+Au ([81–86]), and Pb+Pb ([32,80,87–89]) are shown.

observed in Ar+Sc data. The K^-/π^- ratio in Ar+Sc exhibits a similar energy dependence to other systems selected for the comparison in the SPS energy range.

6.5 System size dependence

In this section, the important onset of deconfinement observables, the K^+/π^+ ratio and the inverse slope parameter of the p_T spectra of K^+ are studied as a function of the colliding system size. The mean number of wounded nucleons $\langle W \rangle$ was chosen as the system size measure. Figures 6.18 and 6.19 present the system size dependence of K^+/π^+ and the inverse slope parameter, respectively. The dependence is shown for 19A, 30A, 40A, 75A, and 150A GeV/c beam momenta. The Ar+Sc system is the first analyzed dataset in NA61/SHINE where particle identification was possible at 13A GeV/c. Thus the comparison for the lowest SPS energy is not shown.

Similarity between strangeness production properties measured in central Be+Be collisions and p+p interactions may suggest that for small systems, particle production originates from small clusters of strongly-interacting matter, as predicted by the WNM. When moving from p+p and Be+Be to Ar+Sc, an apparent quantitative difference in K^+/π^+ ratio is present for all studied beam momenta. The Ar+Sc results are similar to those obtained for central Pb+Pb collisions, where the particles are produced from a single, large cluster of equilibrated strongly-interacting matter known as the *fireball*. It may indicate the existence of the *onset of fireball* [96] which refers to the threshold in system size for the creation of large clusters in the heavy-ion collisions, leading to the creation of the fireball in large colliding systems. The inverse slope parameter T changes approximately linearly with the size of the colliding system.

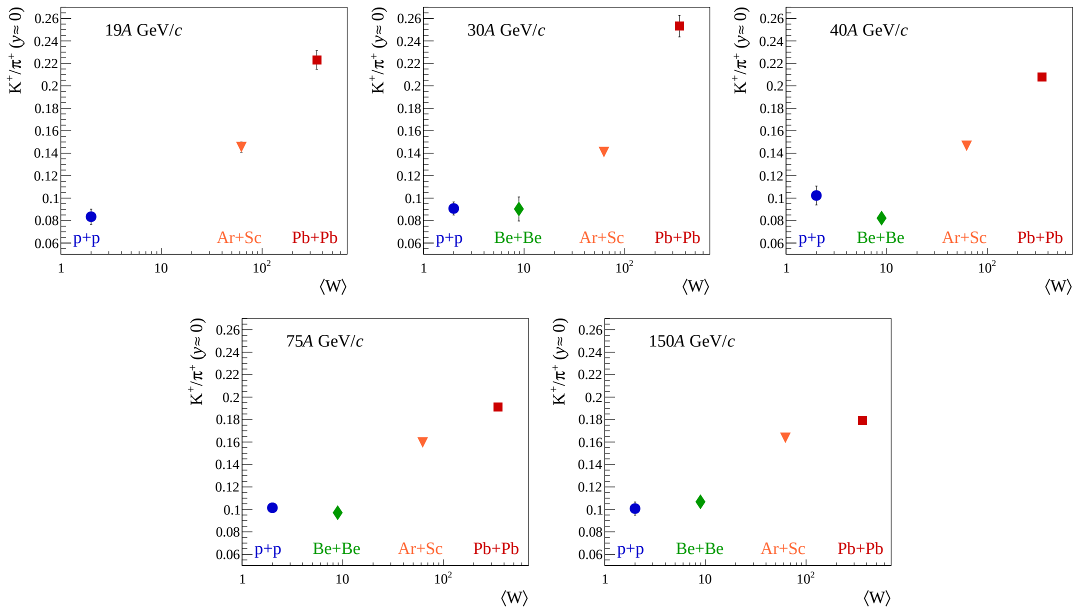

Figure 6.18: System size dependence of K^+/π^+ yield ratio in mid-rapidity measured at 19A-150A GeV/c. The mean number of wounded nucleons $\langle W \rangle$ is used as a measure of the system size. Results for p+p ([36]), Be+Be ([34]), Ar+Sc (this thesis), and Pb+Pb ([32, 88]) are shown.

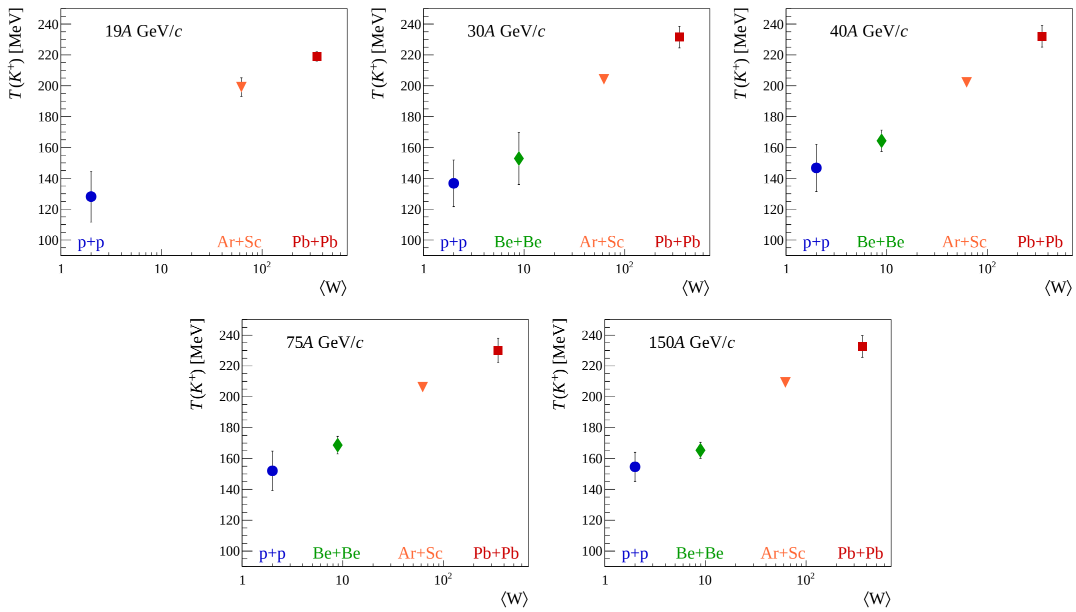

Figure 6.19: System size dependence of the inverse slope parameter T of K^+ transverse momentum spectra in mid-rapidity measured at 19A-150A GeV/c. The mean number of wounded nucleons $\langle W \rangle$ is used as a measure of the system size. Results for p+p ([36]), Be+Be ([34]), Ar+Sc (this thesis), and Pb+Pb ([32, 88]) are shown.

6.6 Comparison with theoretical models

In this section, a comparison of obtained results with three selected theoretical models is shown. Results were compared with predictions of EPOS 1.99 [67, 90], PHSD 4.0 [91–93] and SMASH 2.0 [94, 95].

Kaon production properties

Transverse momentum spectra of charged kaons in mid-rapidity are compared with the models. Figures 6.20 and 6.21 show comparisons of K^+ and K^- transverse momentum spectra with models, respectively. The EPOS model predicts the p_T spectrum width to be systematically smaller than the measured values for all beam momenta and both charge signs. The SMASH spectra are slightly wider than for EPOS. Still, they are narrower than the measured ones. On the other hand, PHSD properly describes the shape of the spectra. PHSD provides reasonable quantitative agreement with the measurement results for the lowest beam momentum, though for higher collision energies it overestimates kaon production. EPOS predictions show an opposite trend with collision energy: for higher beam momenta, they tend to be systematically smaller than data. SMASH underestimates charged kaon production for all analyzed beam momenta.

Integrated p_T spectra were also compared with model predictions. The dn/dy yields of models are obtained with the procedure described in Sec. 6.3, the same as for the experimental data. A comparison of kaon yields in mid-rapidity with models is presented in Fig. 6.22. K^- yields predicted by PHSD and EPOS are in agreement with experimental data for the lowest analyzed collision energies. The shape of the energy dependence of the K^+ yield is well described by PHSD, apart from a slight overestimation in higher beam momenta. EPOS shows a significantly smaller slope of K^+ yield energy dependence for higher collision energies, while SMASH, properly predicts the shape but fails quantitatively. Similarly, the negatively charged kaon yield for higher collision energies is enveloped between the EPOS and PHSD predictions. Here, the PHSD overestimation is more pronounced, resulting in less agreement in the energy dependence shape. The SMASH predictions are again below the measured kaon yields for all beam momenta.

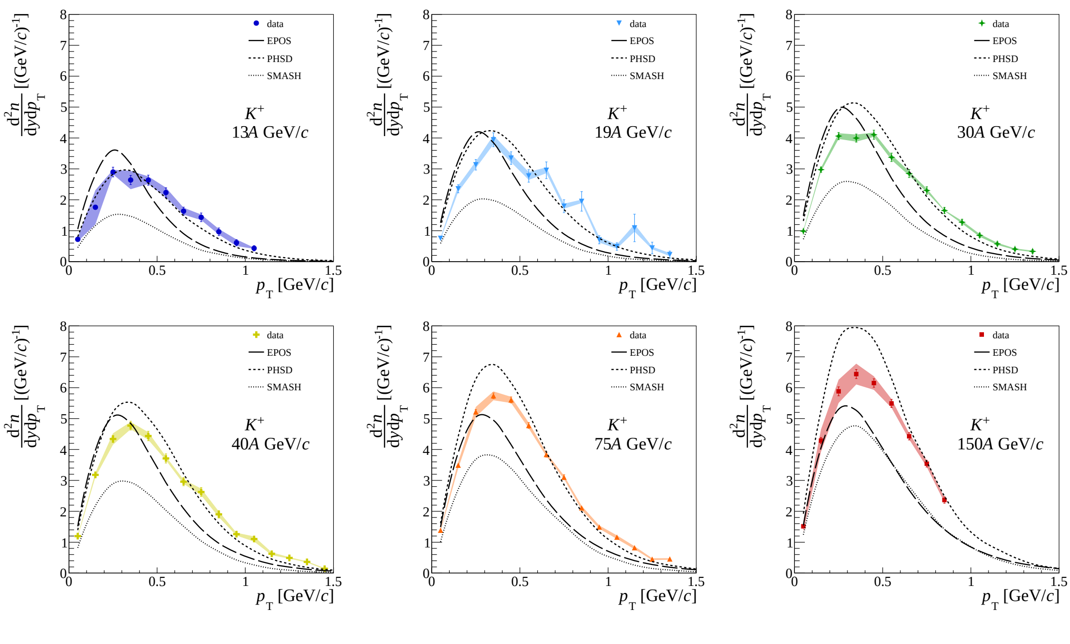

Figure 6.20: Comparison of the transverse momentum spectra of K^+ mesons produced in central Ar+Sc collisions with EPOS 1.99 [67, 90], PHSD 4.0 [91–93] and SMASH 2.0 [94, 95] models.

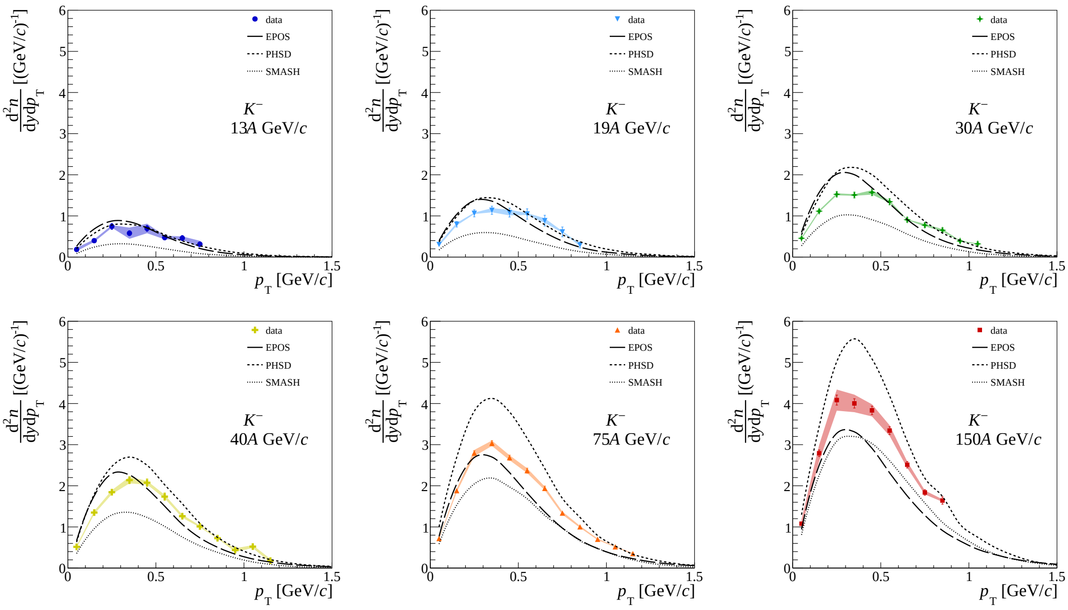

Figure 6.21: Comparison of the transverse momentum spectra of K^- mesons produced in central Ar+Sc collisions with EPOS 1.99 [67, 90], PHSD 4.0 [91–93] and SMASH 2.0 [94, 95] models.

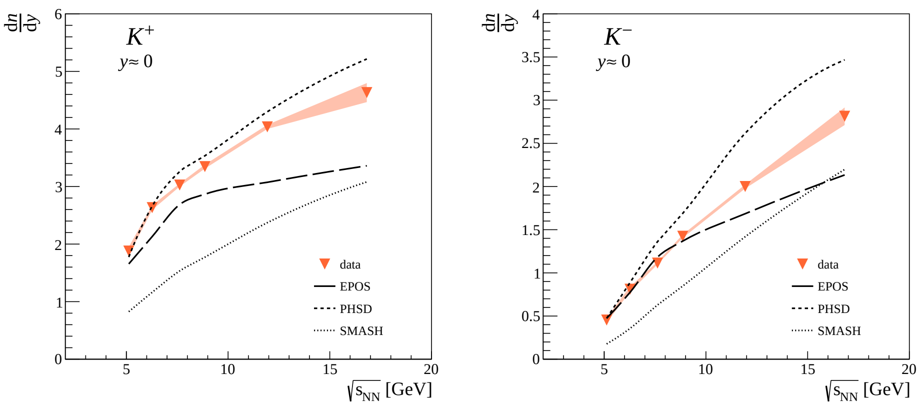

Figure 6.22: Comparison of the energy dependence of K^+ (*left*) and K^- (*right*) production at mid-rapidity in central Ar+Sc collisions with EPOS 1.99 [67, 90], PHSD 4.0 [91–93] and SMASH 2.0 [94, 95] models.

The K^+/K^- ratio comparison is shown in Fig. 6.23. The EPOS and PHSD models underestimate the ratio, with EPOS providing better estimation for lower beam momenta and PHSD in the higher ones. The SMASH prediction agrees with the measurement for the two lowest beam momenta, while for higher ones the ratio is underestimated, like for the other two models.

Figure 6.24 shows comparisons of the inverse slope parameters of the kaon p_T spectra in mid-rapidity with models. The values of T parameter for the model predictions were obtained in the same way as for the experimental data by fitting the function 6.2. The substantial qualitative differences in the p_T spectra shapes of charged kaons predicted by EOPS with respect to the experimental data are reflected in the values of the fitted inverse slope parameters. The T predicted by the EPOS model is lower than the

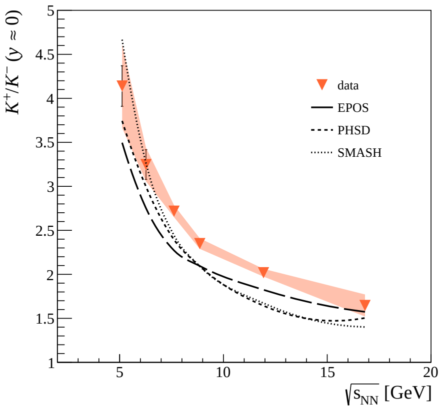

Figure 6.23: Comparison of the energy dependence of K^+/K^- ratio at mid-rapidity in central Ar+Sc collisions with EPOS 1.99 [67, 90], PHSD 4.0 [91–93] and SMASH 2.0 [94, 95] models.

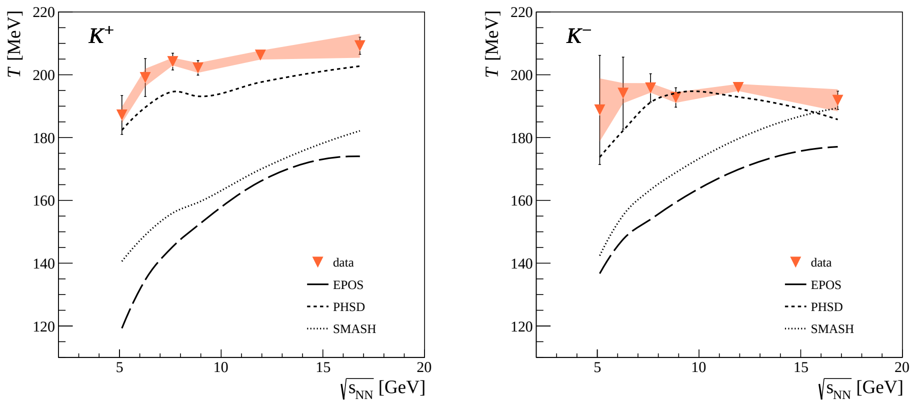

Figure 6.24: Comparison of the energy dependence of the inverse slope parameter of K^+ (*left*) and K^- (*right*) transverse momentum spectra at mid-rapidity in central Ar+Sc collisions with EPOS 1.99 [67,90], PHSD 4.0 [91–93] and SMASH 2.0 [94,95] models.

measurement results by up to 50% of the predicted value. The energy dependence predicted by the EPOS model is also different than what was measured. SMASH predictions are slightly larger than EPOS predictions, still well below the measured values for all beam momenta but the maximal SPS momentum, where the T value predicted for negatively charged kaons, agrees with the experiment. PHSD, however, is in reasonably good agreement with the experimental results. The predicted energy dependence shape accurately reflects the measurements, yet it slightly underestimates the T values for positively charged kaons.

The K/π ratio is the most prominent signature of the onset of deconfinement. The measurement results were compared with theoretical models on Fig. 6.25. The shape of the energy dependence of the K/π ratio predicted by the EPOS model is in qualitative agreement with the measurements. Quantitatively, values predicted by EPOS are lower than the observed ones for both charge signs. The shape of the K/π energy dependence predicted by SMASH is similar to EPOS, but the predicted values are systematically

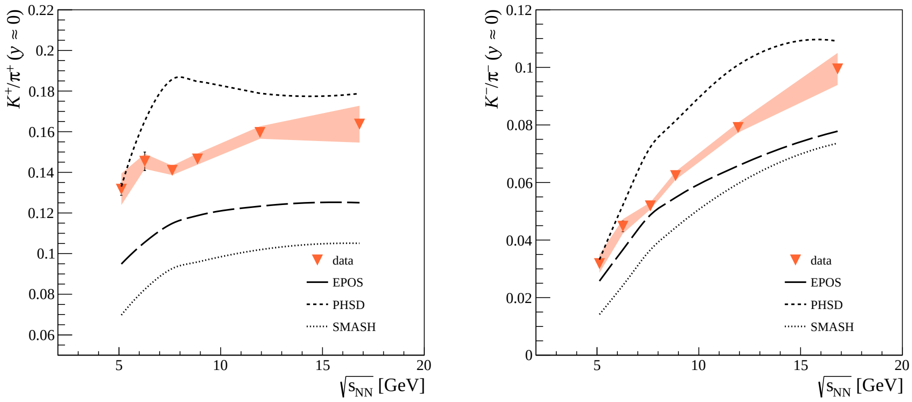

Figure 6.25: Comparison of the energy dependence of K^+/π^+ (*left*) and K^-/π^- (*right*) ratios at mid-rapidity in central Ar+Sc collisions with EPOS 1.99 [67, 90], PHSD 4.0 [91–93] and SMASH 2.0 [94, 95] models.

lower than EPOS, leading to further disagreement with experimental measurements. PHSD, on the other hand, predicts a very different shape of the K^+/π^+ energy dependence, which is not in agreement with the data. The qualitative difference in the case of negatively charged kaons is less prominent but still visible.

(Anti-)proton production properties

The transverse momentum spectra of protons and anti-protons in mid-rapidity were also compared with the models. Figures 6.26 and 6.27 show the comparisons of p_T spectra of p and $\bar{p}$ with the models, respectively. For anti-protons (Fig. 6.27), comparison with PHSD is not shown due to low $\bar{p}$

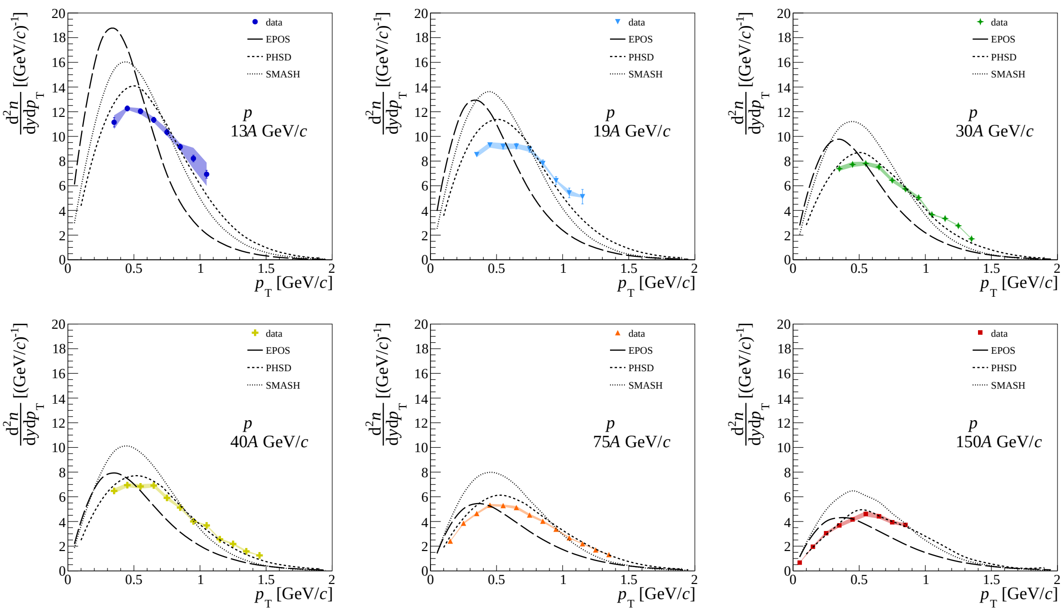

Figure 6.26: Comparison of the transverse momentum spectra of protons produced in central Ar+Sc collisions with EPOS 1.99 [67, 90], PHSD 4.0 [91–93] and SMASH 2.0 [94, 95] models.

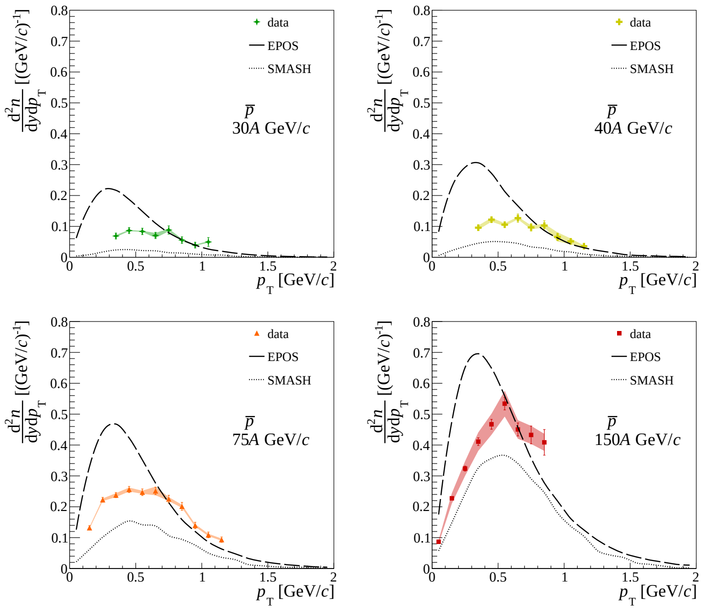

Figure 6.27: Comparison of the transverse momentum spectra of anti-protons produced in central Ar+Sc collisions with EPOS 1.99 [67, 90] and SMASH 2.0 [94, 95] models.

yield and insufficient statistics of the available PHSD sample. Qualitatively all studied models predict a shape of the $p/\bar{p}$ transverse momentum spectra which is narrower than the measured one, with EPOS providing poorest agreement with the data.

Integrated p and $\bar{p}$ yields are compared with models in Fig. 6.28. All three models quantitatively predict the measured shape of the p production energy dependence. PHSD is in very good agreement with the measured p multiplicities. The p yield is slightly overestimated by SMASH and underestimated by EPOS for higher beam momenta. The $\bar{p}$ production predicted by the EPOS model is larger than the measured values for all beam momenta except the highest one. The EPOS predicted slope of the energy

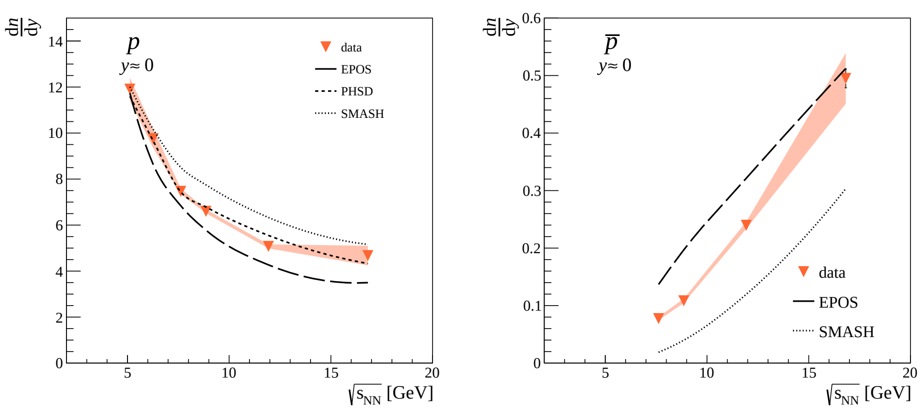

Figure 6.28: Comparison of the energy dependence of p (*left*) and $\bar{p}$ (*right*) production at mid-rapidity in central Ar+Sc collisions with EPOS 1.99 [67, 90], PHSD 4.0 [91–93] and SMASH 2.0 [94, 95] models.

dependence of the anti-proton production in the mid-rapidity is also less steep than the measured value. Qualitatively, SMASH predicts the correct shape of the $\bar{p}$ yield energy dependence but vastly underestimates the absolute values.

In summary, none of the models used for the comparison was able to reproduce all the features of the K^+, K^-, π^+, π^-, p, and $\bar{p}$ spectra measured in central Ar+Sc collisions. PHSD works best at describing the properties of the charged kaon production. However, it fails to predict the K/π ratio.

Chapter 7

Summary and outlook

The presented thesis concerns hadron production measurements in 10% of the most central Ar+Sc collisions collected by the NA61/SHINE experiment at the CERN SPS.

The main results of this thesis are charged particle production spectra : p, $\bar{p}$, π^+, π^-, K^+, K^-. The results were obtained for beam momenta of 13A, 19A, 30A, 40A, 75A, and 150A GeV/c. Particle identification based on simultaneous measurement of energy loss and time-of-flight measurement was performed. The results were corrected for detector and reconstruction efficiencies, contributions from weak decays, and interactions with detector material. Identified particle spectra were presented as a function of rapidity and transverse momentum.

Special attention was paid to $K^{\pm}$ mesons production properties. Charged kaons are, next to Λ baryons, the most abundant strange particles produced in $A + A$ collisions in the CERN SPS energy range. Properties of strangeness production are of particular interest for studying the onset of deconfinement. Transverse momentum spectra of charged kaons in mid-rapidity were obtained. The spectra were parametrized with an exponential function yielding the inverse slope parameter, enabling obtaining the kaon yields in said rapidity interval.

Signatures of the onset of deconfinement were studied as a function of the collision energy in the range available at the SPS. Based on parametrization of charged kaons p_{T} spectra in the mid-rapidity, the inverse slope parameters T_{K^+} and T_{K^-} were obtained. Values these inverse slope parameters as a function of collision energy exhibit a characteristic plateau in the SPS energy range. Quantitatively, experimental results on Ar+Sc collisions fall between Be+Be and Pb+Pb results. The charged kaon to pion production ratio at mid-rapidity was calculated and compared with the available world data. The K^+/π^+ ratio is one of the most prominent signatures of the onset of deconfinement predicted by the SMES. The values of the K^+/π^+ ratio measured for Ar+Sc monotonically grow with the collision energy within the total uncertainties. For the lowest recorded beam momentum, the ratio falls approximately between results for small systems (Be+Be, p+p) and large systems (Pb+Pb). On the other hand, at the maximal SPS energy measured values of the K^+/π^+ ratio are very close to those of Pb+Pb collisions. Such behavior is in partial contradiction with SMES, which predicts Ar+Sc values to be very close to Pb+Pb for all beam momenta in the SPS energy range. Such rapid change of the strangeness production properties when moving from small (p+p, Be+Be) to intermediate (Ar+Sc) systems may be attributed to a transition between small non-equilibrated and large equilibrated clusters of strongly-interacting matter. This is refered to as the Onset of the Fireball. Strangeness production in Ar+Sc collisions is not well-described by statistical (e.g., SMES) nor dynamical (e.g., PHSD) models. The results presented in this dissertation will serve an important role in improving the existing models and developing new ones.

Analysis of the Xe+La and Pb+Pb data collected by NA61/SHINE is currently ongoing, and the first results can be expected in the near future. Data on Xe+La collisions will fill the gap between Ar+Sc and Pb+Pb. The NA61/SHINE experiment, after finishing its two-dimensional scan program in collision energy and system size in 2018, aims to perform precise measurements of open charm production in Pb+Pb collisions in the SPS energy range. The measurements provided by NA61/SHINE in 2022-2024 will enable estimation of the mean number of charm and anti-charm quark pairs $\langle c\bar{c} \rangle$ produced in the full phase space of the Pb+Pb collisions at $40A$ and $150A$ GeV/c beam momenta for the first time. To accomplish this goal, a significant hardware upgrade of the NA61/SHINE spectrometer is ongoing. A brief description of the upgrade can be found in Appendix B.

The rapid change of hadron production properties when moving from p+p and Be+Be to Ar+Sc triggered the first discussions in the NA61/SHINE community on a possible extension of the two-dimensional scan program into smaller colliding systems to further study properties of the onset of fireball. A tentative draft of the possible data taking after CERN LS3 (2025-2028) was presented in [97]. Moreover, new projects such as the RHIC-fixed-target (BNL), SIS100 (GSI), or NICA (JINR) are planned to start operation in the following years. Experimental data from these projects, together with collected and future data from NA61/SHINE, will allow a deeper study of strongly-interacting matter, its equation of state and properties of the onsets of deconfinement and fireball.

Appendix A

Coordinate system and kinematic variables

This appendix introduces the standard coordinate system of the NA61/SHINE detector and the kinematic variables used in this thesis.

A.1 NA61/SHINE coordinate system

The coordinate system used in NA61/SHINE is shown in Fig. 2.1. Due to historical reasons, the origin of the coordinate system is located in the middle of the VERTEX-2 magnet on the beamline. All coordinates and angles described in this appendix are defined in the LAB reference frame. The standard Cartesian, right-handed coordinates are used, with coordinate axes defined as follows:

- z axis is horizontal, coincidental with the beamline,
- x axis is horizontal,
- y axis is vertical, pointing up.

The direction of the x axis is set for the coordinate system to be right-handed. Apart from the Cartesian coordinates, the spherical coordinate system (θ, ϕ) is used in momentum space to describe the direction of particles produced in the interaction. The polar angle, θ, is the angle between the momentum vector and the beam (z) axis:

$$\theta = \arcsin \frac{p_T}{p} \,. \tag{A.1}$$

This angle ranges from 0 to π, where $\theta = 0$ corresponds to particles produced in the forward direction, along the beam axis. The azimuthal angle, ϕ, is the angle defined in $x-y$ plane. It is the angle between the transverse component of the momentum vector (p_T) and the x axis:

$$\phi = \mathrm{arc\,tg} \frac{p_y}{p_x} \,. \tag{A.2}$$

The ϕ angle ranges from 0 to 2π, where $\phi = 0$ corresponds to x axis and $\phi = \pi/2$ to the y axis.

A.2 Kinematic variables

A.2.1 Momentum and transverse variables

The momentum of a particle can be decomposed into components along coordinate axes (p_x, p_y, p_z) defined in the previous section. The magnitude of the momentum vector (total momentum) is expressed by its components in the following way:

$$p = \sqrt{p_x^2 + p_y^2 + p_z^2}\ . \tag{A.3}$$

It is convenient to separate momentum components along the beam axis (*longitudinal* momentum) and perpendicular to the beam axis (*transverse* momentum):

$$p_L = p_z\ , \tag{A.4}$$

$$p_T = \sqrt{p_x^2 + p_y^2}\ . \tag{A.5}$$

The transverse mass of a particle with invariant mass m is defined as:

$$m_T = \sqrt{p_T^2/c^2 + m^2}\ . \tag{A.6}$$

A.2.2 Rapidity

The rapidity, y, is defined as follows:

$$y = \frac{1}{2}\ln\left(\frac{E + p_L c}{E - p_L c}\right), \tag{A.7}$$

where E and p_L denote energy and longitudinal momentum of a particle, respectively. Rapidity is a dimensionless variable with simple and convenient transformation properties under Lorentz boosts along the beam axis. Namely, transformation of rapidity from laboratory (LAB) frame of reference to center-of-mass (CM) frame of reference is additive:

$$y_{CM} = y_{LAB} - \frac{1}{2}y_{beam}. \tag{A.8}$$

The beam rapidity y_{beam} in the formula above is defined as follows:

$$y_{beam} = \frac{1}{2}\ln\left(\frac{E_{beam} + p_{beam}c}{E_{beam} - p_{beam}c}\right),\ E_{beam} = \sqrt{m_p^2 c^4 + p_{beam}^2 c^2}\ . \tag{A.9}$$

where p_{beam} and m_p are the beam momentum and a proton mass, respectively. Rapidity transformations under under Lorentz boosts along the beam axis ensures that the shape of the rapidity spectrum remains invariant under such a transformation.

A.2.3 Collision energy

In a relativistic collision of two particles with masses m_{beam} and m_{target}, the total center-of-mass energy is expressed in Lorentz invariant form (magnitude of the total four-momentum of the system):

$$\sqrt{s} = \sqrt{(E_{beam} + E_{target})^2 - (p_{beam} + p_{target})^2} \,. \tag{A.10}$$

This thesis adopts the convention, widely used in high energy physics, of referring to the collision energy as the center-of-mass energy per nucleon pair $\sqrt{s_{NN}}$. In the case of a fixed target experiment, the target particle is at rest, and the formula for the collision energy becomes:

$$\sqrt{s_{NN}} = \sqrt{2m_p^2 + E_{beam} m_p} \,. \tag{A.11}$$

Appendix B

Upgrade of the NA61/SHINE detector

After Long Shutdown 2 at CERN (LS2, 2019-2021), NA61/SHINE will extend its physics program with high statistics measurements of open charm production in Pb+Pb interactions at the CERN SPS energies, which will allow determination of the mean number of $c\bar{c}$ quark pairs produced in Pb+Pb interactions for the first time at SPS energy range. The experiment will also continue to perform reference measurements for the neutrino and cosmic ray communities [63]. In order to meet the mentioned physics goals, a significant hardware modification of the spectrometer is required. The key points of the upgrade are schematiccaly summarised on Fig. B.1 and are listed below:

1. Construction of a new Vertex Detector
2. Upgrade of the TPC readout electronics
3. Implementation of a new trigger and DAQ systems
4. Upgrade of the PSD
5. Construction of a new ToF-L detector

The new Vertex Detector (VD, upgraded SAVD) will have improved phase space coverage for the open charm reconstruction. The NA61/SHINE TPCs will be equipped with new readout electronics. This upgrade, combined

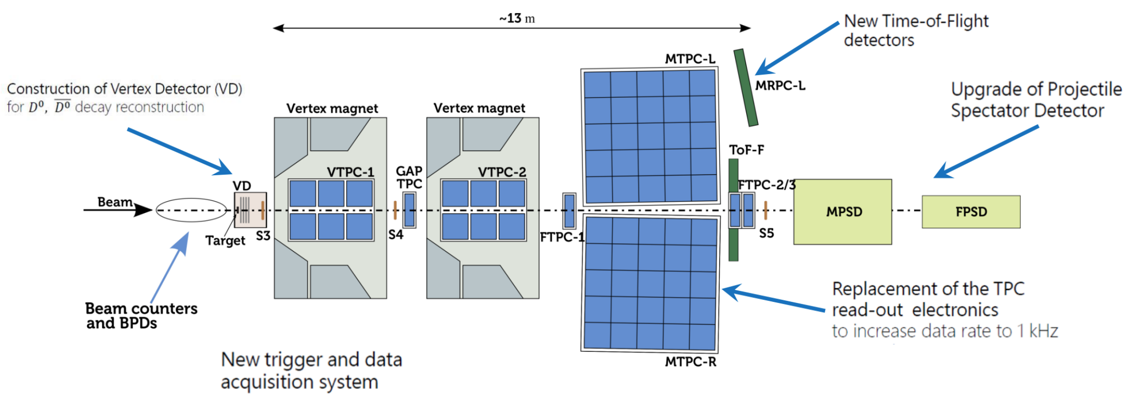

Figure B.1: A schematic view of the planned NA61/SHINE detector upgrades performed during CERN Long Shutdown 2.

with a new trigger and data acquisition system, will allow a tenfold increase of the data taking rate, up to 1 kHz. An upgraded PSD will withstand high Pb beam intensities, necessary to saturate the whole system. Finally, a new ToF detector, based on mRPC technology, will replace the TOF-L/R walls. The new ToF detector will allow identification of charged kaons in mid-rapidity, allowing for a possible continuation of hadron production measurements and studies of the onset of deconfinement. For the moment, construction of only one left wall is planned. More information about the upgrade can be found in refs. [98–100].

Appendix C

Tabulated results

This appendix contains numerical results of the double differential spectra of K^+, K^-, p, $\bar{p}$, π^+ and π^- produced in central Ar+Sc collisions at 13A, 19A, 30A, 40A, 75A and 150A GeV/c beam momenta. The values in the table cells stand for:

$$\frac{d^2n}{dy dp_T} \pm \sigma_{stat} \pm \sigma_{sys} \; [(\text{GeV}/c)^{-1}], \qquad (C.1)$$

where $d^2n/dy dp_T$ is the mean number of particles produced in a single event per unit volume of the $y - p_T$ space, σ_{stat} and σ_{sys} denote statistical and systematic uncertainties, respectively.

C.1 K^+ spectra

p_T [GeV/c]	$-0.8 < y < -0.6$	$-0.6 < y < -0.4$	y $-0.4 < y < -0.2$	$-0.2 < y < 0.0$	$0.0 < y < 0.2$
0.05	0.439 ± 0.271 ± 0.241	0.291 ± 0.084 ± 0.026	0.720 ± 0.097 ± 0.070	0.813 ± 0.125 ± 0.094	-
0.15	-	0.676 ± 0.402 ± 0.713	1.759 ± 0.243 ± 0.555	2.150 ± 0.180 ± 0.069	1.739 ± 0.136 ± 0.119
0.25	-	-	-	2.881 ± 0.265 ± 0.121	2.560 ± 0.173 ± 0.208
0.35	-	-	-	-	2.980 ± 0.201 ± 0.126

p_T [GeV/c]	$0.2 < y < 0.4$	y $0.4 < y < 0.6$	$0.6 < y < 0.8$
0.05	-	-	-
0.15	-	-	-
0.25	2.898 ± 0.156 ± 0.074	-	-
0.35	2.640 ± 0.148 ± 0.298	2.743 ± 0.166 ± 0.117	-
0.45	2.635 ± 0.162 ± 0.123	2.302 ± 0.121 ± 0.120	-
0.55	2.234 ± 0.154 ± 0.160	1.815 ± 0.111 ± 0.215	1.577 ± 0.172 ± 0.563
0.65	1.633 ± 0.128 ± 0.112	1.536 ± 0.109 ± 0.065	1.077 ± 0.109 ± 0.045
0.75	1.433 ± 0.140 ± 0.091	1.048 ± 0.097 ± 0.195	0.815 ± 0.085 ± 0.059
0.85	0.966 ± 0.123 ± 0.091	0.750 ± 0.083 ± 0.089	0.854 ± 0.098 ± 0.069
0.95	0.610 ± 0.100 ± 0.108	0.363 ± 0.046 ± 0.041	0.521 ± 0.077 ± 0.029
1.05	0.432 ± 0.083 ± 0.019	0.447 ± 0.076 ± 0.112	0.381 ± 0.076 ± 0.069
1.15	-	0.254 ± 0.051 ± 0.035	0.174 ± 0.039 ± 0.054

Table C.1: Numerical values of $\frac{d^2n}{dy dp_T}$ spectra of K^+ produced in Ar+Sc collisions at 13A GeV/c

p_T [GeV/c]	y: $-0.8 < y < -0.6$	$-0.6 < y < -0.4$	$-0.4 < y < -0.2$	$-0.2 < y < 0.0$	$0.0 < y < 0.2$	$0.2 < y < 0.4$	$0.4 < y < 0.6$
0.05	$0.774 \pm 0.309 \pm 0.269$	$0.717 \pm 0.109 \pm 0.079$	$0.846 \pm 0.078 \pm 0.077$	$0.754 \pm 0.069 \pm 0.031$	-	-	-
0.15	-	$1.218 \pm 0.415 \pm 0.397$	$2.095 \pm 0.206 \pm 0.081$	$2.322 \pm 0.156 \pm 0.119$	$2.356 \pm 0.131 \pm 0.105$	-	-
0.25	-	-	$3.708 \pm 0.602 \pm 0.388$	$3.964 \pm 0.272 \pm 0.163$	$3.133 \pm 0.170 \pm 0.109$	$2.960 \pm 0.154 \pm 0.074$	-
0.35	-	-	-	$3.930 \pm 0.334 \pm 0.080$	$3.942 \pm 0.225 \pm 0.149$	$3.425 \pm 0.155 \pm 0.073$	$3.110 \pm 0.289 \pm 0.200$
0.45	-	-	-	$4.233 \pm 0.611 \pm 0.349$	$3.350 \pm 0.203 \pm 0.134$	$2.937 \pm 0.152 \pm 0.132$	$2.866 \pm 0.183 \pm 0.043$
0.55	-	-	-	-	$2.772 \pm 0.202 \pm 0.129$	$2.509 \pm 0.153 \pm 0.106$	$2.302 \pm 0.134 \pm 0.082$
0.65	-	-	-	-	$2.956 \pm 0.270 \pm 0.094$	$2.056 \pm 0.147 \pm 0.076$	$1.977 \pm 0.128 \pm 0.050$
0.75	-	-	-	-	$1.793 \pm 0.208 \pm 0.080$	$2.050 \pm 0.177 \pm 0.154$	$1.368 \pm 0.100 \pm 0.030$
0.85	-	-	-	-	$1.950 \pm 0.317 \pm 0.056$	$1.233 \pm 0.120 \pm 0.087$	$1.313 \pm 0.121 \pm 0.049$
0.95	-	-	-	-	$0.706 \pm 0.130 \pm 0.091$	$0.739 \pm 0.088 \pm 0.099$	$0.901 \pm 0.108 \pm 0.031$
1.05	-	-	-	-	$0.487 \pm 0.120 \pm 0.069$	$0.665 \pm 0.102 \pm 0.030$	$0.493 \pm 0.068 \pm 0.039$
1.15	-	-	-	-	$1.089 \pm 0.445 \pm 0.120$	$0.436 \pm 0.079 \pm 0.027$	$0.378 \pm 0.062 \pm 0.023$
1.25	-	-	-	-	$0.441 \pm 0.187 \pm 0.044$	$0.417 \pm 0.111 \pm 0.036$	$0.221 \pm 0.048 \pm 0.020$
1.35	-	-	-	-	$0.227 \pm 0.113 \pm 0.050$	$0.168 \pm 0.050 \pm 0.012$	$0.146 \pm 0.038 \pm 0.015$

Table C.2: Numerical values of $\frac{d^2n}{dy dp_T}$ spectra of K^+ produced in Ar+Sc collisions at $19A$ GeV/c

p_T [GeV/c]	y: $-0.6 < y < -0.4$	$-0.4 < y < -0.2$	$-0.2 < y < 0.0$	$0.0 < y < 0.2$	$0.2 < y < 0.4$	$0.4 < y < 0.6$
0.05	$0.899 \pm 0.066 \pm 0.027$	$1.016 \pm 0.047 \pm 0.027$	$0.986 \pm 0.036 \pm 0.029$	-	-	-
0.15	$3.132 \pm 0.497 \pm 0.624$	$2.713 \pm 0.132 \pm 0.059$	$2.672 \pm 0.096 \pm 0.076$	$2.975 \pm 0.082 \pm 0.060$	-	-
0.25	-	$3.999 \pm 0.261 \pm 0.245$	$3.863 \pm 0.145 \pm 0.094$	$4.062 \pm 0.116 \pm 0.093$	$3.925 \pm 0.126 \pm 0.072$	-
0.35	-	-	$4.400 \pm 0.173 \pm 0.065$	$3.997 \pm 0.130 \pm 0.115$	$4.280 \pm 0.112 \pm 0.119$	-
0.45	-	-	$4.189 \pm 0.190 \pm 0.128$	$4.106 \pm 0.146 \pm 0.070$	$3.874 \pm 0.109 \pm 0.069$	-
0.55	-	-	$3.826 \pm 0.220 \pm 0.126$	$3.374 \pm 0.136 \pm 0.085$	$3.380 \pm 0.112 \pm 0.098$	$3.381 \pm 0.209 \pm 0.136$
0.65	-	-	$3.392 \pm 0.245 \pm 0.171$	$2.851 \pm 0.130 \pm 0.069$	$2.714 \pm 0.101 \pm 0.074$	$2.433 \pm 0.153 \pm 0.093$
0.75	-	-	$2.630 \pm 0.229 \pm 0.093$	$2.302 \pm 0.121 \pm 0.057$	$1.986 \pm 0.089 \pm 0.070$	$1.983 \pm 0.144 \pm 0.053$
0.85	-	-	$1.827 \pm 0.205 \pm 0.094$	$1.655 \pm 0.099 \pm 0.017$	$1.791 \pm 0.096 \pm 0.061$	$1.341 \pm 0.112 \pm 0.084$
0.95	-	-	$1.224 \pm 0.184 \pm 0.111$	$1.275 \pm 0.095 \pm 0.044$	$1.146 \pm 0.073 \pm 0.051$	$1.051 \pm 0.109 \pm 0.050$
1.05	-	-	$0.939 \pm 0.153 \pm 0.048$	$0.850 \pm 0.071 \pm 0.045$	$0.930 \pm 0.074 \pm 0.034$	$0.856 \pm 0.115 \pm 0.063$
1.15	-	-	-	$0.574 \pm 0.060 \pm 0.036$	$0.657 \pm 0.064 \pm 0.043$	
1.25	-	-	-	$0.403 \pm 0.046 \pm 0.023$	$0.445 \pm 0.055 \pm 0.032$	
1.35	-	-	-	$0.331 \pm 0.057 \pm 0.023$	$0.335 \pm 0.051 \pm 0.027$	

Table C.3: Numerical values of $\frac{d^2n}{dy dp_T}$ spectra of K^+ produced in Ar+Sc collisions at $30A$ GeV/c

p_T [GeV/c]	y: $-0.6<y<-0.4$	$-0.4<y<-0.2$	$-0.2<y<0.0$	$0.0<y<0.2$	$0.2<y<0.4$
0.05	1.196 ± 0.101 ± 0.099	1.126 ± 0.046 ± 0.044	1.153 ± 0.035 ± 0.023	1.197 ± 0.043 ± 0.033	-
0.15	-	3.107 ± 0.139 ± 0.117	3.249 ± 0.100 ± 0.094	3.179 ± 0.073 ± 0.073	3.263 ± 0.145 ± 0.157
0.25	-	3.981 ± 0.249 ± 0.221	4.536 ± 0.150 ± 0.086	4.341 ± 0.114 ± 0.185	4.320 ± 0.112 ± 0.116
0.35	-	4.242 ± 0.421 ± 0.768	4.622 ± 0.171 ± 0.062	4.774 ± 0.140 ± 0.120	4.874 ± 0.119 ± 0.113
0.45	-	-	4.566 ± 0.184 ± 0.262	4.437 ± 0.151 ± 0.123	4.545 ± 0.120 ± 0.179
0.55	-	-	4.065 ± 0.189 ± 0.087	3.711 ± 0.147 ± 0.061	4.014 ± 0.122 ± 0.082
0.65	-	-	3.276 ± 0.182 ± 0.102	2.959 ± 0.131 ± 0.069	3.243 ± 0.115 ± 0.120
0.75	-	-	2.840 ± 0.192 ± 0.073	2.626 ± 0.143 ± 0.110	2.502 ± 0.104 ± 0.152
0.85	-	-	2.070 ± 0.162 ± 0.119	1.903 ± 0.118 ± 0.093	1.872 ± 0.098 ± 0.092
0.95	-	-	1.623 ± 0.152 ± 0.059	1.261 ± 0.091 ± 0.045	1.183 ± 0.071 ± 0.068
1.05	-	-	1.096 ± 0.120 ± 0.037	1.104 ± 0.102 ± 0.084	1.012 ± 0.083 ± 0.077
1.15	-	-	0.667 ± 0.088 ± 0.077	0.626 ± 0.065 ± 0.046	0.607 ± 0.058 ± 0.079
1.25	-	-	0.592 ± 0.104 ± 0.085	0.492 ± 0.064 ± 0.023	0.431 ± 0.056 ± 0.040
1.35	-	-	0.385 ± 0.094 ± 0.021	0.364 ± 0.060 ± 0.021	0.262 ± 0.046 ± 0.024
1.45	-	-	0.289 ± 0.070 ± 0.073	0.142 ± 0.026 ± 0.022	0.215 ± 0.046 ± 0.030

Table C.4: Numerical values of $\frac{d^2n}{dy dp_T}$ spectra of K^+ produced in Ar+Sc collisions at 40A GeV/c

p_T [GeV/c]	y: $-0.4<y<-0.2$	$-0.2<y<0.0$	$0.0<y<0.2$	$0.2<y<0.4$	$0.4<y<0.6$
0.05	-	1.347 ± 0.026 ± 0.047	1.387 ± 0.023 ± 0.039	1.344 ± 0.020 ± 0.041	-
0.15	-	3.783 ± 0.075 ± 0.121	3.492 ± 0.047 ± 0.104	3.832 ± 0.037 ± 0.103	3.904 ± 0.068 ± 0.083
0.25	-	5.225 ± 0.117 ± 0.170	5.218 ± 0.077 ± 0.161	5.254 ± 0.060 ± 0.119	5.369 ± 0.077 ± 0.086
0.35	-	5.544 ± 0.132 ± 0.147	5.737 ± 0.092 ± 0.144	5.670 ± 0.072 ± 0.101	5.614 ± 0.088 ± 0.074
0.45	-	5.367 ± 0.131 ± 0.121	5.605 ± 0.097 ± 0.100	5.492 ± 0.076 ± 0.078	5.773 ± 0.111 ± 0.080
0.55	-	4.731 ± 0.119 ± 0.079	4.778 ± 0.093 ± 0.091	4.712 ± 0.072 ± 0.069	4.819 ± 0.133 ± 0.120
0.65	-	4.044 ± 0.107 ± 0.041	3.838 ± 0.086 ± 0.060	3.786 ± 0.065 ± 0.077	-
0.75	-	3.160 ± 0.096 ± 0.028	3.103 ± 0.080 ± 0.053	3.136 ± 0.064 ± 0.111	-
0.85	2.020 ± 0.146 ± 0.059	2.327 ± 0.080 ± 0.033	2.110 ± 0.063 ± 0.068	2.161 ± 0.058 ± 0.095	-
0.95	1.651 ± 0.123 ± 0.027	1.645 ± 0.065 ± 0.034	1.491 ± 0.052 ± 0.052	1.481 ± 0.051 ± 0.079	-
1.05	1.304 ± 0.097 ± 0.025	1.233 ± 0.058 ± 0.048	1.164 ± 0.046 ± 0.059	1.093 ± 0.052 ± 0.061	-
1.15	0.646 ± 0.064 ± 0.023	0.821 ± 0.045 ± 0.047	0.822 ± 0.040 ± 0.048	-	-
1.25	0.545 ± 0.049 ± 0.022	0.589 ± 0.040 ± 0.040	0.452 ± 0.028 ± 0.029	-	-
1.35	0.341 ± 0.051 ± 0.030	0.383 ± 0.030 ± 0.021	0.458 ± 0.046 ± 0.026	-	-

Table C.5: Numerical values of $\frac{d^2n}{dy dp_T}$ spectra of K^+ produced in Ar+Sc collisions at 75A GeV/c

p_T [GeV/c]	y: $-0.4<y<-0.2$	$-0.2<y<0.0$	$0.0<y<0.2$	$0.2<y<0.4$	$0.4<y<0.6$
0.05	-	-	1.514 ± 0.051 ± 0.170	1.429 ± 0.031 ± 0.088	1.482 ± 0.028 ± 0.045
0.15	-	-	4.288 ± 0.100 ± 0.361	3.991 ± 0.050 ± 0.209	3.902 ± 0.047 ± 0.103
0.25	-	-	5.882 ± 0.144 ± 0.377	5.782 ± 0.076 ± 0.215	5.391 ± 0.056 ± 0.101
0.35	-	-	6.441 ± 0.146 ± 0.336	6.180 ± 0.094 ± 0.184	5.909 ± 0.071 ± 0.077
0.45	-	-	6.151 ± 0.136 ± 0.220	6.066 ± 0.105 ± 0.146	5.453 ± 0.102 ± 0.083
0.55	-	5.331 ± 0.258 ± 0.301	5.490 ± 0.131 ± 0.142	5.094 ± 0.102 ± 0.126	-
0.65	-	4.972 ± 0.202 ± 0.139	4.428 ± 0.117 ± 0.099	4.138 ± 0.132 ± 0.155	-
0.75	-	3.529 ± 0.134 ± 0.144	3.541 ± 0.107 ± 0.109	-	-
0.85	-	2.467 ± 0.104 ± 0.067	2.366 ± 0.104 ± 0.077	-	-
0.95	1.950 ± 0.176 ± 0.076	1.754 ± 0.083 ± 0.071	-	-	-
1.05	1.255 ± 0.146 ± 0.100	1.444 ± 0.092 ± 0.068	-	-	-
1.15	0.958 ± 0.087 ± 0.038	0.932 ± 0.099 ± 0.047	-	-	-

p_T [GeV/c]	y: $0.6<y<0.8$
0.05	1.344 ± 0.032 ± 0.028
0.15	3.839 ± 0.060 ± 0.084
0.25	5.106 ± 0.081 ± 0.092

Table C.6: Numerical values of $\frac{d^2n}{dy dp_T}$ spectra of K^+ produced in Ar+Sc collisions at 150A GeV/c

C.2 K^- spectra

p_T [GeV/c]	y: $-0.6 < y < -0.4$	$-0.4 < y < -0.2$	$-0.2 < y < 0.0$	$0.0 < y < 0.2$	$0.2 < y < 0.4$	$0.4 < y < 0.6$
0.05	$0.103 \pm 0.045 \pm 0.102$	$0.184 \pm 0.046 \pm 0.041$	$0.248 \pm 0.059 \pm 0.047$	-	-	-
0.15	-	$0.399 \pm 0.104 \pm 0.032$	$0.518 \pm 0.077 \pm 0.122$	$0.591 \pm 0.072 \pm 0.037$	-	-
0.25	-	-	$0.777 \pm 0.135 \pm 0.105$	$0.727 \pm 0.082 \pm 0.047$	$0.745 \pm 0.074 \pm 0.031$	-
0.35	-	-	-	$0.788 \pm 0.100 \pm 0.056$	$0.580 \pm 0.060 \pm 0.136$	$0.708 \pm 0.076 \pm 0.153$
0.45	-	-	-	$0.633 \pm 0.111 \pm 0.038$	$0.696 \pm 0.072 \pm 0.116$	$0.468 \pm 0.048 \pm 0.034$
0.55	-	-	-	-	$0.474 \pm 0.059 \pm 0.044$	$0.397 \pm 0.045 \pm 0.030$
0.65	-	-	-	-	$0.461 \pm 0.064 \pm 0.042$	$0.329 \pm 0.042 \pm 0.135$
0.75	-	-	-	-	$0.312 \pm 0.058 \pm 0.083$	$0.171 \pm 0.028 \pm 0.031$

Table C.7: Numerical values of $\frac{d^2n}{dydp_T}$ spectra of K^- produced in Ar+Sc collisions at $13A$ GeV/c

p_T [GeV/c]	y: $-0.8 < y < -0.6$	$-0.6 < y < -0.4$	$-0.4 < y < -0.2$	$-0.2 < y < 0.0$	$0.0 < y < 0.2$	$0.2 < y < 0.4$	$0.4 < y < 0.6$
0.05	$0.042 \pm 0.044 \pm 0.086$	$0.277 \pm 0.064 \pm 0.027$	$0.264 \pm 0.037 \pm 0.019$	$0.305 \pm 0.040 \pm 0.033$	-	-	-
0.15	-	$0.274 \pm 0.174 \pm 0.088$	$0.618 \pm 0.094 \pm 0.025$	$0.633 \pm 0.065 \pm 0.046$	$0.798 \pm 0.067 \pm 0.031$	-	-
0.25	-	-	$1.234 \pm 0.307 \pm 0.087$	$0.932 \pm 0.110 \pm 0.032$	$1.064 \pm 0.086 \pm 0.017$	$0.857 \pm 0.067 \pm 0.013$	-
0.35	-	-	-	$1.384 \pm 0.185 \pm 0.024$	$1.138 \pm 0.100 \pm 0.050$	$0.968 \pm 0.071 \pm 0.016$	$0.949 \pm 0.112 \pm 0.043$
0.45	-	-	-	-	$1.081 \pm 0.108 \pm 0.069$	$0.978 \pm 0.078 \pm 0.030$	$0.894 \pm 0.083 \pm 0.037$
0.55	-	-	-	-	$1.047 \pm 0.126 \pm 0.024$	$0.708 \pm 0.069 \pm 0.006$	$0.648 \pm 0.057 \pm 0.024$
0.65	-	-	-	-	$0.886 \pm 0.130 \pm 0.056$	$0.564 \pm 0.062 \pm 0.022$	$0.527 \pm 0.054 \pm 0.017$
0.75	-	-	-	-	$0.612 \pm 0.119 \pm 0.018$	$0.442 \pm 0.056 \pm 0.020$	$0.430 \pm 0.052 \pm 0.014$
0.85	-	-	-	-	$0.296 \pm 0.073 \pm 0.030$	$0.289 \pm 0.049 \pm 0.018$	$0.274 \pm 0.040 \pm 0.014$
0.95						$0.271 \pm 0.054 \pm 0.013$	$0.161 \pm 0.032 \pm 0.008$
1.05						$0.155 \pm 0.040 \pm 0.012$	$0.085 \pm 0.029 \pm 0.008$

Table C.8: Numerical values of $\frac{d^2n}{dydp_T}$ spectra of K^- produced in Ar+Sc collisions at $19A$ GeV/c

p_T [GeV/c]	y $-0.6 < y < -0.4$	$-0.4 < y < -0.2$	$-0.2 < y < 0.0$	$0.0 < y < 0.2$	$0.2 < y < 0.4$	$0.4 < y < 0.6$
0.05	0.415 ± 0.043 ± 0.011	0.409 ± 0.027 ± 0.009	0.457 ± 0.023 ± 0.023	-	-	-
0.15	0.877 ± 0.219 ± 0.048	0.976 ± 0.068 ± 0.029	1.075 ± 0.053 ± 0.033	1.116 ± 0.044 ± 0.024	-	-
0.25	-	1.652 ± 0.148 ± 0.039	1.543 ± 0.082 ± 0.017	1.526 ± 0.061 ± 0.024	1.479 ± 0.064 ± 0.055	-
0.35	-	-	1.726 ± 0.097 ± 0.043	1.508 ± 0.069 ± 0.020	1.566 ± 0.058 ± 0.035	-
0.45	-	-	1.463 ± 0.095 ± 0.044	1.572 ± 0.080 ± 0.053	1.432 ± 0.060 ± 0.026	-
0.55	-	-	1.545 ± 0.121 ± 0.041	1.345 ± 0.074 ± 0.030	1.049 ± 0.050 ± 0.033	1.011 ± 0.077 ± 0.046
0.65	-	-	1.057 ± 0.108 ± 0.032	0.907 ± 0.059 ± 0.010	0.846 ± 0.047 ± 0.015	0.775 ± 0.063 ± 0.042
0.75	-	-	0.864 ± 0.115 ± 0.033	0.776 ± 0.059 ± 0.029	0.709 ± 0.045 ± 0.023	0.656 ± 0.064 ± 0.043
0.85	-	-	0.782 ± 0.132 ± 0.070	0.652 ± 0.058 ± 0.028	0.525 ± 0.041 ± 0.025	0.372 ± 0.044 ± 0.023
0.95	-	-	0.357 ± 0.080 ± 0.065	0.389 ± 0.042 ± 0.014	0.385 ± 0.035 ± 0.012	0.347 ± 0.051 ± 0.019
1.05	-	-	-	0.320 ± 0.051 ± 0.010	0.225 ± 0.027 ± 0.011	

Table C.9: Numerical values of $\frac{d^2n}{dydp_T}$ spectra of K^- produced in Ar+Sc collisions at 30A GeV/c

p_T [GeV/c]	y $-0.6 < y < -0.4$	$-0.4 < y < -0.2$	$-0.2 < y < 0.0$	$0.0 < y < 0.2$	$0.2 < y < 0.4$
0.05	0.524 ± 0.064 ± 0.049	0.544 ± 0.032 ± 0.039	0.509 ± 0.021 ± 0.007	0.516 ± 0.024 ± 0.028	-
0.15	-	1.414 ± 0.090 ± 0.023	1.442 ± 0.061 ± 0.037	1.350 ± 0.043 ± 0.037	1.320 ± 0.070 ± 0.050
0.25	-	2.076 ± 0.182 ± 0.079	1.918 ± 0.089 ± 0.060	1.844 ± 0.068 ± 0.049	1.948 ± 0.067 ± 0.127
0.35	-	1.899 ± 0.243 ± 0.174	2.132 ± 0.109 ± 0.056	2.137 ± 0.086 ± 0.079	1.923 ± 0.063 ± 0.045
0.45	-	-	1.966 ± 0.110 ± 0.081	2.075 ± 0.094 ± 0.046	1.800 ± 0.066 ± 0.055
0.55	-	-	1.747 ± 0.112 ± 0.081	1.737 ± 0.090 ± 0.045	1.390 ± 0.059 ± 0.037
0.65	-	-	1.376 ± 0.102 ± 0.048	1.261 ± 0.073 ± 0.037	1.205 ± 0.060 ± 0.073
0.75	-	-	1.324 ± 0.122 ± 0.031	1.012 ± 0.071 ± 0.023	0.904 ± 0.054 ± 0.028
0.85	-	-	0.962 ± 0.127 ± 0.070	0.726 ± 0.060 ± 0.011	0.634 ± 0.046 ± 0.026
0.95	-	-	0.538 ± 0.071 ± 0.048	0.438 ± 0.041 ± 0.043	0.441 ± 0.038 ± 0.048
1.05	-	-	0.295 ± 0.062 ± 0.056	0.522 ± 0.072 ± 0.036	0.360 ± 0.041 ± 0.030
1.15	-	-	0.335 ± 0.070 ± 0.059	0.180 ± 0.026 ± 0.044	0.295 ± 0.058 ± 0.013

Table C.10: Numerical values of $\frac{d^2n}{dydp_T}$ spectra of K^- produced in Ar+Sc collisions at 40A GeV/c

p_T [GeV/c]	y $-0.4 < y < -0.2$	$-0.2 < y < 0.0$	$0.0 < y < 0.2$	$0.2 < y < 0.4$	$0.4 < y < 0.6$
0.05	-	0.777 ± 0.021 ± 0.021	0.718 ± 0.015 ± 0.018	0.750 ± 0.014 ± 0.022	-
0.15	-	2.153 ± 0.060 ± 0.068	1.882 ± 0.032 ± 0.041	1.882 ± 0.024 ± 0.051	2.073 ± 0.043 ± 0.062
0.25	-	3.072 ± 0.095 ± 0.073	2.795 ± 0.056 ± 0.077	2.654 ± 0.039 ± 0.075	2.762 ± 0.049 ± 0.080
0.35	-	3.102 ± 0.103 ± 0.055	3.034 ± 0.064 ± 0.066	2.740 ± 0.045 ± 0.076	3.072 ± 0.059 ± 0.096
0.45	-	2.825 ± 0.096 ± 0.047	2.683 ± 0.062 ± 0.060	2.560 ± 0.047 ± 0.071	2.663 ± 0.064 ± 0.070
0.55	-	2.583 ± 0.090 ± 0.047	2.368 ± 0.060 ± 0.059	2.265 ± 0.047 ± 0.058	2.481 ± 0.080 ± 0.072
0.65	-	2.061 ± 0.074 ± 0.049	1.937 ± 0.056 ± 0.045	1.690 ± 0.041 ± 0.043	-
0.75	-	1.482 ± 0.064 ± 0.027	1.337 ± 0.045 ± 0.036	1.384 ± 0.039 ± 0.035	-
0.85	-	1.127 ± 0.055 ± 0.030	1.002 ± 0.039 ± 0.024	1.152 ± 0.042 ± 0.028	-
0.95	0.937 ± 0.095 ± 0.044	0.832 ± 0.048 ± 0.016	0.700 ± 0.032 ± 0.018	0.843 ± 0.038 ± 0.015	-
1.05	0.544 ± 0.059 ± 0.027	0.554 ± 0.037 ± 0.013	0.517 ± 0.028 ± 0.011	0.538 ± 0.035 ± 0.016	-
1.15	0.492 ± 0.068 ± 0.015	0.361 ± 0.028 ± 0.014	0.352 ± 0.023 ± 0.014	-	-

Table C.11: Numerical values of $\frac{d^2n}{dydp_T}$ spectra of K^- produced in Ar+Sc collisions at 75A GeV/c

p_T [GeV/c]	y: $-0.4 < y < -0.2$	$-0.2 < y < 0.0$	$0.0 < y < 0.2$	$0.2 < y < 0.4$	$0.4 < y < 0.6$
0.05	-	-	$1.079 \pm 0.045 \pm 0.099$	$0.927 \pm 0.024 \pm 0.053$	$0.943 \pm 0.021 \pm 0.050$
0.15	-	-	$2.791 \pm 0.079 \pm 0.201$	$2.513 \pm 0.037 \pm 0.141$	$2.423 \pm 0.033 \pm 0.135$
0.25	-	-	$4.083 \pm 0.122 \pm 0.256$	$3.432 \pm 0.054 \pm 0.184$	$3.162 \pm 0.038 \pm 0.144$
0.35	-	-	$4.003 \pm 0.113 \pm 0.213$	$3.606 \pm 0.066 \pm 0.164$	$3.411 \pm 0.047 \pm 0.145$
0.45	-	-	$3.833 \pm 0.102 \pm 0.147$	$3.424 \pm 0.069 \pm 0.139$	$3.254 \pm 0.072 \pm 0.106$
0.55	-	$3.594 \pm 0.227 \pm 0.136$	$3.342 \pm 0.095 \pm 0.129$	$2.654 \pm 0.061 \pm 0.079$	-
0.65	-	$2.592 \pm 0.127 \pm 0.084$	$2.512 \pm 0.080 \pm 0.078$	$2.430 \pm 0.084 \pm 0.078$	-
0.75	-	$1.763 \pm 0.085 \pm 0.061$	$1.838 \pm 0.067 \pm 0.049$	-	-
0.85	-	$1.459 \pm 0.072 \pm 0.064$	$1.641 \pm 0.088 \pm 0.031$	-	-
0.95	$0.942 \pm 0.115 \pm 0.068$	$1.034 \pm 0.062 \pm 0.026$	-	-	-
1.05	$0.735 \pm 0.113 \pm 0.026$	$0.776 \pm 0.060 \pm 0.014$	-	-	-

p_T [GeV/c]	y: $0.6 < y < 0.8$
0.05	$0.813 \pm 0.020 \pm 0.051$
0.15	$2.306 \pm 0.039 \pm 0.119$
0.25	$3.207 \pm 0.060 \pm 0.143$

Table C.12: Numerical values of $\frac{d^2n}{dy dp_T}$ spectra of K^- produced in Ar+Sc collisions at 150A GeV/c

C.3 π^+ spectra

p_T [GeV/c]	y: $0.4 < y < 0.6$	$0.6 < y < 0.8$	$0.8 < y < 1.0$	$1.0 < y < 1.2$
0.05	$12.180 \pm 0.214 \pm 0.589$	$13.515 \pm 0.179 \pm 0.338$	$13.469 \pm 0.170 \pm 0.391$	$12.016 \pm 0.433 \pm 0.459$
0.15	$31.024 \pm 0.509 \pm 2.154$	$24.800 \pm 0.329 \pm 1.007$	$26.490 \pm 0.286 \pm 0.726$	$24.538 \pm 0.426 \pm 0.855$
0.25	$32.099 \pm 0.515 \pm 1.121$	$24.394 \pm 0.334 \pm 0.776$	$21.780 \pm 0.261 \pm 0.173$	$18.823 \pm 0.575 \pm 0.642$
0.35	$22.409 \pm 0.389 \pm 0.554$	$17.007 \pm 0.274 \pm 0.464$	$15.313 \pm 0.228 \pm 0.182$	-
0.45	$15.142 \pm 0.301 \pm 0.059$	$11.273 \pm 0.219 \pm 0.192$	$9.500 \pm 0.197 \pm 0.066$	-
0.55	$9.759 \pm 0.234 \pm 0.537$	$7.358 \pm 0.177 \pm 0.142$	$5.913 \pm 0.173 \pm 0.035$	-
0.65	$5.879 \pm 0.176 \pm 0.036$	$4.630 \pm 0.139 \pm 0.130$	$3.315 \pm 0.142 \pm 0.144$	-
0.75	$4.060 \pm 0.153 \pm 0.189$	$3.100 \pm 0.117 \pm 0.085$	$2.256 \pm 0.136 \pm 0.120$	-
0.85	$2.307 \pm 0.113 \pm 0.199$	$1.794 \pm 0.089 \pm 0.051$	$1.137 \pm 0.097 \pm 0.203$	-
0.95	$1.426 \pm 0.090 \pm 0.030$	$1.096 \pm 0.071 \pm 0.115$	-	-
1.05	$0.943 \pm 0.078 \pm 0.055$	$0.608 \pm 0.053 \pm 0.045$	-	-
1.15	$0.474 \pm 0.054 \pm 0.006$	$0.326 \pm 0.038 \pm 0.043$	-	-

Table C.13: Numerical values of $\frac{d^2n}{dy dp_T}$ spectra of π^+ produced in Ar+Sc collisions at 13A GeV/c

p_T [GeV/c]	y: $0.2 < y < 0.4$	$0.4 < y < 0.6$	$0.6 < y < 0.8$	$0.8 < y < 1.0$	$1.0 < y < 1.2$
0.05	-	$16.516 \pm 0.298 \pm 1.172$	$15.727 \pm 0.195 \pm 0.829$	$14.118 \pm 0.148 \pm 0.729$	$12.590 \pm 0.212 \pm 0.753$
0.15	-	$33.761 \pm 0.522 \pm 1.853$	$30.871 \pm 0.360 \pm 0.784$	$29.149 \pm 0.287 \pm 0.931$	$26.554 \pm 0.391 \pm 0.830$
0.25	$36.732 \pm 1.543 \pm 5.882$	$31.675 \pm 0.421 \pm 0.824$	$27.304 \pm 0.338 \pm 0.840$	$25.878 \pm 0.281 \pm 0.693$	-
0.35	$31.365 \pm 0.805 \pm 1.433$	$23.206 \pm 0.340 \pm 0.518$	$20.331 \pm 0.282 \pm 0.594$	$17.381 \pm 0.291 \pm 0.387$	-
0.45	$20.863 \pm 0.526 \pm 0.547$	$16.214 \pm 0.287 \pm 0.411$	$14.378 \pm 0.233 \pm 0.307$	$11.357 \pm 0.343 \pm 0.369$	-
0.55	$13.490 \pm 0.366 \pm 0.230$	$10.351 \pm 0.227 \pm 0.280$	$9.495 \pm 0.189 \pm 0.210$	-	-
0.65	$8.325 \pm 0.265 \pm 0.041$	$7.162 \pm 0.195 \pm 0.192$	$6.170 \pm 0.163 \pm 0.086$	-	-
0.75	$6.060 \pm 0.227 \pm 0.101$	$4.618 \pm 0.158 \pm 0.137$	$3.667 \pm 0.134 \pm 0.046$	-	-
0.85	$3.855 \pm 0.178 \pm 0.034$	$3.056 \pm 0.132 \pm 0.108$	$2.417 \pm 0.126 \pm 0.108$	-	-
0.95	$2.311 \pm 0.133 \pm 0.046$	$1.875 \pm 0.106 \pm 0.067$	$1.799 \pm 0.128 \pm 0.056$	-	-
1.05	$1.590 \pm 0.112 \pm 0.030$	$1.245 \pm 0.087 \pm 0.052$	$1.059 \pm 0.109 \pm 0.024$	-	-
1.15	$0.938 \pm 0.083 \pm 0.033$	$0.734 \pm 0.068 \pm 0.037$	$0.531 \pm 0.070 \pm 0.009$	-	-
1.25	$0.700 \pm 0.092 \pm 0.096$	$0.369 \pm 0.043 \pm 0.031$	$0.330 \pm 0.064 \pm 0.003$	-	-
1.35	$0.389 \pm 0.060 \pm 0.017$	$0.283 \pm 0.042 \pm 0.034$	-	-	-

Table C.14: Numerical values of $\frac{d^2n}{dy dp_T}$ spectra of π^+ produced in Ar+Sc collisions at 19A GeV/c

p_T [GeV/c]	y $0.0<y<0.2$	$0.2<y<0.4$	$0.4<y<0.6$	$0.6<y<0.8$	$0.8<y<1.0$	$1.0<y<1.2$
0.05	-	-	23.037 ± 0.502 ± 9.515	18.970 ± 0.141 ± 0.788	16.799 ± 0.108 ± 0.731	14.868 ± 0.092 ± 0.660
0.15	-	-	38.389 ± 0.387 ± 2.365	37.916 ± 0.260 ± 0.822	34.812 ± 0.207 ± 1.166	32.672 ± 0.244 ± 0.977
0.25	-	38.178 ± 0.637 ± 3.463	36.604 ± 0.303 ± 0.659	34.893 ± 0.253 ± 0.982	31.629 ± 0.216 ± 0.789	
0.35	-	29.514 ± 0.334 ± 1.003	26.809 ± 0.250 ± 0.730	25.155 ± 0.203 ± 0.594	22.783 ± 0.315 ± 0.655	
0.45	30.782 ± 1.034 ± 2.761	21.251 ± 0.251 ± 0.440	18.707 ± 0.207 ± 0.458	17.615 ± 0.182 ± 0.386	-	
0.55	19.237 ± 0.483 ± 0.559	13.822 ± 0.196 ± 0.190	12.853 ± 0.170 ± 0.290	11.855 ± 0.191 ± 0.270	-	
0.65	12.332 ± 0.318 ± 0.207	9.854 ± 0.171 ± 0.200	8.537 ± 0.137 ± 0.174	7.366 ± 0.199 ± 0.242	-	
0.75	7.961 ± 0.225 ± 0.108	6.414 ± 0.140 ± 0.109	5.788 ± 0.114 ± 0.116	-	-	
0.85	4.865 ± 0.161 ± 0.115	4.244 ± 0.117 ± 0.091	3.786 ± 0.095 ± 0.058	-	-	
0.95	3.099 ± 0.126 ± 0.046	2.681 ± 0.092 ± 0.051	2.659 ± 0.088 ± 0.040	-	-	
1.05	1.913 ± 0.091 ± 0.045	1.696 ± 0.071 ± 0.038	1.607 ± 0.074 ± 0.040	-	-	
1.15	1.345 ± 0.091 ± 0.036	1.158 ± 0.060 ± 0.034	1.034 ± 0.064 ± 0.032	-	-	
1.25	0.802 ± 0.059 ± 0.012	0.743 ± 0.049 ± 0.018	-	-	-	
1.35	0.450 ± 0.052 ± 0.025	0.498 ± 0.040 ± 0.017	-	-	-	

Table C.15: Numerical values of $\frac{d^2n}{dydp_T}$ spectra of π^+ produced in Ar+Sc collisions at 30A GeV/c

p_T [GeV/c]	y $-0.2<y<0.0$	$0.0<y<0.2$	$0.2<y<0.4$	$0.4<y<0.6$	$0.6<y<0.8$	$0.8<y<1.0$	$1.0<y<1.2$	$1.2<y<1.4$
0.05	-	-	-	-	20.773 ± 0.191 ± 1.334	18.515 ± 0.116 ± 0.720	17.030 ± 0.091 ± 0.613	14.905 ± 0.145 ± 0.738
0.15	-	-	-	40.712 ± 0.518 ± 3.350	42.381 ± 0.281 ± 0.874	38.405 ± 0.224 ± 1.185	35.942 ± 0.202 ± 1.050	-
0.25	-	-	41.137 ± 0.747 ± 4.169	39.691 ± 0.309 ± 0.627	39.218 ± 0.266 ± 1.173	36.110 ± 0.220 ± 0.857	-	-
0.35	-	-	31.566 ± 0.333 ± 0.955	29.642 ± 0.257 ± 0.585	28.779 ± 0.211 ± 0.634	26.373 ± 0.332 ± 0.862	-	-
0.45	-	22.901 ± 0.502 ± 1.629	23.039 ± 0.260 ± 0.267	20.880 ± 0.214 ± 0.441	20.009 ± 0.198 ± 0.493			
0.55	-	16.367 ± 0.306 ± 0.519	15.106 ± 0.207 ± 0.263	14.608 ± 0.180 ± 0.251	13.189 ± 0.228 ± 0.363			
0.65	-	11.361 ± 0.225 ± 0.284	10.594 ± 0.185 ± 0.191	9.585 ± 0.141 ± 0.104	-			
0.75	-	7.579 ± 0.176 ± 0.148	6.853 ± 0.146 ± 0.109	6.377 ± 0.127 ± 0.135	-			
0.85	7.354 ± 0.549 ± 0.299	4.778 ± 0.134 ± 0.130	4.720 ± 0.126 ± 0.062	4.157 ± 0.120 ± 0.087	-			
0.95	4.238 ± 0.309 ± 0.072	3.134 ± 0.109 ± 0.062	3.055 ± 0.102 ± 0.063	2.964 ± 0.124 ± 0.123	-			
1.05	2.692 ± 0.210 ± 0.246	2.337 ± 0.106 ± 0.094	2.124 ± 0.086 ± 0.051	2.097 ± 0.133 ± 0.129	-			
1.15	1.598 ± 0.161 ± 0.103	1.430 ± 0.080 ± 0.030	1.289 ± 0.064 ± 0.026	1.261 ± 0.124 ± 0.043	-			
1.25	1.130 ± 0.122 ± 0.022	0.910 ± 0.064 ± 0.049	0.896 ± 0.056 ± 0.039	-	-			
1.35	0.659 ± 0.127 ± 0.054	0.502 ± 0.043 ± 0.022	0.480 ± 0.041 ± 0.008	-	-			
1.45	0.321 ± 0.046 ± 0.005	0.419 ± 0.046 ± 0.019	0.383 ± 0.041 ± 0.069	-	-			

Table C.16: Numerical values of $\frac{d^2n}{dydp_T}$ spectra of π^+ produced in Ar+Sc collisions at 40A GeV/c

p_T [GeV/c]	$-0.4 < y < -0.2$	$-0.2 < y < 0.0$	$0.0 < y < 0.2$	$0.2 < y < 0.4$	$0.4 < y < 0.6$
0.05	-	-	-	-	-
0.15	-	-	-	-	-
0.25	-	-	-	-	45.277 ± 0.354 ± 1.194
0.35	-	-	-	36.716 ± 0.382 ± 1.170	36.083 ± 0.195 ± 0.364
0.45	-	-	-	26.190 ± 0.195 ± 0.202	25.399 ± 0.162 ± 0.360
0.55	-	-	18.786 ± 0.232 ± 0.348	18.090 ± 0.154 ± 0.168	17.635 ± 0.130 ± 0.210
0.65	-	-	12.919 ± 0.152 ± 0.094	12.054 ± 0.126 ± 0.143	11.841 ± 0.101 ± 0.128
0.75	-	8.884 ± 0.225 ± 0.197	8.515 ± 0.119 ± 0.056	8.293 ± 0.103 ± 0.091	8.058 ± 0.094 ± 0.148
0.85	-	5.838 ± 0.138 ± 0.032	5.826 ± 0.099 ± 0.052	5.512 ± 0.082 ± 0.056	5.377 ± 0.103 ± 0.094
0.95	-	3.967 ± 0.098 ± 0.036	3.926 ± 0.083 ± 0.055	3.803 ± 0.066 ± 0.045	3.430 ± 0.120 ± 0.093
1.05	-	2.690 ± 0.075 ± 0.021	2.647 ± 0.069 ± 0.028	2.432 ± 0.054 ± 0.027	-
1.15	-	2.021 ± 0.070 ± 0.032	1.738 ± 0.054 ± 0.023	1.656 ± 0.059 ± 0.028	-
1.25	1.579 ± 0.119 ± 0.029	1.153 ± 0.048 ± 0.010	1.148 ± 0.044 ± 0.028	-	-
1.35	-	0.812 ± 0.042 ± 0.015	0.780 ± 0.043 ± 0.015	-	-

p_T [GeV/c]	$0.6 < y < 0.8$	$0.8 < y < 1.0$	$1.0 < y < 1.2$	$1.2 < y < 1.4$	$1.4 < y < 1.6$
0.05	-	-	20.312 ± 0.071 ± 0.497	18.294 ± 0.065 ± 0.245	16.146 ± 0.064 ± 0.300
0.15	44.191 ± 0.370 ± 1.442	45.597 ± 0.169 ± 0.940	41.446 ± 0.118 ± 0.516	38.287 ± 0.106 ± 0.535	-
0.25	46.494 ± 0.199 ± 0.692	41.526 ± 0.153 ± 0.509	39.335 ± 0.142 ± 0.466	-	-
0.35	34.469 ± 0.164 ± 0.483	31.559 ± 0.140 ± 0.349	-	-	-
0.45	24.162 ± 0.128 ± 0.246	-	-	-	-
0.55	16.931 ± 0.139 ± 0.272	-	-	-	-

Table C.17: Numerical values of $\frac{d^2n}{dydp_T}$ spectra of π^+ produced in Ar+Sc collisions at $75A$ GeV/c

p_T [GeV/c]	$-0.4 < y < -0.2$	$-0.2 < y < 0.0$	$0.0 < y < 0.2$	$0.2 < y < 0.4$	$0.4 < y < 0.6$
0.05	-	-	-	-	-
0.15	-	-	-	-	-
0.25	-	-	-	-	-
0.35	-	-	-	-	40.461 ± 0.461 ± 2.250
0.45	-	-	-	29.942 ± 0.510 ± 1.900	30.883 ± 0.244 ± 0.950
0.55	-	-	-	21.867 ± 0.241 ± 0.686	21.001 ± 0.193 ± 0.542
0.65	-	-	15.271 ± 0.288 ± 0.726	15.122 ± 0.187 ± 0.366	14.148 ± 0.207 ± 0.408
0.75	-	-	10.300 ± 0.181 ± 0.360	10.047 ± 0.161 ± 0.324	-
0.85	-	7.458 ± 0.263 ± 0.288	7.224 ± 0.146 ± 0.233	6.986 ± 0.234 ± 0.246	-
0.95	-	4.786 ± 0.151 ± 0.153	4.748 ± 0.134 ± 0.139	-	-
1.05	-	3.357 ± 0.125 ± 0.065	3.253 ± 0.193 ± 0.095	-	-
1.15	2.408 ± 0.208 ± 0.062	2.169 ± 0.104 ± 0.104	-	-	-

p_T [GeV/c]	$0.6 < y < 0.8$	$0.8 < y < 1.0$	$1.0 < y < 1.2$	$1.2 < y < 1.4$	$1.4 < y < 1.6$
0.05	-	-	-	21.406 ± 0.147 ± 1.736	19.419 ± 0.105 ± 0.834
0.15	-	-	47.763 ± 0.193 ± 2.568	45.418 ± 0.152 ± 1.517	40.588 ± 0.152 ± 0.678
0.25	52.432 ± 0.533 ± 3.232	49.200 ± 0.228 ± 2.155	46.106 ± 0.159 ± 0.923	41.956 ± 0.172 ± 0.639	37.979 ± 0.490 ± 0.704
0.35	40.963 ± 0.241 ± 1.351	37.044 ± 0.180 ± 0.799	34.041 ± 0.197 ± 0.639	-	-
0.45	28.554 ± 0.192 ± 0.661	26.028 ± 0.245 ± 0.468	-	-	-
0.55	19.560 ± 0.249 ± 0.391	-	-	-	-

p_T [GeV/c]	$1.6 < y < 1.8$	$1.8 < y < 2.0$
0.05	17.716 ± 0.094 ± 0.294	14.787 ± 0.123 ± 0.245
0.15	36.545 ± 0.265 ± 0.533	-

Table C.18: Numerical values of $\frac{d^2n}{dydp_T}$ spectra of π^+ produced in Ar+Sc collisions at $150A$ GeV/c

C.4 π^- spectra

p_T [GeV/c]	y: $0.4 < y < 0.6$	$0.6 < y < 0.8$	$0.8 < y < 1.0$	$1.0 < y < 1.2$
0.05	13.115 ± 0.180 ± 0.195	13.675 ± 0.140 ± 0.418	13.413 ± 0.135 ± 0.313	13.078 ± 0.311 ± 0.209
0.15	33.559 ± 0.473 ± 0.585	25.676 ± 0.284 ± 0.301	26.414 ± 0.243 ± 0.414	27.559 ± 0.365 ± 0.545
0.25	35.073 ± 0.494 ± 0.488	23.854 ± 0.281 ± 0.384	21.167 ± 0.230 ± 0.202	21.673 ± 0.455 ± 0.482
0.35	24.305 ± 0.380 ± 0.286	16.237 ± 0.224 ± 0.071	14.897 ± 0.202 ± 0.167	-
0.45	15.676 ± 0.283 ± 0.548	10.152 ± 0.175 ± 0.049	9.449 ± 0.173 ± 0.111	-
0.55	9.330 ± 0.206 ± 0.455	6.904 ± 0.144 ± 0.072	5.946 ± 0.151 ± 0.168	-
0.65	6.066 ± 0.164 ± 0.059	4.436 ± 0.117 ± 0.018	-	-
0.75	3.725 ± 0.130 ± 0.349	2.637 ± 0.090 ± 0.068	-	-

Table C.19: Numerical values of $\frac{d^2n}{dy dp_T}$ spectra of π^- produced in Ar+Sc collisions at 13A GeV/c

p_T [GeV/c]	y: $0.2 < y < 0.4$	$0.4 < y < 0.6$	$0.6 < y < 0.8$	$0.8 < y < 1.0$	$1.0 < y < 1.2$
0.05	-	17.717 ± 0.265 ± 1.185	16.428 ± 0.165 ± 0.665	14.111 ± 0.118 ± 0.593	12.671 ± 0.157 ± 0.662
0.15	-	34.846 ± 0.469 ± 1.547	31.204 ± 0.314 ± 0.737	28.783 ± 0.243 ± 1.046	25.856 ± 0.295 ± 1.028
0.25	36.107 ± 1.233 ± 1.854	33.567 ± 0.399 ± 1.012	27.188 ± 0.288 ± 0.483	24.574 ± 0.235 ± 0.717	-
0.35	32.567 ± 0.744 ± 1.136	23.060 ± 0.311 ± 0.336	19.431 ± 0.235 ± 0.275	17.202 ± 0.241 ± 0.487	-
0.45	22.224 ± 0.519 ± 0.869	15.836 ± 0.251 ± 0.114	12.927 ± 0.191 ± 0.126	10.582 ± 0.249 ± 0.280	-
0.55	13.521 ± 0.346 ± 0.276	10.644 ± 0.203 ± 0.170	8.701 ± 0.159 ± 0.142	-	-
0.65	9.559 ± 0.279 ± 0.225	7.068 ± 0.170 ± 0.036	5.436 ± 0.130 ± 0.103	-	-
0.75	6.013 ± 0.215 ± 0.148	4.098 ± 0.126 ± 0.018	3.796 ± 0.120 ± 0.058	-	-
0.85	3.708 ± 0.161 ± 0.085	2.723 ± 0.105 ± 0.043	2.197 ± 0.097 ± 0.046	-	-
0.95	2.234 ± 0.135 ± 0.066	1.699 ± 0.084 ± 0.049	1.449 ± 0.118 ± 0.047	-	-
1.05	1.542 ± 0.102 ± 0.055	1.079 ± 0.073 ± 0.031	-	-	-

Table C.20: Numerical values of $\frac{d^2n}{dy dp_T}$ spectra of π^- produced in Ar+Sc collisions at 19A GeV/c

p_T [GeV/c]	y: $0.0 < y < 0.2$	$0.2 < y < 0.4$	$0.4 < y < 0.6$	$0.6 < y < 0.8$	$0.8 < y < 1.0$
0.05	-	-	24.538 ± 0.476 ± 10.354	19.191 ± 0.122 ± 0.873	16.499 ± 0.085 ± 0.577
0.15	-	-	39.573 ± 0.353 ± 1.290	38.379 ± 0.234 ± 0.901	33.337 ± 0.173 ± 1.093
0.25	-	41.493 ± 0.596 ± 1.535	36.357 ± 0.276 ± 0.709	33.422 ± 0.212 ± 0.617	29.980 ± 0.183 ± 0.770
0.35	-	29.063 ± 0.298 ± 0.890	26.424 ± 0.222 ± 0.408	23.913 ± 0.176 ± 0.462	21.557 ± 0.239 ± 0.843
0.45	32.397 ± 0.885 ± 1.176	20.728 ± 0.227 ± 0.460	17.369 ± 0.173 ± 0.154	16.050 ± 0.149 ± 0.381	-
0.55	19.980 ± 0.441 ± 0.531	13.466 ± 0.180 ± 0.260	11.484 ± 0.138 ± 0.075	10.835 ± 0.149 ± 0.307	-
0.65	11.700 ± 0.277 ± 0.286	9.224 ± 0.148 ± 0.086	8.018 ± 0.117 ± 0.078	6.717 ± 0.150 ± 0.220	-
0.75	7.517 ± 0.199 ± 0.153	6.094 ± 0.120 ± 0.042	5.280 ± 0.097 ± 0.081	-	-
0.85	4.985 ± 0.153 ± 0.083	3.977 ± 0.097 ± 0.040	3.449 ± 0.079 ± 0.064	-	-
0.95	2.941 ± 0.111 ± 0.070	2.701 ± 0.081 ± 0.027	2.465 ± 0.074 ± 0.064	-	-
1.05	-	1.569 ± 0.060 ± 0.029	1.516 ± 0.078 ± 0.039	-	-

p_T [GeV/c]	y: $1.0 < y < 1.2$
0.05	14.985 ± 0.075 ± 0.593
0.15	31.202 ± 0.189 ± 1.064

Table C.21: Numerical values of $\frac{d^2n}{dy dp_T}$ spectra of π^- produced in Ar+Sc collisions at 30A GeV/c

p_T [GeV/c]	y: $-0.2 < y < 0.0$	$0.0 < y < 0.2$	$0.2 < y < 0.4$	$0.4 < y < 0.6$	$0.6 < y < 0.8$
0.05	-	-	-	-	$22.262 \pm 0.184 \pm 1.002$
0.15	-	-	-	$43.747 \pm 0.525 \pm 1.668$	$43.101 \pm 0.264 \pm 1.149$
0.25	-	-	$43.207 \pm 0.721 \pm 1.721$	$41.015 \pm 0.302 \pm 1.047$	$36.991 \pm 0.224 \pm 0.773$
0.35	-	-	$32.531 \pm 0.325 \pm 0.799$	$28.824 \pm 0.228 \pm 0.472$	$26.436 \pm 0.180 \pm 0.541$
0.45	-	$23.684 \pm 0.463 \pm 1.168$	$23.038 \pm 0.249 \pm 0.426$	$19.515 \pm 0.181 \pm 0.280$	$18.501 \pm 0.163 \pm 0.527$
0.55	-	$16.631 \pm 0.291 \pm 0.467$	$14.510 \pm 0.186 \pm 0.179$	$13.487 \pm 0.152 \pm 0.221$	$12.268 \pm 0.178 \pm 0.437$
0.65	-	$11.566 \pm 0.217 \pm 0.242$	$9.892 \pm 0.154 \pm 0.161$	$8.756 \pm 0.122 \pm 0.188$	-
0.75	-	$7.831 \pm 0.172 \pm 0.144$	$6.367 \pm 0.123 \pm 0.096$	$5.950 \pm 0.107 \pm 0.257$	-
0.85	$6.615 \pm 0.735 \pm 0.310$	$5.061 \pm 0.144 \pm 0.218$	$4.312 \pm 0.103 \pm 0.062$	$4.254 \pm 0.110 \pm 0.157$	-
0.95	$5.246 \pm 0.362 \pm 0.481$	$3.057 \pm 0.100 \pm 0.045$	$3.004 \pm 0.090 \pm 0.055$	$2.686 \pm 0.095 \pm 0.085$	-
1.05	$2.208 \pm 0.649 \pm 0.170$	$2.064 \pm 0.088 \pm 0.050$	$1.984 \pm 0.072 \pm 0.042$	$1.900 \pm 0.104 \pm 0.098$	-
1.15	$1.739 \pm 0.174 \pm 0.215$	$1.423 \pm 0.072 \pm 0.024$	$1.308 \pm 0.063 \pm 0.027$	$0.773 \pm 0.143 \pm 0.074$	-

p_T [GeV/c]	y: $0.8 < y < 1.0$	$1.0 < y < 1.2$	$1.2 < y < 1.4$
0.05	$18.621 \pm 0.101 \pm 0.737$	$17.127 \pm 0.077 \pm 0.562$	$14.626 \pm 0.107 \pm 0.676$
0.15	$37.002 \pm 0.188 \pm 1.170$	$34.784 \pm 0.170 \pm 1.269$	-
0.25	$34.137 \pm 0.189 \pm 1.089$	-	-
0.35	$24.029 \pm 0.240 \pm 0.766$	-	-

Table C.22: Numerical values of $\frac{d^2n}{dy dp_T}$ spectra of π^- produced in Ar+Sc collisions at $40A$ GeV/c

p_T [GeV/c]	y: $-0.2 < y < 0.0$	$0.0 < y < 0.2$	$0.2 < y < 0.4$	$0.4 < y < 0.6$	$0.6 < y < 0.8$
0.05	-	-	-	-	-
0.15	-	-	-	-	$46.253 \pm 0.402 \pm 1.114$
0.25	-	-	-	$47.459 \pm 0.389 \pm 0.924$	$45.490 \pm 0.191 \pm 0.544$
0.35	-	-	$38.911 \pm 0.430 \pm 1.122$	$36.974 \pm 0.197 \pm 0.353$	$31.118 \pm 0.136 \pm 0.298$
0.45	-	-	$26.733 \pm 0.199 \pm 0.279$	$24.311 \pm 0.142 \pm 0.221$	$22.656 \pm 0.113 \pm 0.144$
0.55	-	$19.693 \pm 0.247 \pm 0.322$	$17.999 \pm 0.149 \pm 0.097$	$16.037 \pm 0.110 \pm 0.136$	$16.810 \pm 0.124 \pm 0.084$
0.65	-	$13.688 \pm 0.161 \pm 0.086$	$11.891 \pm 0.114 \pm 0.106$	$11.131 \pm 0.091 \pm 0.080$	-
0.75	$9.225 \pm 0.234 \pm 0.152$	$8.789 \pm 0.122 \pm 0.047$	$7.442 \pm 0.085 \pm 0.050$	$8.038 \pm 0.086 \pm 0.049$	-
0.85	$6.151 \pm 0.172 \pm 0.068$	$5.630 \pm 0.093 \pm 0.036$	$5.248 \pm 0.072 \pm 0.042$	$5.653 \pm 0.098 \pm 0.048$	-
0.95	$4.252 \pm 0.103 \pm 0.057$	$3.799 \pm 0.074 \pm 0.020$	$3.389 \pm 0.057 \pm 0.033$	$3.977 \pm 0.107 \pm 0.032$	-
1.05	$2.795 \pm 0.077 \pm 0.059$	$2.494 \pm 0.059 \pm 0.016$	$2.316 \pm 0.049 \pm 0.018$	-	-
1.15	$2.064 \pm 0.069 \pm 0.013$	$1.491 \pm 0.043 \pm 0.013$	$1.590 \pm 0.054 \pm 0.019$	-	-

p_T [GeV/c]	y: $0.8 < y < 1.0$	$1.0 < y < 1.2$	$1.2 < y < 1.4$	$1.4 < y < 1.6$	$1.6 < y < 1.8$
0.05	-	$21.080 \pm 0.070 \pm 0.429$	$18.111 \pm 0.056 \pm 0.160$	$17.551 \pm 0.059 \pm 0.225$	$16.474 \pm 0.164 \pm 0.306$
0.15	$47.417 \pm 0.171 \pm 0.888$	$39.316 \pm 0.101 \pm 0.310$	$38.303 \pm 0.095 \pm 0.311$	-	-
0.25	$39.067 \pm 0.132 \pm 0.326$	$38.429 \pm 0.126 \pm 0.202$	-	-	-
0.35	$30.597 \pm 0.125 \pm 0.150$	-	-	-	-

Table C.23: Numerical values of $\frac{d^2n}{dy dp_T}$ spectra of π^- produced in Ar+Sc collisions at $75A$ GeV/c

p_T [GeV/c]	y $-0.2 < y < 0.0$	$0.0 < y < 0.2$	$0.2 < y < 0.4$	$0.4 < y < 0.6$	$0.6 < y < 0.8$
0.05	-	-	-	-	-
0.15	-	-	-	-	-
0.25	-	-	-	-	54.772 ± 0.542 ± 2.067
0.35	-	-	-	42.309 ± 0.468 ± 0.962	40.316 ± 0.221 ± 1.097
0.45	-	-	-	28.939 ± 0.216 ± 0.587	26.110 ± 0.157 ± 0.317
0.55	-	-	21.227 ± 0.224 ± 0.416	18.749 ± 0.157 ± 0.336	17.632 ± 0.196 ± 0.203
0.65	-	15.877 ± 0.287 ± 0.362	14.432 ± 0.166 ± 0.244	12.935 ± 0.163 ± 0.202	-
0.75	-	10.123 ± 0.167 ± 0.146	9.358 ± 0.138 ± 0.129	-	-
0.85	6.969 ± 0.229 ± 0.105	6.787 ± 0.130 ± 0.076	5.795 ± 0.183 ± 0.124	-	-
0.95	4.694 ± 0.142 ± 0.093	4.669 ± 0.122 ± 0.066	-	-	-
1.05	3.220 ± 0.114 ± 0.058	3.042 ± 0.168 ± 0.093	-	-	-

p_T [GeV/c]	y $0.8 < y < 1.0$	$1.0 < y < 1.2$	$1.2 < y < 1.4$	$1.4 < y < 1.6$	$1.6 < y < 1.8$
0.05	-	-	22.987 ± 0.146 ± 1.436	20.232 ± 0.097 ± 0.428	19.398 ± 0.085 ± 0.210
0.15	-	48.798 ± 0.181 ± 1.919	44.604 ± 0.131 ± 0.835	41.794 ± 0.135 ± 0.501	38.760 ± 0.220 ± 0.665
0.25	49.600 ± 0.214 ± 1.598	41.666 ± 0.127 ± 0.526	40.035 ± 0.149 ± 0.610	38.364 ± 0.410 ± 0.744	-
0.35	34.480 ± 0.149 ± 0.405	33.786 ± 0.177 ± 0.469	-	-	-
0.45	23.712 ± 0.207 ± 0.272	-	-	-	-

p_T [GeV/c]	y $1.8 < y < 2.0$
0.05	15.773 ± 0.098 ± 0.379

Table C.24: Numerical values of $\frac{d^2n}{dydp_T}$ spectra of π^- produced in Ar+Sc collisions at 150*A* GeV/*c*

C.5 *p* spectra

p_T [GeV/c]	y $-0.8 < y < -0.6$	$-0.6 < y < -0.4$	$-0.4 < y < -0.2$	$-0.2 < y < 0.0$	$0.0 < y < 0.2$
0.05	3.042 ± 0.096 ± 0.102	-	-	-	-
0.15	4.741 ± 0.118 ± 0.154	5.492 ± 0.115 ± 0.133	6.338 ± 0.239 ± 0.176	-	-
0.25	9.457 ± 0.391 ± 0.443	8.343 ± 0.172 ± 0.212	8.539 ± 0.153 ± 0.302	8.558 ± 0.256 ± 0.434	-
0.35	-	13.675 ± 0.450 ± 0.145	10.675 ± 0.199 ± 0.165	10.819 ± 0.177 ± 0.263	11.144 ± 0.381 ± 0.566
0.45	-	-	13.921 ± 0.328 ± 0.282	11.983 ± 0.213 ± 0.735	12.266 ± 0.205 ± 0.111
0.55	-	-	-	12.589 ± 0.240 ± 0.315	12.034 ± 0.205 ± 0.251
0.65	-	-	-	13.862 ± 0.359 ± 0.841	11.340 ± 0.218 ± 0.217
0.75	-	-	-	-	10.342 ± 0.226 ± 0.295
0.85	-	-	-	-	9.149 ± 0.232 ± 0.268
0.95	-	-	-	-	8.214 ± 0.268 ± 0.865
1.05	-	-	-	-	6.933 ± 0.315 ± 0.945

p_T [GeV/c]	y $0.2 < y < 0.4$	$0.4 < y < 0.6$
0.05	-	-
0.15	-	-
0.25	-	-
0.35	-	-
0.45	-	-
0.55	12.439 ± 0.303 ± 0.437	-
0.65	11.479 ± 0.212 ± 0.304	-
0.75	9.967 ± 0.193 ± 0.269	-
0.85	8.583 ± 0.198 ± 0.177	8.233 ± 0.267 ± 0.225
0.95	6.633 ± 0.186 ± 0.109	6.064 ± 0.194 ± 0.058
1.05	5.183 ± 0.169 ± 0.570	4.954 ± 0.167 ± 0.546
1.15	4.336 ± 0.170 ± 0.252	3.945 ± 0.153 ± 0.050

Table C.25: Numerical values of $\frac{d^2n}{dydp_T}$ spectra of *p* produced in Ar+Sc collisions at 13*A* GeV/*c*

p_T [GeV/c]	y: $-1.2 < y < -1.0$	$-1.0 < y < -0.8$	$-0.8 < y < -0.6$	$-0.6 < y < -0.4$	$-0.4 < y < -0.2$
0.05	$0.131 \pm 0.013 \pm 0.033$	$1.259 \pm 0.031 \pm 0.074$	$1.933 \pm 0.051 \pm 0.058$	-	-
0.15	-	$4.505 \pm 0.164 \pm 0.139$	$4.541 \pm 0.104 \pm 0.102$	$4.554 \pm 0.092 \pm 0.136$	-
0.25	-	-	$7.394 \pm 0.207 \pm 0.187$	$6.787 \pm 0.146 \pm 0.180$	$6.962 \pm 0.131 \pm 0.220$
0.35	-	-	-	$9.653 \pm 0.225 \pm 0.177$	$8.678 \pm 0.174 \pm 0.245$
0.45	-	-	-	$12.396 \pm 0.540 \pm 0.240$	$9.962 \pm 0.213 \pm 0.248$
0.55	-	-	-	-	$10.714 \pm 0.285 \pm 0.237$
0.65	-	-	-	-	$12.009 \pm 0.528 \pm 0.222$

p_T [GeV/c]	y: $-0.2 < y < 0.0$	$0.0 < y < 0.2$	$0.2 < y < 0.4$	$0.4 < y < 0.6$
0.05	-	-	-	-
0.15	-	-	-	-
0.25	-	-	-	-
0.35	$8.525 \pm 0.167 \pm 0.216$	-	-	-
0.45	$9.306 \pm 0.178 \pm 0.221$	$9.802 \pm 0.270 \pm 0.210$	-	-
0.55	$9.188 \pm 0.200 \pm 0.271$	$9.901 \pm 0.198 \pm 0.222$	-	-
0.65	$9.211 \pm 0.223 \pm 0.191$	$8.879 \pm 0.189 \pm 0.160$	$10.218 \pm 0.426 \pm 0.289$	-
0.75	$8.967 \pm 0.249 \pm 0.229$	$8.057 \pm 0.200 \pm 0.276$	$8.163 \pm 0.247 \pm 0.214$	-
0.85	$7.807 \pm 0.285 \pm 0.161$	$7.101 \pm 0.211 \pm 0.256$	$7.356 \pm 0.219 \pm 0.167$	-
0.95	$6.415 \pm 0.325 \pm 0.084$	$6.360 \pm 0.225 \pm 0.253$	$5.830 \pm 0.184 \pm 0.138$	-
1.05	$5.423 \pm 0.392 \pm 0.229$	$5.202 \pm 0.220 \pm 0.126$	$4.674 \pm 0.169 \pm 0.118$	-
1.15	$5.116 \pm 0.587 \pm 0.083$	$3.817 \pm 0.184 \pm 0.154$	$3.780 \pm 0.172 \pm 0.125$	-
1.25	-	$3.103 \pm 0.181 \pm 0.114$	$2.665 \pm 0.145 \pm 0.091$	$2.240 \pm 0.209 \pm 0.076$
1.35	-	$2.502 \pm 0.182 \pm 0.103$	$2.276 \pm 0.156 \pm 0.066$	-

Table C.26: Numerical values of $\frac{d^2n}{dy dp_T}$ spectra of p produced in Ar+Sc collisions at 19A GeV/c

p_T [GeV/c]	y: $-1.2 < y < -1.0$	$-1.0 < y < -0.8$	$-0.8 < y < -0.6$	$-0.6 < y < -0.4$	$-0.4 < y < -0.2$
0.05	$1.134 \pm 0.031 \pm 0.261$	$1.366 \pm 0.023 \pm 0.037$	$1.390 \pm 0.022 \pm 0.050$	-	-
0.15	-	$3.821 \pm 0.082 \pm 0.132$	$3.935 \pm 0.062 \pm 0.098$	$3.863 \pm 0.053 \pm 0.117$	-
0.25	-	-	$6.170 \pm 0.109 \pm 0.171$	$5.889 \pm 0.089 \pm 0.177$	$5.800 \pm 0.081 \pm 0.142$
0.35	-	-	$7.642 \pm 0.204 \pm 0.404$	$7.257 \pm 0.119 \pm 0.155$	$7.013 \pm 0.100 \pm 0.183$
0.45	-	-	-	$8.506 \pm 0.157 \pm 0.166$	$7.627 \pm 0.125 \pm 0.234$
0.55	-	-	-	$10.105 \pm 0.274 \pm 0.244$	$8.090 \pm 0.142 \pm 0.157$
0.65	-	-	-	-	$7.711 \pm 0.150 \pm 0.121$
0.75	-	-	-	-	$7.851 \pm 0.191 \pm 0.154$
0.85	-	-	-	-	$6.902 \pm 0.226 \pm 0.198$
0.95	-	-	-	-	$5.627 \pm 0.272 \pm 0.202$
1.05	-	-	-	-	$5.252 \pm 0.346 \pm 0.070$

p_T [GeV/c]	y: $-0.2 < y < 0.0$	$0.0 < y < 0.2$	$0.2 < y < 0.4$
0.05	-	-	-
0.15	-	-	-
0.25	-	-	-
0.35	$7.383 \pm 0.135 \pm 0.181$	-	-
0.45	$7.727 \pm 0.109 \pm 0.208$	-	-
0.55	$7.799 \pm 0.121 \pm 0.153$	$7.813 \pm 0.191 \pm 0.216$	-
0.65	$7.521 \pm 0.135 \pm 0.188$	$7.212 \pm 0.142 \pm 0.171$	-
0.75	$6.447 \pm 0.134 \pm 0.165$	$6.877 \pm 0.130 \pm 0.163$	-
0.85	$5.743 \pm 0.136 \pm 0.165$	$5.688 \pm 0.115 \pm 0.097$	-
0.95	$5.039 \pm 0.137 \pm 0.116$	$4.830 \pm 0.116 \pm 0.069$	-
1.05	$3.660 \pm 0.114 \pm 0.058$	$3.591 \pm 0.103 \pm 0.094$	$4.034 \pm 0.183 \pm 0.140$
1.15	$3.347 \pm 0.132 \pm 0.043$	$3.148 \pm 0.108 \pm 0.076$	$3.235 \pm 0.157 \pm 0.055$
1.25	$2.761 \pm 0.127 \pm 0.056$	$2.241 \pm 0.090 \pm 0.070$	-
1.35	$1.699 \pm 0.126 \pm 0.043$	$1.588 \pm 0.076 \pm 0.048$	-

Table C.27: Numerical values of $\frac{d^2n}{dy dp_T}$ spectra of p produced in Ar+Sc collisions at 30A GeV/c

p_T [GeV/c]	y $-1.2 < y < -1.0$	$-1.0 < y < -0.8$	$-0.8 < y < -0.6$	$-0.6 < y < -0.4$	$-0.4 < y < -0.2$
0.05	1.159 ± 0.040 ± 0.117	1.290 ± 0.021 ± 0.038	1.272 ± 0.018 ± 0.044	1.232 ± 0.025 ± 0.053	-
0.15	-	3.686 ± 0.081 ± 0.164	3.596 ± 0.054 ± 0.067	3.419 ± 0.043 ± 0.082	3.477 ± 0.083 ± 0.117
0.25	-	-	5.388 ± 0.094 ± 0.122	5.247 ± 0.079 ± 0.144	5.341 ± 0.072 ± 0.128
0.35	-	-	7.199 ± 0.183 ± 0.284	6.572 ± 0.111 ± 0.127	6.389 ± 0.093 ± 0.198
0.45	-	-	-	7.340 ± 0.138 ± 0.117	6.693 ± 0.113 ± 0.152
0.55	-	-	-	7.639 ± 0.180 ± 0.213	7.033 ± 0.139 ± 0.152
0.65	-	-	-	7.589 ± 0.259 ± 0.337	7.355 ± 0.161 ± 0.151
0.75	-	-	-	-	6.463 ± 0.164 ± 0.179
0.85	-	-	-	-	5.533 ± 0.162 ± 0.130
0.95	-	-	-	-	5.031 ± 0.188 ± 0.087
1.05	-	-	-	-	3.855 ± 0.180 ± 0.043
1.15	-	-	-	-	2.747 ± 0.166 ± 0.108
1.25	-	-	-	-	2.186 ± 0.160 ± 0.120
1.35	-	-	-	-	1.486 ± 0.214 ± 0.346
1.45	-	-	-	-	1.287 ± 0.174 ± 0.022

p_T [GeV/c]	y $-0.2 < y < 0.0$	$0.0 < y < 0.2$
0.05	-	-
0.15	-	-
0.25	-	-
0.35	6.478 ± 0.127 ± 0.199	-
0.45	6.944 ± 0.107 ± 0.171	-
0.55	6.841 ± 0.112 ± 0.186	-
0.65	6.915 ± 0.136 ± 0.162	6.148 ± 0.162 ± 0.195
0.75	5.913 ± 0.135 ± 0.161	5.925 ± 0.153 ± 0.178
0.85	5.127 ± 0.137 ± 0.111	5.027 ± 0.131 ± 0.101
0.95	4.005 ± 0.125 ± 0.074	4.499 ± 0.129 ± 0.102
1.05	3.681 ± 0.137 ± 0.073	3.524 ± 0.115 ± 0.129
1.15	2.559 ± 0.108 ± 0.078	2.858 ± 0.109 ± 0.088
1.25	2.182 ± 0.110 ± 0.079	2.067 ± 0.090 ± 0.100
1.35	1.581 ± 0.098 ± 0.089	1.564 ± 0.092 ± 0.025
1.45	1.251 ± 0.092 ± 0.019	1.100 ± 0.070 ± 0.031

Table C.28: Numerical values of $\frac{d^2n}{dy dp_T}$ spectra of p produced in Ar+Sc collisions at 40A GeV/c

p_T [GeV/c]	y $-0.8 < y < -0.6$	$-0.6 < y < -0.4$	$-0.4 < y < -0.2$	$-0.2 < y < 0.0$	$0.0 < y < 0.2$
0.05	0.975 ± 0.013 ± 0.023	0.923 ± 0.012 ± 0.010	0.879 ± 0.011 ± 0.018	-	-
0.15	2.746 ± 0.041 ± 0.068	2.639 ± 0.027 ± 0.043	2.417 ± 0.020 ± 0.028	2.408 ± 0.038 ± 0.049	-
0.25	4.077 ± 0.088 ± 0.154	4.227 ± 0.049 ± 0.054	3.669 ± 0.037 ± 0.043	3.858 ± 0.039 ± 0.072	-
0.35	-	5.207 ± 0.067 ± 0.059	4.732 ± 0.054 ± 0.087	4.645 ± 0.043 ± 0.088	-
0.45	-	5.568 ± 0.082 ± 0.067	5.180 ± 0.065 ± 0.085	5.321 ± 0.052 ± 0.100	-
0.55	-	5.689 ± 0.099 ± 0.069	5.376 ± 0.074 ± 0.102	5.287 ± 0.060 ± 0.091	-
0.65	-	5.349 ± 0.111 ± 0.083	5.085 ± 0.079 ± 0.072	5.127 ± 0.066 ± 0.123	5.197 ± 0.088 ± 0.135
0.75	-	4.868 ± 0.121 ± 0.137	4.468 ± 0.077 ± 0.060	4.522 ± 0.067 ± 0.106	4.697 ± 0.081 ± 0.137
0.85	-	4.132 ± 0.120 ± 0.041	4.062 ± 0.079 ± 0.054	4.022 ± 0.067 ± 0.090	4.046 ± 0.079 ± 0.106
0.95	-	3.722 ± 0.126 ± 0.049	3.321 ± 0.074 ± 0.046	3.373 ± 0.065 ± 0.069	3.464 ± 0.074 ± 0.104
1.05	-	2.882 ± 0.117 ± 0.058	2.716 ± 0.069 ± 0.045	2.673 ± 0.060 ± 0.060	2.767 ± 0.071 ± 0.074
1.15	-	-	2.371 ± 0.069 ± 0.037	2.193 ± 0.057 ± 0.044	1.883 ± 0.076 ± 0.054
1.25	-	-	1.865 ± 0.062 ± 0.028	1.695 ± 0.050 ± 0.034	-
1.35	-	-	1.324 ± 0.053 ± 0.020	1.317 ± 0.054 ± 0.037	-

Table C.29: Numerical values of $\frac{d^2n}{dy dp_T}$ spectra of p produced in Ar+Sc collisions at 75A GeV/c

p_T [GeV/c]	y: $-0.6 < y < -0.4$	$-0.4 < y < -0.2$	$-0.2 < y < 0.0$	$0.0 < y < 0.2$
0.05	0.666 ± 0.020 ± 0.057	0.651 ± 0.014 ± 0.039	0.659 ± 0.013 ± 0.049	0.661 ± 0.019 ± 0.058
0.15	1.957 ± 0.044 ± 0.148	1.912 ± 0.024 ± 0.108	1.934 ± 0.024 ± 0.141	1.788 ± 0.031 ± 0.176
0.25	2.955 ± 0.097 ± 0.264	2.921 ± 0.041 ± 0.166	3.020 ± 0.033 ± 0.221	2.910 ± 0.038 ± 0.270
0.35	3.481 ± 0.140 ± 0.312	3.814 ± 0.063 ± 0.200	3.645 ± 0.048 ± 0.271	3.608 ± 0.051 ± 0.319
0.45	4.309 ± 0.189 ± 0.457	4.456 ± 0.081 ± 0.224	4.105 ± 0.063 ± 0.304	3.948 ± 0.083 ± 0.328
0.55	3.957 ± 0.188 ± 0.409	4.452 ± 0.089 ± 0.226	4.537 ± 0.078 ± 0.346	-
0.65	4.071 ± 0.195 ± 0.360	4.590 ± 0.101 ± 0.251	4.332 ± 0.089 ± 0.305	-
0.75	3.955 ± 0.189 ± 0.215	3.975 ± 0.098 ± 0.239	3.852 ± 0.107 ± 0.263	-
0.85	3.405 ± 0.184 ± 0.202	3.603 ± 0.100 ± 0.197	3.617 ± 0.147 ± 0.228	-
0.95	3.002 ± 0.164 ± 0.189	2.921 ± 0.094 ± 0.175	-	-
1.05	-	2.214 ± 0.090 ± 0.126	-	-
1.15	-	2.102 ± 0.127 ± 0.104	-	-

Table C.30: Numerical values of $\frac{d^2n}{dydp_T}$ spectra of p produced in Ar+Sc collisions at 150A GeV/c

C.6 $\bar{p}$ spectra

p_T [GeV/c]	y: $-1.2 < y < -1.0$	$-1.0 < y < -0.8$	$-0.8 < y < -0.6$	$-0.6 < y < -0.4$	$-0.4 < y < -0.2$
0.05	0.013 ± 0.005 ± 0.009	0.008 ± 0.002 ± 0.002	0.008 ± 0.001 ± 0.001	-	-
0.15	-	0.030 ± 0.007 ± 0.001	0.026 ± 0.004 ± 0.001	0.028 ± 0.004 ± 0.002	-
0.25	-	-	0.042 ± 0.008 ± 0.004	0.038 ± 0.005 ± 0.003	0.059 ± 0.007 ± 0.002
0.35	-	-	0.057 ± 0.013 ± 0.004	0.050 ± 0.008 ± 0.002	0.062 ± 0.007 ± 0.003
0.45	-	-	-	0.059 ± 0.010 ± 0.001	0.071 ± 0.009 ± 0.002
0.55	-	-	-	0.068 ± 0.016 ± 0.008	0.079 ± 0.012 ± 0.002
0.65	-	-	-	-	0.069 ± 0.011 ± 0.003
0.75	-	-	-	-	0.040 ± 0.009 ± 0.003
0.85	-	-	-	-	0.049 ± 0.015 ± 0.004
0.95	-	-	-	-	0.042 ± 0.014 ± 0.003

p_T [GeV/c]	y: $-0.2 < y < 0.0$	$0.0 < y < 0.2$
0.05	-	-
0.15	-	-
0.25	-	-
0.35	0.069 ± 0.009 ± 0.003	-
0.45	0.087 ± 0.009 ± 0.002	-
0.55	0.084 ± 0.010 ± 0.002	0.049 ± 0.009 ± 0.004
0.65	0.071 ± 0.010 ± 0.008	0.082 ± 0.011 ± 0.004
0.75	0.088 ± 0.013 ± 0.004	0.063 ± 0.009 ± 0.003
0.85	0.056 ± 0.011 ± 0.004	0.059 ± 0.010 ± 0.003
0.95	0.039 ± 0.009 ± 0.002	0.053 ± 0.011 ± 0.003
1.05	0.050 ± 0.014 ± 0.003	0.021 ± 0.005 ± 0.003

Table C.31: Numerical values of $\frac{d^2n}{dydp_T}$ spectra of $\bar{p}$ produced in Ar+Sc collisions at 30A GeV/c

p_T [GeV/c]	y: $-1.2 < y < -1.0$	$-1.0 < y < -0.8$	$-0.8 < y < -0.6$	$-0.6 < y < -0.4$	$-0.4 < y < -0.2$
0.05	$0.005 \pm 0.003 \pm 0.004$	$0.011 \pm 0.002 \pm 0.001$	$0.011 \pm 0.001 \pm 0.001$	$0.017 \pm 0.002 \pm 0.002$	-
0.15	-	$0.021 \pm 0.005 \pm 0.000$	$0.038 \pm 0.004 \pm 0.004$	$0.050 \pm 0.004 \pm 0.003$	$0.046 \pm 0.006 \pm 0.006$
0.25	-	-	$0.051 \pm 0.007 \pm 0.001$	$0.076 \pm 0.007 \pm 0.006$	$0.091 \pm 0.007 \pm 0.003$
0.35	-	-	$0.099 \pm 0.018 \pm 0.007$	$0.091 \pm 0.010 \pm 0.007$	$0.103 \pm 0.008 \pm 0.003$
0.45	-	-	-	$0.098 \pm 0.012 \pm 0.005$	$0.101 \pm 0.010 \pm 0.006$
0.55	-	-	-	$0.124 \pm 0.018 \pm 0.005$	$0.133 \pm 0.015 \pm 0.007$
0.65	-	-	-	$0.137 \pm 0.029 \pm 0.008$	$0.138 \pm 0.019 \pm 0.013$
0.75	-	-	-	-	$0.103 \pm 0.015 \pm 0.018$
0.85	-	-	-	-	$0.088 \pm 0.017 \pm 0.007$
0.95	-	-	-	-	$0.059 \pm 0.014 \pm 0.004$
1.05	-	-	-	-	$0.074 \pm 0.035 \pm 0.008$
1.15	-	-	-	-	$0.064 \pm 0.029 \pm 0.043$

p_T [GeV/c]	y: $-0.2 < y < 0.0$	$0.0 < y < 0.2$
0.05	-	-
0.15	-	-
0.25	-	-
0.35	$0.096 \pm 0.009 \pm 0.007$	-
0.45	$0.122 \pm 0.010 \pm 0.007$	-
0.55	$0.105 \pm 0.010 \pm 0.005$	-
0.65	$0.127 \pm 0.013 \pm 0.004$	$0.102 \pm 0.014 \pm 0.006$
0.75	$0.097 \pm 0.012 \pm 0.007$	$0.078 \pm 0.010 \pm 0.010$
0.85	$0.103 \pm 0.016 \pm 0.006$	$0.087 \pm 0.013 \pm 0.003$
0.95	$0.066 \pm 0.012 \pm 0.015$	$0.060 \pm 0.010 \pm 0.002$
1.05	$0.051 \pm 0.010 \pm 0.009$	$0.069 \pm 0.014 \pm 0.019$
1.15	$0.036 \pm 0.009 \pm 0.002$	$0.038 \pm 0.010 \pm 0.010$

Table C.32: Numerical values of $\frac{d^2n}{dy dp_T}$ spectra of $\bar{p}$ produced in Ar+Sc collisions at 40*A* GeV/*c*

p_T [GeV/c]	y: $-0.8 < y < -0.6$	$-0.6 < y < -0.4$	$-0.4 < y < -0.2$	$-0.2 < y < 0.0$	$0.0 < y < 0.2$
0.05	$0.045 \pm 0.003 \pm 0.002$	$0.044 \pm 0.002 \pm 0.001$	$0.045 \pm 0.002 \pm 0.001$	-	-
0.15	$0.132 \pm 0.009 \pm 0.003$	$0.131 \pm 0.005 \pm 0.005$	$0.118 \pm 0.004 \pm 0.002$	$0.132 \pm 0.007 \pm 0.003$	-
0.25	$0.188 \pm 0.019 \pm 0.010$	$0.203 \pm 0.010 \pm 0.005$	$0.163 \pm 0.007 \pm 0.003$	$0.223 \pm 0.008 \pm 0.004$	-
0.35	-	$0.224 \pm 0.013 \pm 0.002$	$0.208 \pm 0.009 \pm 0.005$	$0.238 \pm 0.008 \pm 0.006$	-
0.45	-	$0.258 \pm 0.017 \pm 0.006$	$0.221 \pm 0.011 \pm 0.007$	$0.256 \pm 0.010 \pm 0.006$	-
0.55	-	$0.231 \pm 0.019 \pm 0.007$	$0.212 \pm 0.012 \pm 0.008$	$0.247 \pm 0.011 \pm 0.005$	-
0.65	-	$0.198 \pm 0.019 \pm 0.011$	$0.247 \pm 0.015 \pm 0.006$	$0.251 \pm 0.012 \pm 0.014$	$0.274 \pm 0.015 \pm 0.009$
0.75	-	$0.218 \pm 0.023 \pm 0.006$	$0.204 \pm 0.015 \pm 0.005$	$0.225 \pm 0.012 \pm 0.006$	$0.216 \pm 0.013 \pm 0.008$
0.85	-	$0.261 \pm 0.039 \pm 0.008$	$0.179 \pm 0.015 \pm 0.006$	$0.201 \pm 0.013 \pm 0.005$	$0.206 \pm 0.015 \pm 0.010$
0.95	-	$0.152 \pm 0.022 \pm 0.010$	$0.155 \pm 0.014 \pm 0.004$	$0.140 \pm 0.010 \pm 0.004$	$0.192 \pm 0.015 \pm 0.009$
1.05	-	$0.173 \pm 0.030 \pm 0.013$	$0.128 \pm 0.014 \pm 0.003$	$0.109 \pm 0.009 \pm 0.004$	$0.129 \pm 0.012 \pm 0.006$
1.15	-	-	$0.080 \pm 0.010 \pm 0.002$	$0.093 \pm 0.009 \pm 0.004$	$0.083 \pm 0.013 \pm 0.005$

Table C.33: Numerical values of $\frac{d^2n}{dy dp_T}$ spectra of $\bar{p}$ produced in Ar+Sc collisions at 75*A* GeV/*c*

p_T [GeV/c]	y: $-0.6 < y < -0.4$	$-0.4 < y < -0.2$	$-0.2 < y < 0.0$	$0.0 < y < 0.2$
0.05	0.067 ± 0.005 ± 0.006	0.087 ± 0.004 ± 0.005	0.087 ± 0.004 ± 0.005	0.069 ± 0.004 ± 0.007
0.15	0.252 ± 0.015 ± 0.017	0.219 ± 0.007 ± 0.009	0.227 ± 0.006 ± 0.017	0.209 ± 0.008 ± 0.018
0.25	0.387 ± 0.035 ± 0.025	0.365 ± 0.013 ± 0.018	0.324 ± 0.008 ± 0.024	0.328 ± 0.010 ± 0.030
0.35	0.358 ± 0.043 ± 0.009	0.526 ± 0.021 ± 0.028	0.411 ± 0.012 ± 0.030	0.519 ± 0.016 ± 0.042
0.45	0.513 ± 0.071 ± 0.028	0.502 ± 0.022 ± 0.021	0.467 ± 0.016 ± 0.034	0.396 ± 0.020 ± 0.037
0.55	0.599 ± 0.078 ± 0.016	0.623 ± 0.031 ± 0.026	0.534 ± 0.020 ± 0.042	-
0.65	0.552 ± 0.074 ± 0.023	0.505 ± 0.028 ± 0.022	0.450 ± 0.021 ± 0.030	-
0.75	0.431 ± 0.064 ± 0.018	0.426 ± 0.027 ± 0.023	0.433 ± 0.029 ± 0.029	-
0.85	0.400 ± 0.055 ± 0.027	0.324 ± 0.022 ± 0.018	0.409 ± 0.041 ± 0.028	-
0.95	0.282 ± 0.047 ± 0.021	0.256 ± 0.021 ± 0.016	-	-
1.05	-	0.248 ± 0.025 ± 0.016	-	-

Table C.34: Numerical values of $\frac{d^2n}{dy dp_T}$ spectra of $\bar{p}$ produced in Ar+Sc collisions at 150*A* GeV/*c*

List of Abbreviations

ADC	Analog to Digital Converter
AGS	Alternating Gradient Synchrotron
ALICE	A Large Ion Collider Experiment
ATLAS	A Toroidal LHC ApparatuS
BNL	Brookhaven National Laboratory
BPD	Beam Position Detect
CEDAR	Cherenkov Differential Counter with Achromatic Ring Focus
CERN	European Organization for Nuclear Research
CFD	Constant-Fraction Discriminator
CMS	Compact Muon Solenoid
CP	Critical Point
DAQ	Data AcQuisition
$\mathbf{d}E/\mathbf{d}x$	analysis method based on energy loss measurement
DRS	Domino Ring Sampling
DUNE	Deep Underground Neutrino Experiment
ECR	Electron Cyclotron Resonance
FEE	Front-End Electronics
FPGA	Field Programmable Gate Array
FTPC	Forward Time Projection chamber
GAP-TPC	Gap Time Projection Chamber
GEANT	GEometry ANd Tracking
HG	Hadron Gas
LEIR	Low Energy Ion Ring
LHC	Large Hadron Cillider
LHT	Liquid Hydrogen Target
LINAC	Linear accelerator
LS2	CERN Long Shutdown 2
MAPD	Micro-pixel Avalanche PhotoDiode
MC	Monte Carlo
MHTDC	Multi-Hit Time Digital Converter
MT	Main Trigger
MTPC	Main Time Projection Chamber
MWPC	Multi-Wire Proportional Chamber
NuMI	Neutrinos at the Main Injector
NA49	49^{th} experiment in the CERN North Area

NA61/SHINE	61^{st} experiment in the CERN North Area SPS Heavy Ion and Neutrino Experiment
NOνA	(NuMI Off-Axis ν_e Appearance
PHSD	Parton-Hadron-String Dynamics
PMT	Photo-Multiplier Tube
PS	Proton Synchrotron
PSB	Proton Synchrotron Booster
PSD	Projectile Spectator Detector
QCD	Quantum ChromoDynamics
QDC	Charge to Digital Converter
QED	Quantum ElectroDynamics
QGP	Quark-Gluon Plasma
RHIC	Relativistic Heavy Ion Collider
RFQ	Radio-Frequency Quadrupole
RST	Right-Side Track
SAVD	Small Acceptance Vertex Detector
SM	Standard Model
SMASH	Simulating Many Accelerated Strongly-interacting Hadrons
SMES	Statistical Model of the Early Stage
SPS	Super Proton Synchrotron
T2K	Tokai to Kamioka experiment
TDC	Time to Digital Converter
ToF	Time-of-Flight detector
ToF-F	Forward Time-of-Flight Detector
ToF-L	Left Time-of-Flight Detector
ToF-R	Right Time-of-Flight Detector
$\boldsymbol{tof} - \mathbf{d}E/\mathbf{d}x$	Analysis method based on the simultaneous measurement of the energy loss and the time-of-flight
TPC	Time Projection Chamber
VD	Vertex Detector
VTPC	Vertex Time Projection Chamber
WDXRF	Wavelength Dispersive X-Ray Fluorescence
WLS	Wave-Length-Shifter
WNM	Wounded Nucleon Model
WST	Wrong-Side Track

References

[1] S. Weinberg, "The Making of the standard model," *Eur. Phys. J. C* **34** (2004) 5–13.

[2] G. Aad *et al.*, [ATLAS Collab.], "Observation of a new particle in the search for the Standard Model Higgs boson with the ATLAS detector at the LHC," *Phys. Lett. B* **716** (2012) 1–29.

[3] S. Chatrchyan *et al.*, [CMS Collab.], "Observation of a New Boson at a Mass of 125 GeV with the CMS Experiment at the LHC," *Phys. Lett. B* **716** (2012) 30–61.

[4] "Wikipedia, the free encyclopedia." `https://en.wikipedia.org/`. Accessed: 2021-02-15.

[5] R. Aaij *et al.*, [LHCb Collab.], "Observation of the resonant character of the $Z(4430)^-$ state," *Phys. Rev. Lett.* **112** no. 22, (2014) 222002.

[6] R. Aaij *et al.*, [LHCb Collab.], "Observation of $J/\psi p$ Resonances Consistent with Pentaquark States in $\Lambda_b^0 \to J/\psi K^- p$ Decays," *Phys. Rev. Lett.* **115** (2015) 072001.

[7] R. Aaij *et al.*, [LHCb Collab.], "Observation of a narrow pentaquark state, $P_c(4312)^+$, and of two-peak structure of the $P_c(4450)^+$," *Phys. Rev. Lett.* **122** no. 22, (2019) 222001.

[8] S. L. Glashow, "The renormalizability of vector meson interactions," *Nucl. Phys.* **10** (1959) 107–117.

[9] A. Salam and J. C. Ward, "Electromagnetic and weak interactions," *Phys. Lett.* **13** (1964) 168–171.

[10] J. Leite Lopes and N. Fleury, "A Model for Leptons," *Lett. Nuovo Cim.* **19** (1977) 7.

[11] F. Englert and R. Brout, "Broken Symmetry and the Mass of Gauge Vector Mesons," *Phys. Rev. Lett.* **13** (1964) 321–323.

[12] P. W. Higgs, "Broken Symmetries and the Masses of Gauge Bosons," *Phys. Rev. Lett.* **13** (1964) 508–509.

[13] P. Zyla *et al.*, [Particle Data Group Collab.], "Review of Particle Physics," *PTEP* **2020** no. 8, (2020) 083C01.

[14] G. S. Bali, "QCD forces and heavy quark bound states," *Phys. Rept.* **343** (2001) 1–136.

[15] K. G. Wilson, "Confinement of quarks," *Phys. Rev. D* **10** (Oct, 1974) 2445–2459.

[16] G. 't Hooft, "On the Phase Transition Towards Permanent Quark Confinement," *Nucl. Phys. B* **138** (1978) 1–25.

[17] D. J. Gross and F. Wilczek, "Ultraviolet Behavior of Nonabelian Gauge Theories," *Phys. Rev. Lett.* **30** (1973) 1343–1346.

[18] H. D. Politzer, "Reliable Perturbative Results for Strong Interactions?," *Phys. Rev. Lett.* **30** (1973) 1346–1349.

[19] J. C. Collins and M. J. Perry, "Superdense Matter: Neutrons Or Asymptotically Free Quarks?," *Phys. Rev. Lett.* **34** (1975) 1353.

[20] E. V. Shuryak, "Quark-Gluon Plasma and Hadronic Production of Leptons, Photons and Psions," *Sov. J. Nucl. Phys.* **28** (1978) 408.

[21] E. V. Shuryak, "Quantum Chromodynamics and the Theory of Superdense Matter," *Phys. Rept.* **61** (1980) 71–158.

[22] H. H. Dalsgaard, *Pseudorapidity Densities in p+p and Pb+Pb collisions at LHC measured with the ALICE experiment*. PhD thesis, Bohr Inst., 2012. `http://cds.cern.ch/record/1453242`.

[23] M. I. Gorenstein, "Discovery of quark-gluon plasma in nucleus nucleus collisions at CERN SPS," in *Crimean Summer School-Seminar on New Trends in High-Energy Physics (Crimean 2000)*, pp. 128–134. 5, 2000.

[24] T. Ludlam, "Experimental results from the early measurements at RHIC: Hunting for the quark-gluon plasma," *Nucl. Phys. A* **750** (2005) 9–29.

[25] A. Bazavov *et al.*, [HotQCD Collab.], "Chiral crossover in QCD at zero and non-zero chemical potentials," *Phys. Lett. B* **795** (2019) 15–21.

[26] M. A. Stephanov, "QCD phase diagram: An Overview," *PoS* **LAT2006** (2006) 024.

[27] Z. Fodor and S. D. Katz, "Critical point of QCD at finite T and mu, lattice results for physical quark masses," *JHEP* **04** (2004) 050.

[28] M. Lewicki. Private communication.

[29] A. Bialas, M. Bleszynski, and W. Czyz, "Multiplicity Distributions in Nucleus-Nucleus Collisions at High-Energies," *Nucl. Phys. B* **111** (1976) 461–476.

[30] K. Grebieszkow, "Lecture on introduction to heavy ion collisions." 2019/2020. `http://www.if.pw.edu.pl/~kperl/HIP/hip.html`.

[31] M. Gazdzicki and M. I. Gorenstein, "On the early stage of nucleus-nucleus collisions," *Acta Phys. Polon. B* **30** (1999) 2705, `arXiv:hep-ph/9803462`.

[32] C. Alt *et al.*, [NA49 Collab.], "Pion and kaon production in central Pb + Pb collisions at 20-A and 30-A-GeV: Evidence for the onset of deconfinement," *Phys. Rev. C* **77** (2008) 024903.

[33] J. Cleymans, R. V. Gavai, and E. Suhonen, "Quarks and Gluons at High Temperatures and Densities," *Phys. Rept.* **130** (1986) 217.

[34] A. Acharya *et al.*, [NA61/SHINE Collab.], "Measurements of $\pi^{\pm}$, $K^{\pm}$, p and $\bar{p}$ spectra in ^{7}Be+^{9}Be collisions at beam momenta from 19A to 150A GeV/c with the NA61/SHINE spectrometer at the CERN

SPS," *Eur. Phys. J. C* **81** no. 1, (2021) 73.

[35] A. Acharya *et al.*, [NA61/SHINE Collab.], "Measurements of π^- production in ^{7}Be+^{9}Be collisions at beam momenta from 19*A* to 150*A*GeV/*c* in the NA61/SHINE experiment at the CERN SPS," *Eur. Phys. J. C* **80** no. 10, (2020) 961.

[36] A. Aduszkiewicz *et al.*, [NA61/SHINE Collab.], "Measurements of $\pi^\pm$, $K^\pm$, p and $\bar{p}$ spectra in proton-proton interactions at 20, 31, 40, 80 and 158 GeV/*c* with the NA61/SHINE spectrometer at the CERN SPS," *Eur.Phys.J.* **C77** no. 10, (2017) 671.

[37] R. V. Poberezhnyuk, M. Gazdzicki, and M. I. Gorenstein, "Statistical Model of the Early Stage of nucleus-nucleus collisions with exact strangeness conservation," *Acta Phys. Polon. B* **46** no. 10, (2015) 1991.

[38] K. Abe *et al.*, [T2K Collab.], "The T2K Experiment," *Nucl. Instrum. Meth. A* **659** (2011) 106–135.

[39] D. S. Ayres *et al.*, [NOvA Collab.], "NOvA: Proposal to Build a 30 Kiloton Off-Axis Detector to Study $\nu_\mu \rightarrow \nu_e$ Oscillations in the NuMI Beamline,".

[40] J. Abraham *et al.*, [Pierre Auger Collab.], "Properties and performance of the prototype instrument for the Pierre Auger Observatory," *Nucl. Instrum. Meth. A* **523** (2004) 50–95.

[41] G. Schatz, [KASCADE Collab.], "The KASCADE cosmic ray experiment," *Nucl. Phys. B Proc. Suppl.* **43** (1995) 261–264.

[42] . Aduszkiewicz *et al.*, [NA61/SHINE Collaboration Collab.], "Feasibility Study for the Measurement of Nuclear Fragmentation Cross Sections with NA61/SHINE at the CERN SPS," Tech. Rep. CERN-SPSC-2017-035. SPSC-P-330-ADD-9, CERN, Geneva, Oct, 2017. `https://cds.cern.ch/record/2287004`.

[43] F. Becattini, J. Manninen, and M. Gazdzicki, "Energy and system size dependence of chemical freeze-out in relativistic nuclear collisions," *Phys. Rev. C* **73** (2006) 044905.

[44] [NA61/SHINE Collab.], "Image library.".

[45] A. Aduszkiewicz *et al.*, [NA61/SHINE Collab.], "Proton-Proton Interactions and Onset of Deconfinement," *Phys. Rev. C* **102** no. 1, (2020) 011901.

[46] J. Adam *et al.*, [ALICE Collab.], "Enhanced production of multi-strange hadrons in high-multiplicity proton-proton collisions," *Nature Phys.* **13** (2017) 535–539.

[47] V. Khachatryan *et al.*, [CMS Collab.], "Evidence for collectivity in pp collisions at the LHC," *Phys. Lett. B* **765** (2017) 193–220.

[48] N. Abgrall *et al.*, [NA61/SHINE Collab.], "NA61/SHINE facility at the CERN SPS: beams and detector system," *JINST* **9** (2014) P06005.

[49] S. Afanasiev *et al.*, [NA49 Collab.], "The NA49 large acceptance hadron detector," *Nucl. Instrum. Meth. A* **430** (1999) 210–244.

[50] N. Abgrall *et al.*, [NA61/SHINE Collab.], "Measurement of negatively charged pion spectra in inelastic p+p interactions at p_{lab} = 20, 31, 40, 80 and 158 GeV/c," *Eur.Phys.J.* **C74** (2014) 2794.

[51] N. Abgrall *et al.*, [NA61/SHINE Collab.], "Measurements of $\pi^{\pm}$ differential yields from the surface of the T2K replica target for incoming 31 GeV/c protons with the NA61/SHINE spectrometer at the CERN SPS," *Eur. Phys. J.* **C76** no. 11, (2016) 617.

[52] N. Abgrall *et al.*, [NA61/SHINE Collab.], "Measurements of $\pi^{\pm}$, $K^{\pm}$ and proton double differential yields from the surface of the T2K replica target for incoming 31 GeV/c protons with the NA61/SHINE spectrometer at the CERN SPS," *Eur. Phys. J.* **C79** no. 2, (2019) 100.

[53] C. Bov, R. Maleyran, A. Placci, and M. Placidi, "The CEDAR (Cerenkov Differential Counters with Achromatic Ring Focus) Project," *IEEE Transactions on Nuclear Science* **25** no. 1, (Feb, 1978) 572–576.

[54] B. Rumberger *et al.*, "The Forward TPC system of the NA61/SHINE experiment at CERN: a tandem TPC concept," *JINST* **15** no. 07, (2020) P07013.

[55] R. Renfordt, [NA61/SHINE Collab.], "Introduction to NA61/SHINE Time Projection Chambers." `https://indico.cern.ch/event/515331/`.

[56] F. Sauli, "Principles of operation of multiwire proportional and drift chambers," *CERN-77-09* (1977) .

[57] G. Charpak and F. Sauli, "Multiwire proportional chambers and drift chambers," *Nucl. Instrum. Meth. A* **162** no. 1, (1979) 405 – 428.

[58] M. Ćwiok *et al.*, "A TPC Detector for Studying Photo-nuclear Reactions at Astrophysical Energies with Gamma-ray Beams at ELI–NP," *Acta Phys. Polon. B* **49** (2018) 509–514.

[59] [The ALICE Collaboration Collab.], "Upgrade of the ALICE Time Projection Chamber," Tech. Rep. CERN-LHCC-2013-020. ALICE-TDR-016, Oct, 2013. `https://cds.cern.ch/record/1622286`.

[60] G. Dellacasa *et al.*, [ALICE Collab.], "ALICE: Technical design report of the time projection chamber,".

[61] F. Bieser *et al.*, "Design and performance of TPC readout electronics for the NA49 experiment," *Nucl. Instrum. Meth. A* **385** no. 3, (1997) 535 – 546.

[62] S. Ritt, R. Dinapoli, and U. Hartmann, "Application of the DRS chip for fast waveform digitizing," *Nucl. Instrum. Meth. A* **623** no. 1, (2010) 486 – 488.

[63] A. Aduszkiewicz, [NA61/SHINE Collab.], "Beam momentum scan with Pb+Pb collisions," tech. rep., CERN, Geneva, Oct, 2015. `https://cds.cern.ch/record/2059811`.

[64] A. Dorokhov *et al.*, "High resistivity CMOS pixel sensors and their application to the STAR PXL detector," *Nucl. Instrum. Meth. A* **650**

no. 1, (2011) 174 – 177.

[65] M. Deveaux *et al.*, "Radiation tolerance of a column parallel CMOS sensor with high resistivity epitaxial layer," *JINST* **6** no. 02, (Feb, 2011) C02004–C02004.

[66] A. Aduszkiewicz, *Energy dependence of negatively charged pion production in proton-proton interactions at the CERN SPS*. PhD thesis, University of Warsaw, 2015. https://cds.cern.ch/record/2135329.

[67] K. Werner, "The hadronic interaction model EPOS," *Nuclear Physics B - Proceedings Supplements* **175-176** (2008) 81 – 87. Proceedings of the XIV International Symposium on Very High Energy Cosmic Ray Interactions.

[68] R. Brun, R. Hagelberg, M. Hansroul, and J. C. Lassalle, "Geant: Simulation Program for Particle Physics Experiments. User Guide and Reference Manual,". https://cds.cern.ch/record/118715.

[69] D. Banas, A. Kubala-Kukus, M. Rybczynski, I. Stabrawa, and G. Stefanek, "Influence of target material impurities on physical results in relativistic heavy-ion collisions," *Eur. Phys. J. Plus* **134** no. 1, (2019) 44.

[70] A. Acharya *et al.*, [NA61/SHINE Collab.], "Spectra and mean multiplicities of π^- in central^{40}Ar+^{45}Sc collisions at 13A, 19A, 30A, 40A, 75A and 150A Ge V/c beam momenta measured by the NA61/SHINE spectrometer at the CERN SPS," *Eur. Phys. J. C* **81** no. 5, (2021) 397.

[71] E. Kaptur, *Analysis of collision centrality and negative pion spectra in ^{7}Be + ^{9}Be interactions at CERN SPS energy range*. PhD thesis, University of Silesia, 2017. https://edms.cern.ch/document/2004086/1.

[72] M. Naskręt. Private communication.

[73] A. Seryakov, [NA61/SHINE Collab.], "PSD acceptance maps for event selection." https://edms.cern.ch/document/1867336/1.

[74] A. Rustamov and M. I. Gorenstein, "Identity Method for Moments of Multiplicity Distribution," *Phys. Rev. C* **86** (2012) 044906.

[75] M. Lewicki, *Charged hadron production in central Ar+Sc collisions at the CERN SPS*. PhD thesis, University of Wrocław, 2021.

[76] M. Gazdzicki, M. Gorenstein, and P. Seyboth, "Onset of deconfinement in nucleus-nucleus collisions: Review for pedestrians and experts," *Acta Phys. Polon. B* **42** (2011) 307–351.

[77] B. I. Abelev *et al.*, [STAR Collab.], "Systematic Measurements of Identified Particle Spectra in pp, d^+ Au and Au+Au Collisions from STAR," *Phys. Rev. C* **79** (2009) 034909.

[78] M. Kliemant, B. Lungwitz, and M. Gazdzicki, "Energy dependence of transverse mass spectra of kaons produced in p + p and p + anti-p interactions: A Compilation," *Phys. Rev. C* **69** (2004) 044903.

[79] K. Aamodt *et al.*, [ALICE Collab.], "Production of pions, kaons and

protons in *pp* collisions at $\sqrt{s} = 900$ GeV with ALICE at the LHC," *Eur. Phys. J. C* **71** (2011) 1655, 1101.4110.

[80] B. B. Abelev *et al.*, [ALICE Collab.], "Production of charged pions, kaons and protons at large transverse momenta in pp and Pb–Pb collisions at $\sqrt{s_{NN}}$ =2.76 TeV," *Phys. Lett. B* **736** (2014) 196–207, 1401.1250.

[81] L. Adamczyk *et al.*, [STAR Collab.], "Bulk Properties of the Medium Produced in Relativistic Heavy-Ion Collisions from the Beam Energy Scan Program," *Phys. Rev. C* **96** no. 4, (2017) 044904.

[82] J. Adams *et al.*, [STAR Collab.], "Identified particle distributions in pp and Au+Au collisions at $\sqrt{s_{NN}} = 200$ GeV," *Phys. Rev. Lett.* **92** (2004) 112301.

[83] K. Adcox *et al.*, [PHENIX Collab.], "Single identified hadron spectra from $\sqrt{s_{NN}} = 130$ GeV Au+Au collisions," *Phys. Rev. C* **69** (2004) 024904.

[84] S. S. Adler *et al.*, [PHENIX Collab.], "Identified charged particle spectra and yields in Au+Au collisions at $\sqrt{s_{NN}} = 200$ GeV," *Phys. Rev. C* **69** (2004) 034909.

[85] I. Arsene *et al.*, [BRAHMS Collab.], "Centrality dependent particle production at y=0 and y ~ 1 in Au + Au collisions at $\sqrt{s_{NN}} = 200$ GeV," *Phys. Rev. C* **72** (2005) 014908.

[86] L. Ahle *et al.*, [E-802, E-866 Collab.], "Centrality dependence of kaon yields in Si + A and Au + Au collisions at the AGS," *Phys. Rev. C* **60** (1999) 044904.

[87] T. Anticic *et al.*, [NA49 Collab.], "System-size and centrality dependence of charged kaon and pion production in nucleus-nucleus collisions at 40A GeV and158A GeV beam energy," *Phys. Rev. C* **86** (2012) 054903.

[88] S. V. Afanasiev *et al.*, [NA49 Collab.], "Energy dependence of pion and kaon production in central Pb + Pb collisions," *Phys. Rev. C* **66** (2002) 054902.

[89] B. Abelev *et al.*, [ALICE Collab.], "Pion, Kaon, and Proton Production in Central Pb–Pb Collisions at $\sqrt{s_{NN}} = 2.76$ TeV," *Phys. Rev. Lett.* **109** (2012) 252301, 1208.1974.

[90] K. Werner, L. Karpenko, M. Bleicher, and T. Pierog, "The Physics of EPOS," *EPJ Web Conf.* **52** (2013) 05001.

[91] W. Cassing and E. L. Bratkovskaya, "Parton transport and hadronization from the dynamical quasiparticle point of view," *Phys. Rev. C* **78** (2008) 034919.

[92] W. Cassing and E. L. Bratkovskaya, "Parton-Hadron-String Dynamics: an off-shell transport approach for relativistic energies," *Nucl. Phys. A* **831** (2009) 215–242.

[93] V. Kireyeu. Private communication.

[94] J. Mohs, S. Ryu, and H. Elfner, "Particle Production via Strings and Baryon Stopping within a Hadronic Transport Approach," *J. Phys. G*

47 no. 6, (2020) 065101.

[95] J. Weil *et al.*, "Particle production and equilibrium properties within a new hadron transport approach for heavy-ion collisions," *Phys. Rev. C* **94** no. 5, (2016) 054905.

[96] M. Gazdzicki and A. Rybicki, [NA61/SHINE Collab.], "Overview of Results from NA61/SHINE: Uncovering Critical Structures," *Acta Phys. Polon. B* **50** (2019) 1057–1070.

[97] P. Podlaski and L. Fields, [NA61/SHINE Collab.], "Report from the NA61/SHINE experiment at the CERN SPS," Tech. Rep. CERN-SPSC-2020-023. SPSC-SR-278, CERN, Geneva, Oct, 2020. `https://cds.cern.ch/record/2739340`.

[98] A. Aduszkiewicz *et al.*, [NA61/SHINE Collab.], "Study of Hadron-Nucleus and Nucleus-Nucleus Collisions at the CERN SPS: Early Post-LS2 Measurements and Future Plans," Tech. Rep. CERN-SPSC-2018-008. SPSC-P-330-ADD-10, CERN, Geneva, Mar, 2018. `https://cds.cern.ch/record/2309890`.

[99] A. Aduszkiewicz *et al.*, [NA61/SHINE Collab.], "Reply to the SPSC questions on Addendum CERN-SPSC-2018-008 entitled Study of Hadron-Nucleus and Nucleus-Nucleus Collisions at the CERN SPS: Early Post-LS2 Measurements and Future Plans ," Tech. Rep. CERN-SPSC-2018-019. SPSC-P-330-ADD-11, CERN, Geneva, Jun, 2018. `https://cds.cern.ch/record/2621751`.

[100] 2020. Technical Design Reports for the upgrade of the NA61/SHINE detector subsystems, `https://edms.cern.ch/document/2422986/1`.